DNA ADSORPTION ONTO GLASS SURFACES

BY

KRISTA LYNN CARLSON

A THESIS

SUBMITTED TO THE FACULTY OF

ALFRED UNIVERSITY

IN PARTIAL FULFILLMENT OF THE REQUIREMENTS
FOR THE DEGREE OF

DOCTOR OF PHILOSOPHY

IN

GLASS SCIENCE

ALFRED, NEW YORK

MAY, 2008

DNA ADSORPTION ONTO GLASS SURFACES

BY

KRISTA LYNN CARLSON

B.S. ALFRED UNIVERSITY (2004)

SIGNATURE OF AUTHOR (Signature on File)

APPROVED BY (Signature on File)
MATTHEW M. HALL, ADVISOR

(Signature on File)
WILLIAM M. CARTY, ADVISORY COMMITTEE

(Signature on File)
LISA M. FLICK, ADVISORY COMMITTEE

(Signature on File)
WILLIAM C. LACOURSE, ADVISORY COMMITTEE

(Signature on File)
CHAIR, ORAL THESIS DEFENSE

ACCEPTED BY (Signature on File)
ALASTAIR N. CORMACK, DEAN
KAZUO INAMORI SCHOOL OF ENGINEERING

ACCEPTED BY (Signature on File)
WILLIAM M. HALL, ASSOCIATE PROVOST
FOR GRADUATE AND PROFESSIONAL PROGRAMS
ALFRED UNIVERSITY

ACKNOWLEDGMENTS

Thanks, Rosalind Franklin, for showing me why it is important to analyze your XRD patterns asap.

Thanks, Mom, for naming me Krista Lynn…if not I might have only worked with amorphous materials forever! Thanks also for keeping me too well fed…I will now be back on the free donut and pasta diet.

Thanks, Uncle Bob, for giving me a huge quartz crystal. I would have never known how beautiful ceramics actually were.

Thanks, Ms. Ann Baldwin, I'll never be too busy to fight for NYSCC…someday we'll get that Science on Wheels money back from AU and start it up again at the new HSCC @ Kauai.

Thanks, Dr. Clare, for making glass become more than just windows and letting me crush glass for Matt.

Thanks, Matt, for allowing me to destroy expensive glassware and ask stupid questions… however, I am still waiting for my freshman glass crusher.

Thanks, Dr. Carty, Dr. Flick and Dr. LaCourse, for your input and reading this overgrown picture book.

Thanks, Gerry and Mercedes, for helping me obtain 98.3% of photos and references in here.

Thanks, Dad. Thanks for attempting to teach me calculus and the meaning of π when I was 3. Thanks for making me think that plotting solitaire stats was actually a fun game. Most importantly, thanks for being like Feynman's father and constantly telling me random facts about the world. Just think, I could have turned out like Feynman if after age 3 I had developed an attention span longer than 30 seconds!

TABLE OF CONTENTS

LIST OF TABLES

LIST OF FIGURES

ABSTRACT

Streaming potential measurements were performed on microspheres of silica, soda lime silicate (SLS) and calcium aluminate (CA) glasses containing silica and iron oxide (CASi and CAFe). The silicate based glasses exhibited acidic surfaces with isoelectric points (IEP) around a pH of 3 while the calcium aluminates displayed more basic surfaces with IEP ranging from 8-9.5. The surface of the calcium aluminate microspheres containing silica reacted with the background electrolyte, altering the measured zeta potential values and inhibiting electrolyte flow past the sample at ~ pH 4 due to formation of a solid plug.

DNA adsorption experiments were performed using the microspheres and a commercially available silicate based DNA isolation filter using a known quantity of DNA suspended in a chaotropic agent free 0.35 wt% Tris(hydroxymethyl)aminomethane (Tris) buffer solution. The microspheres and commercial filter were also used to isolate DNA from macrophage cells in the presence of chaotropic agents. UV absorbance at ~260 nm and gel electrophoresis were used to quantify the amount and size of the DNA strands that adsorbed to the microsphere surfaces. In both experiments, the 43-106 μm CAFe microspheres adsorbed the largest quantity of DNA. However, the 43-106 μm SLS microspheres isolated more DNA from the cells than the <43 μm CAFe microspheres, indicating that microsphere size contributes to isolation ability.

The UV absorbance of DNA at ~260 nm was slightly altered due to the dissolution of the calcium aluminate glasses during the adsorption process. Inductively coupled plasma - optical emission spectroscopy (ICP-OES) determined that calcium and aluminum ions leached from the CA and CAFe microsphere surfaces during these experiments. Circular dichroism (CD) spectroscopy showed that the leached ions had no effect on the conformation of the DNA, and therefore would not be expected to interfere in downstream applications such as DNA replication.

The 0.35 wt% Tris solution completely inhibited the formation of the hydrated crystalline layer that develops when the calcium aluminate glassess are incubated in deionized water. A Tris concentration of 0.24 wt% allowed for the formation of both hexagonal and cubic hydrates, however they were severely distorted and present in low amounts such that they were undectable by XRD.

CHAPTER 1: DETERMINATION OF ZETA POTENTIAL USING STREAMING POTENTIAL MEASUREMENTS

I LITERATURE REVIEW

A. Surface Behavior of Oxide Materials in Aqueous Solutions

1. Origin of Surface Charge and the Electrical Double Layer

The charge that develops at an oxide surface when its placed in contact with an aqueous solution, is dependent on the electronegativity of the cations in the material and the solution pH.[1-4] The surface charge of a material is pH dependent and occurs through either physical or chemical reactions with molecular or dissociated water molecules. Changes in surface charge through physical adsorption occur through non-dissociative reactions such as hydrogen bonding while chemical reactions can be regarded as acid-base reactions with the amphoteric -MOH groups

$$-MOH_2^+ \xleftarrow{+H^+} -MOH \xrightarrow{-H+} -MO^- + H^+$$

or as the adsorption of H^+ or OH^-

$$-MOH_2^+ \xleftarrow{+H^+} -MOH \xrightarrow{+OH^-} -M(OH)_2^- \leftrightarrow -MO^- + H_2O$$

Surface charge can also develop through the specific adsorption of electrolyte ions oppositely charged to that of the surface.[3,5,6] When the concentration of cations and anions in solution is unequal, the species present in greater quantity tends to have a greater affinity for the oxide surface. This effect is more noticeable with di- and tri-valent cations than with mono-valent cations, which tend to be introduced into solution in a 1:1 ratio with the anions. A more detailed description of electrolyte adsorption is discussed in Ch 1. I. A. 2.

To preserve electroneutrality, a charge compensating electrical double layer (EDL) forms at the sample surface and is composed of aligned water molecules and/or

ions from the electrolyte solution.[1-3,7] The EDL consists of two regions; an inner layer of tightly bound ions called the compact or Stern layer and a more dispersed outer region called the diffuse layer. Two slightly different models exist to describe the structure and resulting electric potentials of these two layers.

In the Stern-Graheme model shown in Figure 1, the potential at the surface is compensated by specifically adsorbed ions of opposite charge (counter-ions) that can only approach the surface to within their ionic radius.[1-3,7] Since ions can exhibit various hydration states, the Stern layer is further divided into an inner plane, located at the center of specifically adsorbed dehydrated ions, and an outer plane, located at the center of the hydrated ions. These planes are referred to as the Inner and Outer Helmholtz planes and exhibit a linear decrease in potential away from the surface due to an absence of free charge. Specific adsorption is considered to be the result of temporary electrostatic or van der Waals forces that are strong enough to overcome thermal agitation. Ions in this layer are not considered to be rigidly bound to one location but are thought of as mobile, with the ability to immediately react to the oxide surface charge with changes in pH and ionic strength.

Ions located outside of the Outer Helmholtz plane are considered to be part of the diffuse layer.[1-3,7] While this layer is mainly composed of counter-ions, some co-ions are also present. The exponential decay of potential from the surface results from a combination of Coulombic attractions to the surface and a tendency to move into the bulk from thermal motion. The approximation used to calculate the thickness of this layer is discussed in Ch 1. I. A. 2.

The Bockris-Devanathan-Muller model, Figure 2, is a modification of the Stern-Graheme model where the hydrated counter-ions are separated from the oxide surface by a monolayer of oriented water molecules.[1-3,7,8] The plane between the hydrated cations and the diffuse layer is now termed the Gouy plane. This model is usually employed when an oxide surface has difficulty obtaining or maintaining an equilibrium potential with the aqueous solution. This model is commonly used in easily hydrated materials, such as cement, where exposure to aqueous solutions causes the release of dissolution products into solution and the precipitation of hydrated phases onto the surface. The

hydrated nature of the Stern layer in this model is a more accurate description of a continuously changing surface.

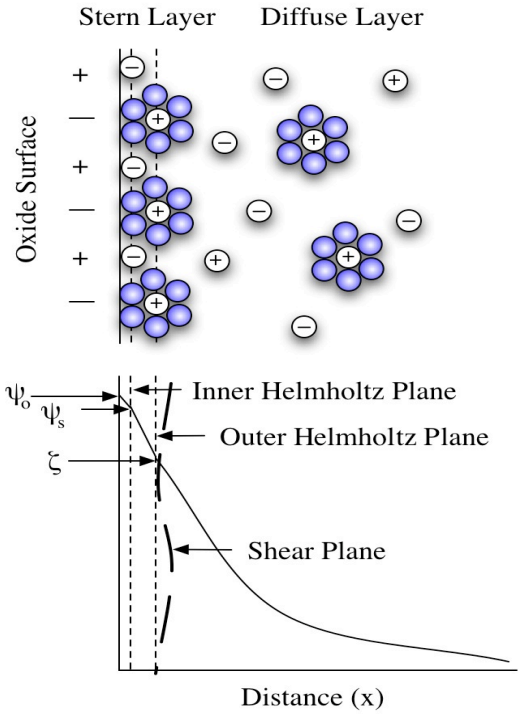

Figure 1. Schematic of the Stern-Graheme model of the EDL.

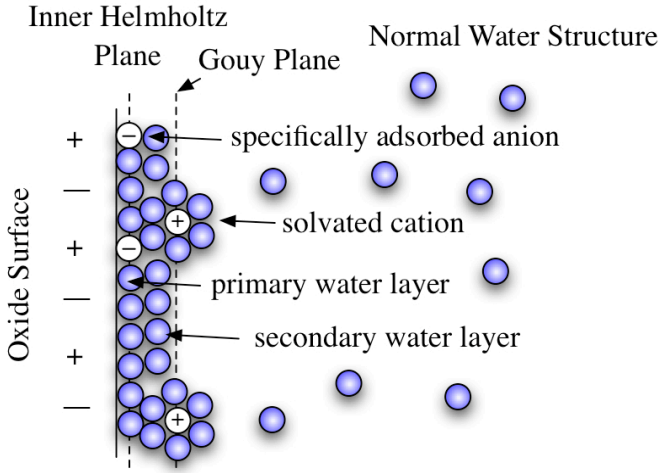

Figure 2. Schematic of the Bockris-Devanathan-Muller model of the EDL.

In either model, the diffuse layer may be sheared from the Stern layer through the application of an electric field or by the physical movement of solution past the solid surface. [1-3,7] The potential at this shear plane is called the zeta potential, ζ, Figure 1, and is usually considered to be located at the Gouy plane. However, the location of this plane, discussed in Ch 1. I. A. 2., can vary depending on the surface reactions taking place and the instrument used for the measurement. The zeta potential represents the surface charge of a material in an aqueous solution at various pH values and electrolyte concentrations. The pH at which the zeta potential value is zero is called the isoelectric point (IEP) and is independent of ionic strength if the background electrolyte is indifferent to the oxide surface. The pH at which the IEP occurs, and the magnitude of surface charge above and below this point, are directly related to the cations in the oxide material.[4,9] The IEP of an oxide will usually decrease as the ratio between the cation radius and its formal charge decreases. Table I shows this trend with MO_2 having the highest IEP and MO_3 having the lowest. The broad range of IEP within each group is due to factors such as differences in hydration state and cation radius. Oxides do not always follow these trends however, since the local environment and partial charge on the oxygen atom must also be taken into account. The oxide surface is known to become more basic as the oxygen coordination number decreases and its partial charge increases.

Table I. Cation Oxidation States and their Predicted IEP.

Cation Oxidation State	pH of IEP
M_2O	>11.5
MO	8.5-12.5
M_2O_3	6.5-10.4
MO_2	0.5-7.5
M_2O_5	<.5
MO_3	<.5

2. Determining Surface Charge through Electrokinetic Characterization

Electrokinetic phenomena occur when the diffuse layer of the EDL is sheared from the compact layer due to either the physical flow of solution past the solid sample surface or an applied electric field. [1-3,7] The application of either method will result in the

occurrence of the other (i.e. the application of an electric field will also cause fluid flow). Several types of phenomena arise depending on the chosen application and the mobility of the material being examined. Streaming potential is the most useful technique for zeta potential determination of bulk materials and non-colloidal particles. Streaming potential measurements generate zeta potential values through the physical flow of electrolyte solution across a sample located between two electrodes. Fluid pressure across the sample shears the diffuse layer, causing a streaming current and the accumulation of ions at one of the electrodes. The potential difference created from ion accumulation generates a backflow current which opposes the streaming current. The potential difference across the cell, called the streaming potential, is measured once steady state between the two currents has been established. The measured zeta potential is usually of higher magnitude than those produced by other methods due to the location of the shear plane closer to the surface and lower dissolution rates associated with bulk materials.[1,3,10] While the actual location of the zeta potential thought to be slightly farther out than the Gouy plane, it is commonly assigned to this location since the measured potential is only marginally lower than expected.

The equation used to calculate the zeta potential can be derived using expressions for streaming and backflow currents through a capillary, where the EDL is considered to be confined to a thin region near the wall.[1] The streaming current, I_S, can be expressed as:

$$I_S = -\frac{\varepsilon\zeta}{l\eta}\pi r^2 p \tag{1}$$

where ζ is the zeta potential, ε and η are the dielectric permittivity and viscosity of the electrolyte solution, l is the length of the capillary, r is the radius of the capillary, and p is the pressure gradient down the capillary.

The backflow current, I_B, resulting from the development of the potential difference between the electrodes is given by:

$$I_B = \frac{\pi r^2 U_S \sigma_0}{l} + \frac{2\pi r U_S \sigma_S}{l} \tag{2}$$

where U_S is the streaming potential, σ_s is the specific surface conductivity, and σ_0 is the conductance of a cylindrical shaped area of solution. When equilibrium has been established between the two currents:

$$I_S + I_B = 0 \tag{3}$$

Combining Equations 1 and 2:

$$\frac{U}{P} = \frac{\varepsilon \zeta}{\eta(\sigma_0 + 2\sigma_S / r)} \tag{4}$$

Equation 4 is only valid under certain conditions:[1,3]

1) The electrolyte flow over the sample is laminar
2) The thickness of the EDL is significantly smaller than the diameter of the pores through which the electrolyte is flowing through
3) The material surface is both physically and chemically homogeneous
4) The EDL and adjacent solution can be modeled as having the geometry of a parallel plate or capillary capacitor
5) The flow channel does not have a concentration gradient along its axis

When most of the charge is transported by the bulk electrolyte solution and not at the sample surface, such as in a perfect insulator, σ_s may be removed from the equation. The Electro Kinetic Analyzer from Anton Paar calculates the zeta potential using:[11]

$$\zeta = \frac{dU}{dp} \frac{\eta}{\varepsilon} \sigma \tag{5}$$

where the ratio dU/dp was substituted for U/p to eliminate any differences in polarization between the two electrodes.

3. Effect of Electrolyte Solution on Zeta Potential

The potential throughout the diffuse layer can be modeled using a combination of the Poisson and Bolatzmann equations and the Debye-Huckel approximation:[1,3]

$$\psi = \psi_0 \exp(-\kappa x) \tag{6}$$

where ψ and ψ_0 are the electric potentials in the diffuse layer and at surface, x is the distance away from the surface and κ is defined as:

$$\kappa = \sqrt{\frac{8\pi n e^2 v^2}{\varepsilon k T}} \tag{7}$$

where *e* and *v* are the electronic and valence charge, *k* is Botltzman's constant, and *T* is temperature. The thickness of the diffuse layer is defined as the case in which x equals 1/κ, because after this point the potential becomes so low that any change is considered negligible.

Increasing the ionic strength of the background electrolyte will cause the diffuse layer to become compressed, pushing ions into the Stern layer. [1,3] An increased concentration of ions in the Stern layer provides greater surface charge shielding, therefore reducing the potential in the diffuse layer. Figure 3 shows that while an increase in ionic strength will decrease the overall magnitude of the zeta potential, the IEP should remain the same. In most cases it is assumed that the background electrolyte is indifferent to the oxide surface, compensating the surface charge via weak physical interactions. However, oppositely charged electrolyte ions can develop a difference in affinity for an oxide surface after the addition of a titrant that is composed of one of the electrolyte ions. Physical adsorption of the electrolyte ion with a larger concentration can occur, but is only observed where the ion and the oxide surface exhibit opposite charges due to the weak electrostatic nature of these interactions. The minima/maxima exhibited at the ends of the zeta potential curves in Figure 4 are the result of physical adsorption. Chemical adsorption is also possible under electrolyte concentrations that are not 1:1 and at extremes in pH. These bonds are much stronger and the electrolyte can remain attached to the oxide surface even after they exhibit the same charge. While the chemical adsorption of counter-ions will cause a shift in the IEP, as shown in Figure 4, the

chemical adsorption of co-ions will have little, if any, effect on the overall surface charge.

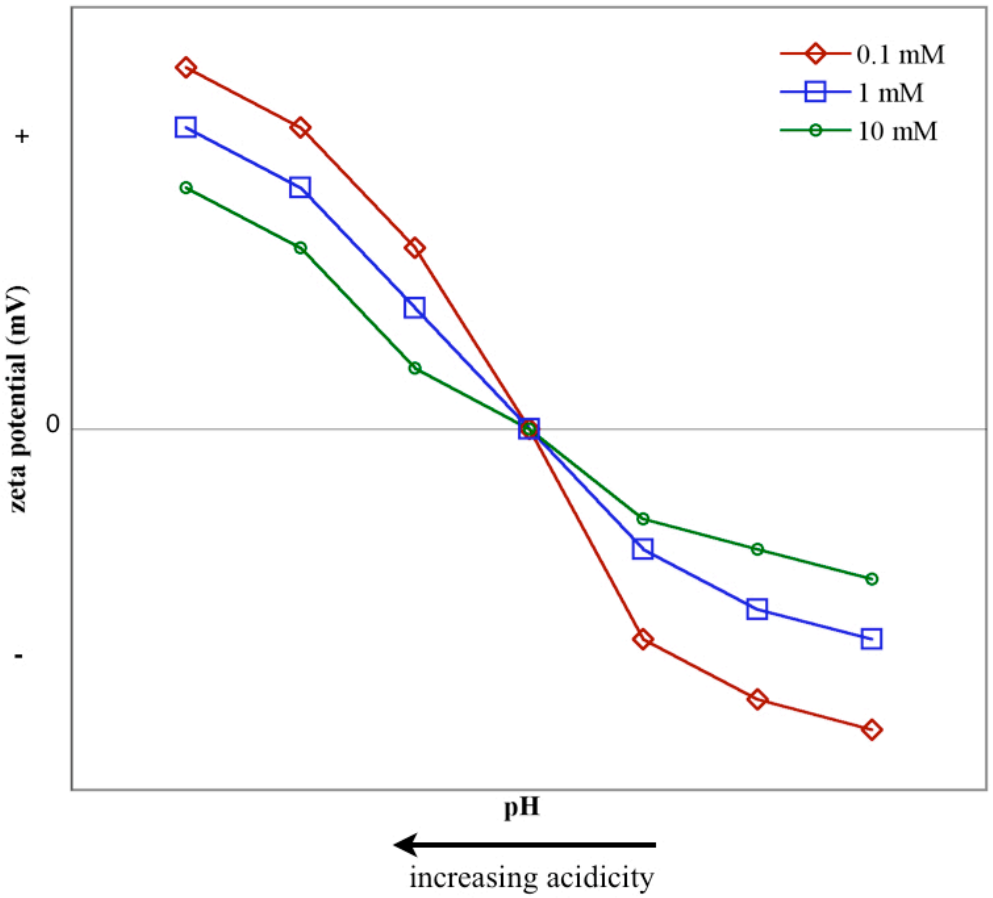

Figure 3. Effect of ionic strength on zeta potential.

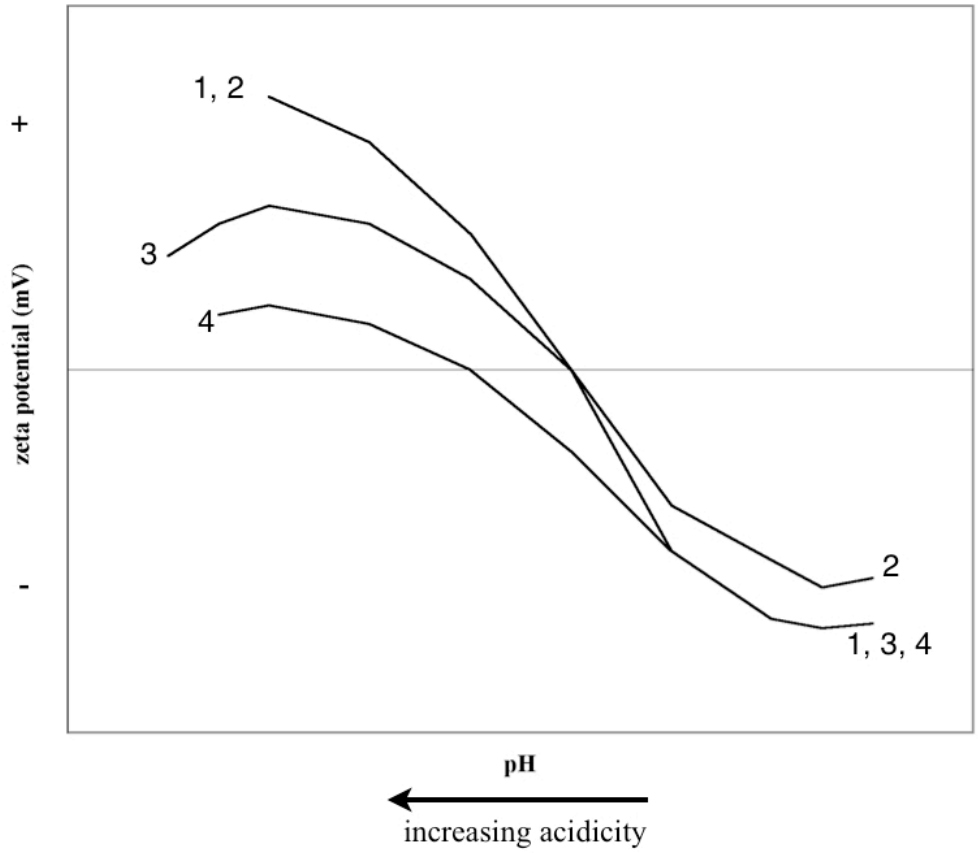

Figure 4. Effect of physical and chemical adsorption on zeta potential; 1) no specific adsorption, 2) physical adsorption of cations, 3) physical adsorption of anions, 4) chemical adsorption of anions.

II INTRODUCTION – PART I. SILICATE AND CALCIUM ALUMINATE BASED GLASSES

Understanding the development of surface charge exhibited by an oxide material in aqueous solutions is important in applications ranging from the stability of charged colloidal systems to the electrostatic interactions between oxides and biological materials.[1,2,7,12,13] Surface modifications to an oxide through the chemical adsorption of inorganic or organic materials are often performed to produce a net charge opposite to that of the original material.[12,14,15] A more efficient method to produce a desired surface charge is to inherently alter the charge through modifications to the original oxide composition.

The purpose of this study was to examine the effect of compositional changes on the surface charge exhibited by amorphous, multi-component silicate and calcium aluminate based glasses. Zeta potential values were obtained through streaming potential measurements. Previous studies have reported low pH IEP for silicate based glasses and high pH IEP for crystalline alumina and calcium carbonate, reflecting the acidic and basic nature of the surfaces, respectively.[4,11,16-22]

III EXPERIMENTAL PROCEDURE

A. Sample Preparation

Calcium aluminate based glasses were prepared using reagent grade Na_2CO_3, K_2CO_3, CaO, Fe_2O_3, Al_2O_3, and SiO_2. Batch constituents were mixed with a mortar and pestle and placed in a 99.8% alumina crucible for melting. Batches with a mass of 30 g were melted at 1600°C with melting times ranging from 30 to 90 minutes depending on the glass composition. Melts were quenched by pouring into a stainless steel container filled with water. The addition of silica to the calcium aluminate batches improved the formability so that water quenching was not necessary, however it was still performed to maintain consistent sample preparation. The glasses were crushed using a stainless steel press and particles in the size range between 106-150 μm were retained through sieving. Frit was also formed from silica tubing and uncoated soda lime silicate (SLS) microscope slides. Glass compositions were examined using inductively coupled plasma – optical emission spectroscopy (ICP-OES) since melting in alumina crucibles can slightly alter the batched composition. Table II shows the compositions for the glasses used in this study with all error less than 0.1 mol%. No ICP-OES was performed on the commercial silicate glasses.

Table II. Glass Compositions.

Name	Composition (mol%)						Melt Time (hours)
	Na_2O	K_2O	CaO	Al_2O_3	Fe_2O_3	SiO_2	
CA	0.3	-	59.0	40.7	-	-	0.5
CASi	0.2	-	52.5	39.2	-	8.1	0.5
CAFe	5.2	1.4	28.0	55.0	10.4	-	1.5
2CAFe	9.7	2.2	30.9	55.4	1.8	-	1.0
SLS	15.0	-	10.0	1.0	-	74.0	N/A
SiO2	-	-	-	-	-	100.0	N/A

The glass frit was formed into microspheres to produce samples with uniform morphology that would exhibit consistent packing behavior. The microspheres were

formed by dropping frit into an oxygen-propane flame at 1900˚C via a vibrating spatula. The frit size range between 106-150 μm was used because particles in this size range flowed smoothly into the flame with little agglomeration. The flame was kept under oxidizing conditions to prevent the formation of a carbon coating. The irregularly shaped particles melted and became spherical as they traveled through the flame, eventually landing in a collection chamber. The unannealed microspheres were stored in sealed plastic containers in ambient atmosphere. A schematic of this process is shown in Figure 5.

Microspheres were visually examined using an environmental scanning electron microscope (Environmental Scanning Electron Microscope (ESEM), FEI, Hillsboro, OR). ESEM samples were prepared by covering a sample stub with carbon tape and sprinkling the microspheres onto it with a small metal spatula. The samples were then coated with about 150-200 Å of carbon. The microspheres were examined in low vacuum mode with pressures ranging from 1-1.1 Pa, an accelerating potential of 20 kV, and beam spot size of 4. When energy dispersive spectroscopy (EDS) was performed, the accelerating potential and beam spot size were changed to 25 kV and 5, respectively.

An electron microprobe (JXA-8200 Electron Microprobe (EMP), JEOL, Peabody, MA) was used to examine microsphere compositional homogeneity. Microspheres were mounted in a phenolic thermosetting powder and polished to a 1 μm finish using diamond suspensions. The polished samples were coated with ~15 nm of carbon. A stage scan with a fixed focus beam was performed using an accelerating potential of ~15 kV and a beam current of ~1 nA. Any alterations to the surface during polishing were negligible since the x-ray radiation collected is from a depth of at least 1 μm into the sample surface.

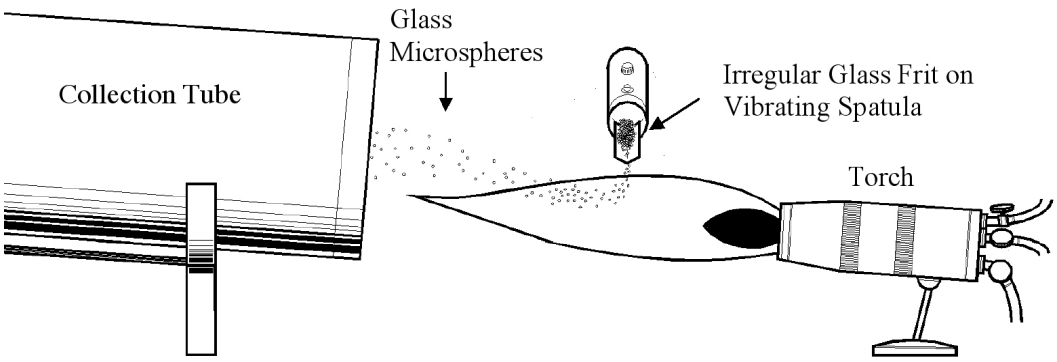

Figure 5. Schematic of microsphere formation.

B. Streaming Potential Measurements

An electro kinetic analyzer (Electrokinetic Analyzer (EKA), Anton Paar, Graz, Austria) used streaming potential measurements along with automated titrations to determine the zeta potential values on the glass microspheres over a continuous pH range. A schematic of the instrument is shown in Figure 6. Measurements were performed using the cylindrical measuring cell and the powder cell insert, which were specifically designed for the examination of coarse (>50 μm) particles. The microspheres were placed in the powder cell in between two filter membranes containing a 43 μm pore size. A cell used to control the solution temperature and atmosphere was added later by the author since the probes used to measure pH and conductivity are sensitive to these parameters. After each measurement the instrument was rinsed with a non-ionic surfactant solution to remove any possible electrolyte contamination and then rinsed with a reagent alcohol solution to remove any surfactant contamination from the prior rinse. The zeta potential was calculated using Equation 5.

The EKA measurement parameters were chosen based on manufacturer recommendation and are given in Table III. Electrode asymmetry was accounted for by passing the electrolyte solution over the porous plug in alternating directions and by using the change in potential vs. pressure in Equation 5. Longer measurement and rinse times (up to 60 seconds) and an increased number of alternating repetitions through the cell (up to 2) produced reproducible zeta potential values for the silicate glasses and the

CAFe glass but not for the CASi and the 2CAFe glasses. Each glass was measured 3 times with reproducibility to within $\pm$ 2 mV for all glasses except for the 2CAFe and CASi which were measured 4 and 6 times and led to reproducibility to within $\pm$ 5 mV and $\pm$ 10 mV, respectively. A 10 mM KCl solution was used as the background electrolyte to negate any effects from conductivity occurring at the sample surface. Titrations were kept between pH values of 2.5 and 10.5 to prevent electrode damage. The initial zeta potential values were measured before any titrations were performed.

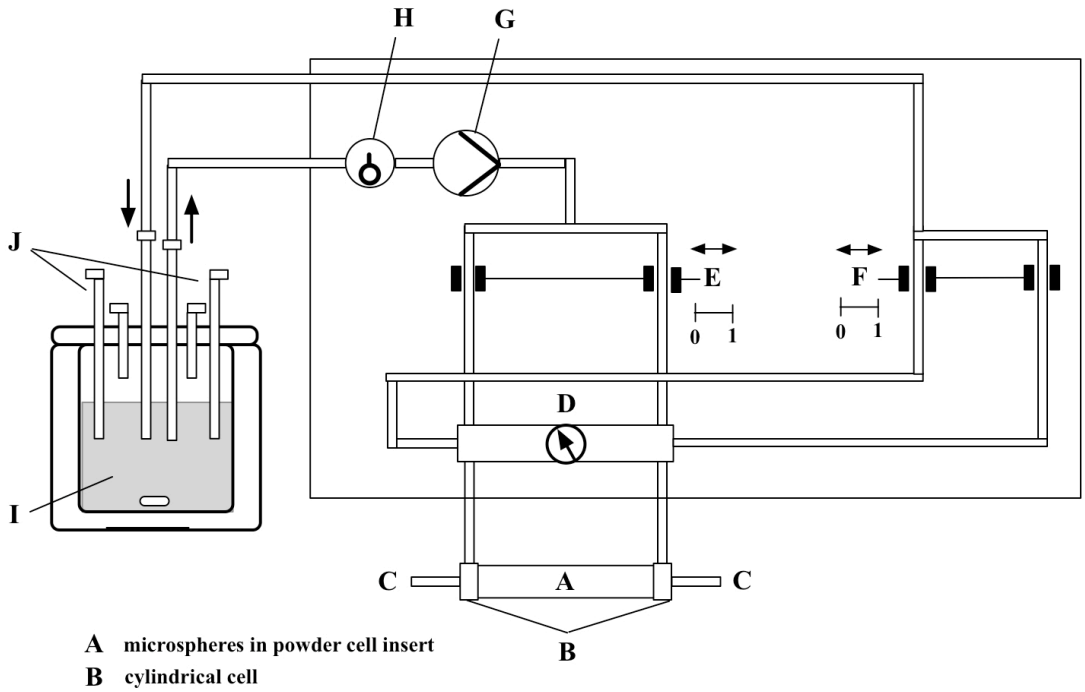

A microspheres in powder cell insert
B cylindrical cell
C measuring electrodes
D differential pressure sensor
E right pinch solenoid valve
F left pinch solenoid valve
G pump
H temperature sensor
I temperature and atmosphere controlled cell containing the electrolyte solution and stirbar
J pH and conductivity probes, nitrogen gas inlet/outlet

Figure 6. Schematic of the EKA.

Table III. EKA Parameters.

Sample Size	0.4 - 0.6 g
Temperature	25˚C
Atmosphere	Nitrogen
Electrolyte Solution	10 mM KCl
Titration	started from pH of 10 mM KCl
Titrant for Decreasing pH	0.1 N HCl
Titrant for Increasing pH	0.1 N KOH
Cell Pressure Program	
Maximum Pressure	400 mbar
Measurement Time	30 sec
Number of Repititions	1
Cell Rinse Program	
Maximum Pressure	300 mbar
Time in Bypass	5 sec
Time in Cell	5 sec
Number of Repititions	1
Automated Titration Program	
pH Differenece Between Measurements	0.2
Initial Amount of Titrant	0.2 ml

Inductively coupled plasma optical emission spectroscopy (Inductively coupled plasma optical emission spectroscopy (ICP-OES), Perkin Elmer, Waltham, MA) was performed on KCl solutions extracted during the streaming potential measurements. Solution was extracted at the same time a zeta potential value was measured to determine the concentration and type of ions present at each point during the measurement. Solution collection was performed during different streaming potential measurements than the ones used to determine the zeta potential values, since the atmosphere and temperature controlled cell had to be opened during solution extraction.

IV RESULTS

A. Sample Preparation

Microsphere examination with the ESEM showed that dropping the frit through the flame almost always produced solid, spherical particles for the CA and CASi microspheres, as shown in Figures 7a and b. The SLS and CAFe frit produced microspheres similar to the CA but sometimes formed microspheres with surface pitting or crystallization, as shown in Figures 7c and d, respectively. The amount of crystallization on the CAFe was low enough not to be detected using x-ray diffraction. The size of the microspheres remained within the original frit size range of 106-150 μm with an average sphere size of 123 μm $\pm$ 11.

EMP confirmed that the composition was homogeneous throughout the microspheres. Figure 8 shows the compositional variation for each element throughout a single microsphere of CAFe. The CAFe microsphere shown is from the 43-106 μm size group, prepared for experiments in Chapter 2, but is representative of the microspheres from all sizes ranges. The gray scale intensity varies for each element and therefore the actual intensity values were used to make compositional comparisons between each element. Compositional fluctuations around the edges were more difficult to determine since some structural damage occurred during the mounting and polishing process. A slight intensity loss around the edge of the microspheres was noticed and is thought to be the result of the space between the microsphere and the mount matrix.

B. Streaming Potential Measurements

Figure 9 shows the most representative streaming potential curve measured for each glass. The unfilled symbols represent the start of the measurements titrated with either HCl (solid line connector) or KOH (dashed line connector). The asterisk on the abscissa represents the initial pH of the electrolyte solution which was 5.5 $\pm$ 0.3. All streaming potential measurements curves are represented in this manner.

Silicate based glasses have significantly lower IEP values than the calcium aluminate based glasses. The zeta potential values for the CASi glass titrated with HCl

showed an unusual plateau soon after its IEP, with values at low pH being unattainable. Table IV shows that the IEP values obtained in this study are similar to values reported in other studies that also used streaming potential measurements.[4,11,16-23]

The shapes of the streaming potential curves are fairly similar with the exception of the CASi curve titrated with HCl. Discontinuities within the curves and maxima and/or minima at the ends of the curves are more noticeable in the calcium aluminate glasses than in the silicate glasses. While the location of the initial zeta potential values for the silicate glasses are close to the original pH of the 10 mM KCl solution, the initial values for the calcium aluminates are shifted to a more basic pH.

Figure 10 shows ESEM images of the CAFe and CASi microspheres after measurements started at the pH of the KCl solution and titrated with HCl. While the CAFe surface shows cracking and minor surface roughening, the CASi surface shows severe damage with the formation of gel layers. ESEM images of 2CAFe showed surface damage similar to CASi but less severe, and images of SLS and silica microspheres showed no damage. All calcium aluminate based glasses titrated with KOH from the pH of the KCl solution showed surface damage similar those titrated with HCl described above.

Table V shows that aluminum and calcium leached from the CAFe and CASi glasses during the streaming potential measurements. The CAFe and CASi microspheres both leached ~ 6 wt% of aluminum after 1 hour. The amount of calcium leached between the samples was significantly different however, with CAFe leaching only ~2 wt% and the CASi leaching ~12 wt%. The CAFe sample was also found to have leached ~4 wt% sodium. No leached sodium was detected in either of the electrolyte solutions for the CASi or SLS microspheres. The differences in time in solution between the samples is the result of pre-set parameters that measure the zeta potential after a certain pH difference has been achieved, not at specific time intervals. The CASi released a steady amount of both aluminum and calcium with increasing time and volume of HCl or KOH added, while the CAFe only released aluminum after about an hour during the titration with KOH. The conductivity of the CASi showed random decreases with increasing volume of titratant when a steady increase, like that exhibited by the CAFe, should have been observed.

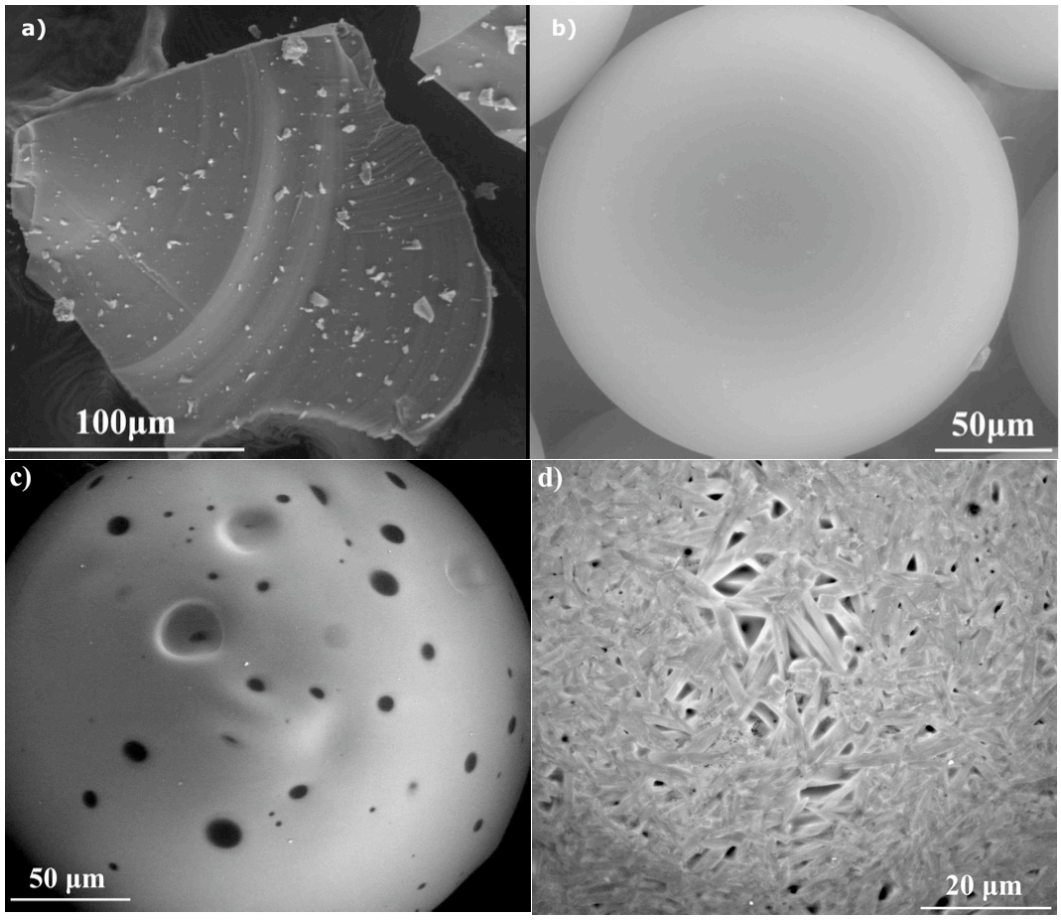

Figure 7. A CA glass particle a) before and b) after going through the flame. A c) pitted SLS microsphere and a d) crystallized CAFe microsphere.

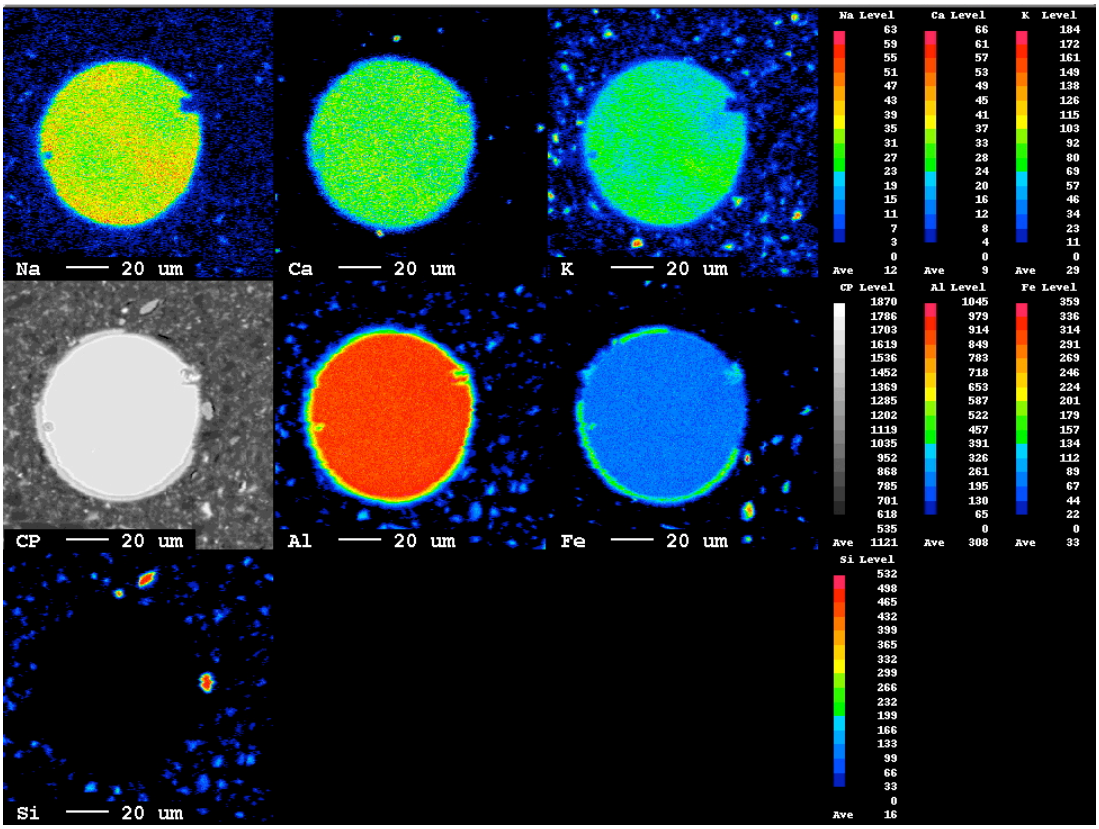

Figure 8. EMP qualitative compositional surface analysis of a CAFe microsphere from the 43-106 μm size range.

Table IV. IEP Values Obtained using Streaming Potential Measurements.

Collected Data - Amorphous		
Oxide	**pH of IEP**	
CAFe	8.1	
2CAFe	9.3	
CASi	8.1	
SLS	3.3	
SiO_2	2.9	
Previously Reported Data - Amorphous		
Oxide	**pH of IEP**	**Reference**
SLS	2-3.4	16, 23
SiO_2	2-3	4, 20
Previously Reported Data - Crystalline		
Oxide	**pH of IEP**	**Reference**
$CaCO_3$	9.5	21
Al_2O_3	7-9.5	4, 17, 18
Fe_2O_3	7-9	4, 17
Al_2SiO_5	8	22
SiO_2	2-3	4, 17, 20

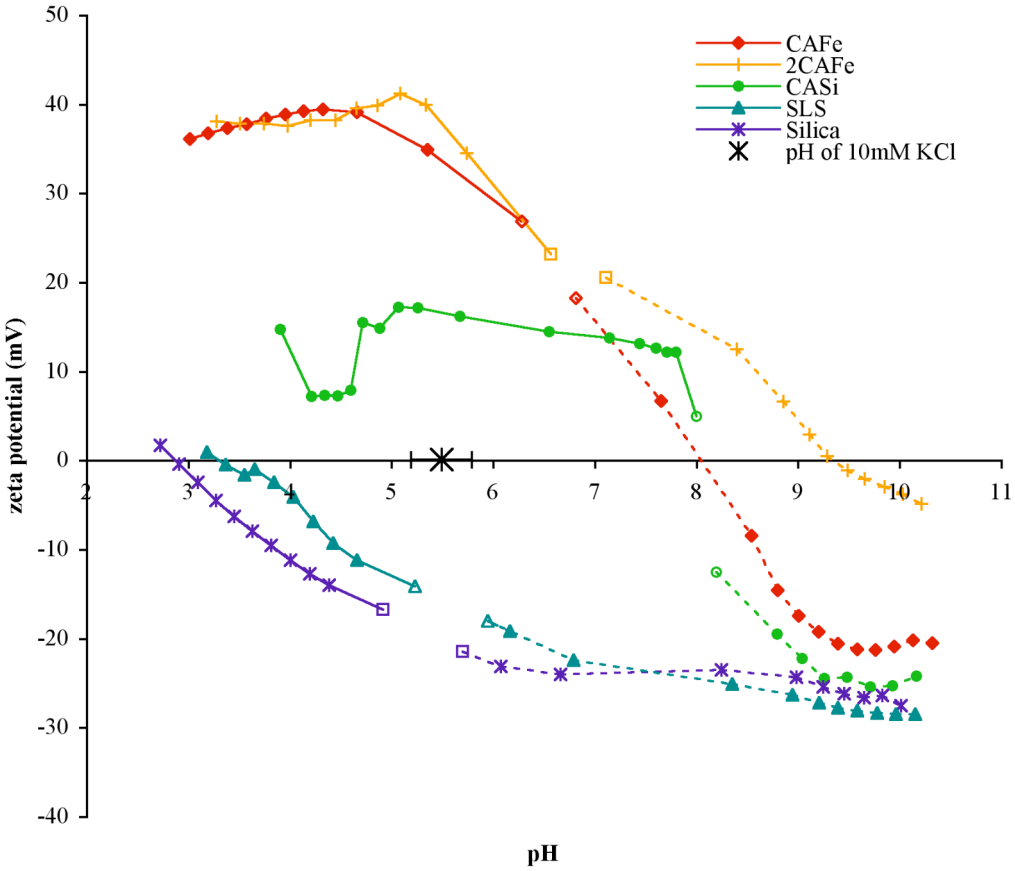

Figure 9. Zeta potential values for various silicate and calcium aluminate based glasses.

Table V. Calcium and Aluminum Ions Leached from the Microspheres During the Streaming Potential Measurements.

Sample	Time in Solution (min)	Volume of Titrant Added (ml)	Solution Conductivity (mS/m)	pH	Al(III) Concentration (mM)	Ca(II) Concentration (mM)
CAFe KOH						
	3.7	0.0	145.1	6.8	0.0	0.0
	12.5	0.4	147.4	8.6	0.0	0.0
	21.2	0.8	149.4	9.0	0.0	0.0
	27.9	1.2	150.5	9.2	0.0	0.0
	59.0	4.1	160.0	10.1	0.23	0.03
CASi HCl						
	4.2	0.0	146.1	8.0	0.00	0.00
	11.5	0.6	110.6	7.8	0.05	0.12
	18.6	1.2	148.6	7.7	0.07	0.13
	32.4	2.4	112.2	7.4	0.09	0.14
	58.7	4.8	151.0	5.3	0.23	0.30
CASi KOH						
	3.8	0.0	146.4	8.2	0.00	0.00
	12.7	0.4	150.3	8.8	0.02	0.08
	23.8	0.8	114.6	9.3	0.09	0.12
	30.6	1.2	155.5	9.5	0.11	0.17
	55.8	4.0	159.9	10.2	0.33	0.24

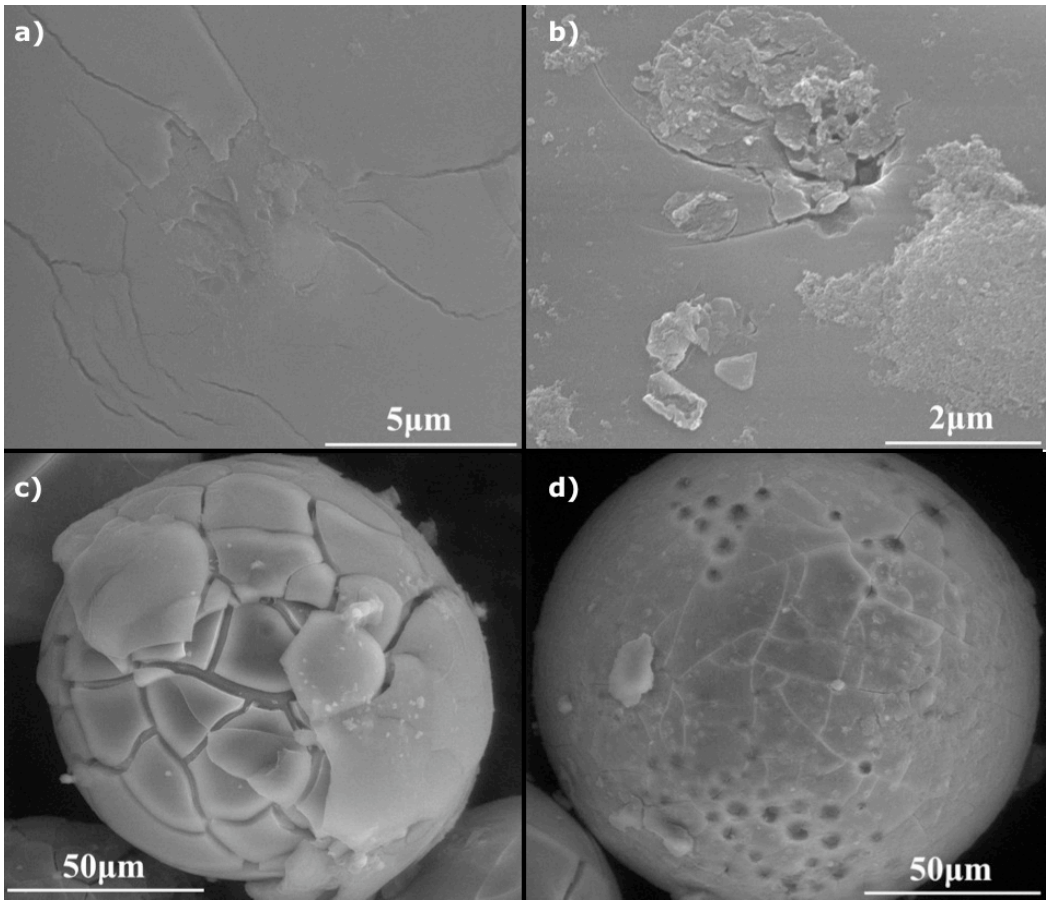

Figure 10. ESEM photos of a) CAFe and b-d) CASi microspheres after streaming potential measurements performed in a 10 mM KCl solution and titrated with 0.1 N HCl.

V DISCUSSION

Zeta potential values obtained by streaming potential measurements are sensitive to changes in the electrolyte flow over the sample surface. Variations in surface morphology that could alter the flow were eliminated through the formation of microspheres which exhibited smooth exteriors and enabled tight, reproducible packing important for a consistent porosity.[1-3,19] Putting the frit into the flame also eliminated fine particles present at the frit surface. The mobility of these fines, along with an increased tendency to degrade, could disrupt the fluid flow over the surface and alter the measured zeta potential values. The calcium aluminates tended to yield more perfectly shaped spheres than the silicates because they form lower viscosity melts with higher surface tensions.[24]

The streaming potential curves confirmed that the greater electronegative silicon cations produce more acidic oxide surfaces than do calcium or aluminum based oxides. Based on the Bronsted acid-base theory, an acidic oxide surface will require a greater amount of protons to neutralize the charged surface and hence exhibit an IEP at lower pH.[3,9] The low chemical durability of the CA and CASi glasses prevented the direct evaluation of changes in the CA surface charge with the addition of silicon or iron oxide. However, based on previously reported IEP data, it is expected that the iron oxide would have little effect on the surface charge, while the addition of silica would cause it to become more acidic. Although the CASi curve in Figure 9 exhibits a lower IEP and overall zeta potential than the CAFe, these results are questionable due to the highly reactive nature of the CASi surface.

Discontinuities in the streaming potential curves indicated that the potential at oxide surface was not in equilibrium with the electrolyte solution during the zeta potential measurement.[1,3] The smoothness of the silicate curves emphasized the greater chemical durability compared to that of the calcium aluminates. When placed in contact with an aqueous solution <30˚C, the calcium aluminates exhibit rapid, congruent dissolution, followed by the formation of hydrated, hexagonal crystalline precipitates.[25-30] The appearance of only a hydrated gel-layer on the microspheres was expected since the crystals tend to form under stagnant conditions in smaller volumes of water. While the

addition of iron oxide appears to provide greater chemical durability than that of silica, the aluminum and calcium were not replaced in equivalent amounts and therefore cannot be directly compared.[31-33]

The validity of the streaming potential curves for the CASi and 2CAFe microspheres is questionable due to their high reactivity in aqueous solutions. When durable oxide materials come into contact with aqueous solutions, the surface charge that develops is a result of adsorption/dissociation reactions with dissociated water molecules or electrolyte ions.[1,3] The equilibrium EDL that develops does so fairly rapidly and only changes upon electrolyte addition or shifts in pH. The chemical interactions between the calcium aluminates and various species present in the aqueous solution never allow the formation of an equilibrium EDL. Dissolution of the network structure releases calcium and aluminum ions into solution, temporarily increasing the ionic conductivity. An increase in ionic strength compresses the EDL, causing a reduction in the magnitude of the zeta potential. The addition of only positively charged ions into the diffuse layer will also reduce the magnitude of the zeta potential, since their presence will reduce the potential difference measured by the electrodes. A larger surface conductivity will also be compounded by the formation of the hydrated gel-layer that can allow increased counter-ion penetration and migration. Some of the leached ions most likely adsorb back onto the microsphere surface, but no significant change in zeta potential is expected since they possess the same sign charge as the surface.[10]

The dissolution of calcium aluminates is normally hindered by the formation of a protective crystalline layer.[25-30] The inability of the CA and CASi to form this layer caused hydrated surface swelling that converted the packed microspheres into a solid plug, inhibiting electrolyte flow past the sample surface. A better understanding of the affects of surface hydration on measured zeta potential could be developed through time interval measurements where no titrations are performed.

Determining an accurate model to describe and measure the potential of CA and CASi microspheres would be nearly impossible due to their dynamic surface reactions and eventual pore structure collapse. However, the more stable hydrated crystalline form should be evaluated because it should produce zeta potential values similar to those of the amorphous glass.[4,5] The hydrated crystalline layer might produce slightly more basic

values since an increased number of basic hydroxide groups are present in the structure. Parks reported that the formation of a hydration layer on crystalline Fe_2O_3 and Al_2O_3 caused an increase in the IEP of about 2 pH units.[4] However, hydration effects are most likely minor in comparison to the drastic differences in surface morphology. The effects of morphology and hydration could be further examined by comparing the zeta potential values measured on the hydrated, hexagonal crystalline phase to those of the hydrated, cubic phase that forms at temperatures >30˚C.

The rapid rate of calcium aluminate hydration is evident in the starting pH of the streaming potential curves. The shift in the initial pH to more basic values indicates the adsorption of H^+ ions onto the –MOH surface.[3,4,9] The greater hydration rate of the CASi than the CAFe is also noticeable in the random drops in conductivity observed during the measurement. A large decrease in conductivity indicates that surface reactions involving the background electrolyte could be occurring. However, the immediate increase in conductivity also suggests that air bubble formation due to disrupted flow over the sample surface could have interfered with the conductivity measurement. The source of solution conductivity changes could be clarified by performing measurements without titrant additions.

VI CONCLUSION

This study confirmed that the surface of an oxide material can be intrinsically controlled through the choice of cation; silicate glasses contain cations with a greater electronegativity than calcium aluminate glasses and therefore exhibit a more acidic IEP. Streaming potential measurements are useful in obtaining zeta potential values when working with oxide materials that are chemically stable in aqueous environments.

Degradation of the CASi glass prevented accurate measurements of the zeta potential over a continuous pH range. The release of calcium and aluminum ions from surface dissolution caused local increases in the ionic strength, reducing the overall magnitude of the zeta potential. The formation of a hydrated gel layer also diminished the magnitude through increased ion mobility at the surface. An increased understanding of these surfaces could be obtained through the examination of the surfaces over time at specific pH values.

While corrections to the zeta potential equation can be made to account for surface conductance, no alteration can realistically account for the constant degradation of the calcium aluminate surface. However, values similar to the amorphous sample could be expected from a sample whose surface was stabilized through the development of the protective hydrated crystalline phase that form on these glasses in aqueous solutions.

VII INTRODUCTION – PART II. SODA LIME SILICATE GLASS UNDER VARIOUS CONDITIONS

A variety of electrokinetic techniques are available to measure the zeta potential of oxide materials in contact with aqueous solutions.[1-3] One of the main factors in method selection is the size and morphology of the material being examined. Streaming potential measurements are commonly used for the examination of micron-sized particles that do not readily form a suspension.

The present study used streaming potential measurements to examine the effects of varying the concentration of a KCl background electrolyte solution and its initial pH, on the zeta potential values of soda lime silicate (SLS) glass microspheres. The effects of pre-treatments with HCl and $Ca(OH)_2$ on the zeta potential of the SLS was also examined.

VIII EXPERIMENTAL PROCEDURE

A. Sample Preparation

SLS microspheres were formed using the procedure explained in Ch 1. III. A.

B. Streaming Potential Measurements

Streaming potential measurements were performed using the procedure described in Ch 1. III. B.

KCl electrolyte concentrations of 0.1, 1, 10 and 100 mM were used to examine the effects of altering the electrolyte concentration on the zeta potential values of the SLS microspheres. KCl was chosen due to its presumed status as an indifferent electrolyte. Zeta potential values were calculated using Equation 5. Titrations were performed with either 0.1 N HCl or 0.1 N KOH and were started at the initial pH of the KCl solution. All the electrolyte concentrations required similar amounts of titrant to shift the pH by comparable amounts. The effects of the initial solution pH on the zeta potential were also examined by adjusting the pH of the solution to high or low values prior to the measurement.

SLS microspheres with surface modifications were examined using a 1 mM KCl solution. The surfaces of the microspheres were modified by placing approximately 1 g of spheres in either a HCl solution with pH 0.6 or a saturated $Ca(OH)_2$ solution with pH 12, for 24 hours at room temperature. The microspheres were filtered from the solution and dried in ambient atmosphere for 48 hours before the streaming potential measurements were performed.

IX RESULTS

Figure 11 shows the potential versus pressure ramps for the different flow directions from the SLS microspheres examined using the 1 or 100 mM KCl solutions. The dU/dp curves for the 1 mM solution are linear while the curves for the 100 mM solution show a large discontinuity at low pressure but become more linear with increased pressure. Measuring the dU/dp for the different flow directions helps to reduce polarization effects and possible uneven particle shifts over time. The curves labeled A represent electrolyte rinsing from right to left while curves labeled B represent rinsing from left to right. Table VI shows the effects of the dU/dp on the zeta potential values. It can be noticed that the cell conductivity increases as the KCl concentration increases, while the cell resistance decreases. For simplification purposes, only specific values that emphasized noteworthy trends were selected from the overall data.

Figures 12-15 show the results of the streaming potential measurements performed on the SLS microspheres under various conditions. The unfilled symbols represent the start of the curves that were titrated with either HCl (solid line connector) or KOH (dashed line connector). The initial pH of the background electrolyte solutions ranged between 5.0 to 5.4. All streaming potential measurement curves are represented in this manner.

Figure 12 shows the effect of altering the electrolyte concentration on the zeta potential of the microspheres. While the 0.1, 1 and 10 mM curves show similar IEP and zeta potential values at low pH, the 10 mM curve exhibits less negative zeta potential values at high pH. The 100 mM curve is considerably different than the other curves with a significant shift in the IEP. In some curves, minima and/or maxima are observed at low and high pH.

Figure 13 shows the effect of initial pH on streaming potential measurements performed on the microspheres in a 1 mM KCl solution. The only similarities between the curves occur between curve 2 and 3 at high pH.

Figure 14 also shows the effects of initial solution pH, but with a 100 mM KCl solution. None of the curves have similar overall zeta potential values, however curves 7

and 8 do appear to have a similar IEP. All the curves show a maxima at low pH and a plateau at high pH.

Figure 15 shows the streaming potential measurements for untreated and surface modified SLS microspheres using a 1 mM KCl solution. Microspheres treated with $Ca(OH)_2$ exhibit a higher IEP than the untreated spheres while the microspheres treated with HCl exhibit a lower IEP. The magnitudes of the zeta potentials above and below the IEP are also significantly different with the $Ca(OH)_2$ treated microspheres exhibiting greater positive values below the IEP and the HCl treated spheres exhibiting greater negative values above the IEP. Discontinuities in the curve are noticeable in the untreated and $Ca(OH)_2$ treated microspheres.

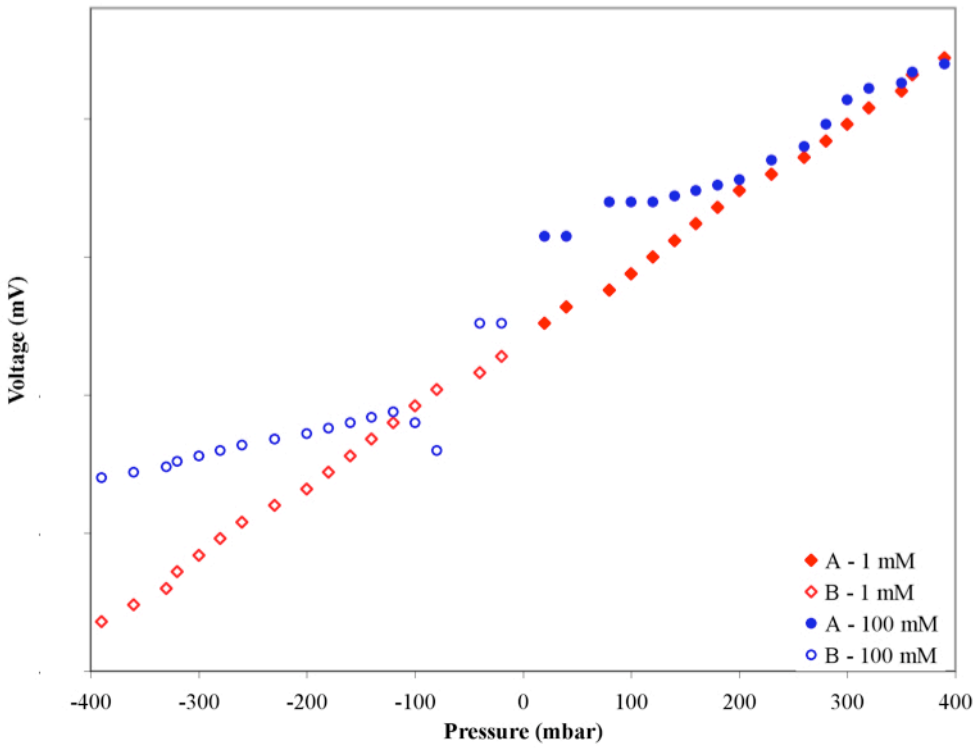

Figure 11. Representative electrolyte flow curves (dU/dp) from the streaming potential measurements performed with 1 mM and 100 mM KCl electrolyte solutions titrated with HCl. Ramps for the 0.1 mM are linear while ramps for the 10 mM exhibit discontinuities but less severe than the 100 mM.

Table VI. Values used to Calculate Streaming Potential.

Samples Titrated with HCl from pH of KCl	pH	ζ (mV)	dU/dp (mV/mbar)	dU/dp correlation	σ_B (mS/m)	R (kOhm)
0.1 mM						
	5.4	-15.7	-7.5E-01	1.00	1.6	188.30
	4.5	-14.6	-5.3E-01	1.00	2.1	142.50
	3.6	-6.5	-6.4E-02	1.00	8.0	38.36
	3.3	0.4	1.6E-03	0.69	19.6	15.73
	3.1	4.4	1.1E-02	1.00	31.1	9.90
1 mM - curve 1						
	5.3	-18.8	-1.1E-01	1.00	12.7	23.42
	4.4	-15.9	-8.9E-02	1.00	13.5	21.27
	3.8	-0.9	-3.8E-03	0.89	17.5	16.35
	3.6	3.5	1.3E-02	1.00	20.7	13.85
	3.2	6.1	1.4E-02	1.00	33.8	8.42
10 mM						
	6.2	-19.3	-1.1E-02	1.00	137.2	3.59
	4.0	-4.2	-2.3E-03	0.99	141.4	3.46
	3.7	-1.1	-5.7E-04	0.75	149.0	3.29
	3.4	-0.6	-3.0E-04	0.64	148.2	2.19
	3.2	0.9	4.3E-04	0.50	158.7	2.05
100 mM - curve 5						
	5.0	-2.5	-1.5E-04	0.49	1210	0.37
	4.3	3.7	2.3E-04	0.59	1223	0.33
	4.1	23.5	1.4E-03	0.99	1233	0.33
	3.4	22.9	1.4E-03	0.99	1249	0.32
	3.1	20.4	1.3E-03	0.98	1256	0.32

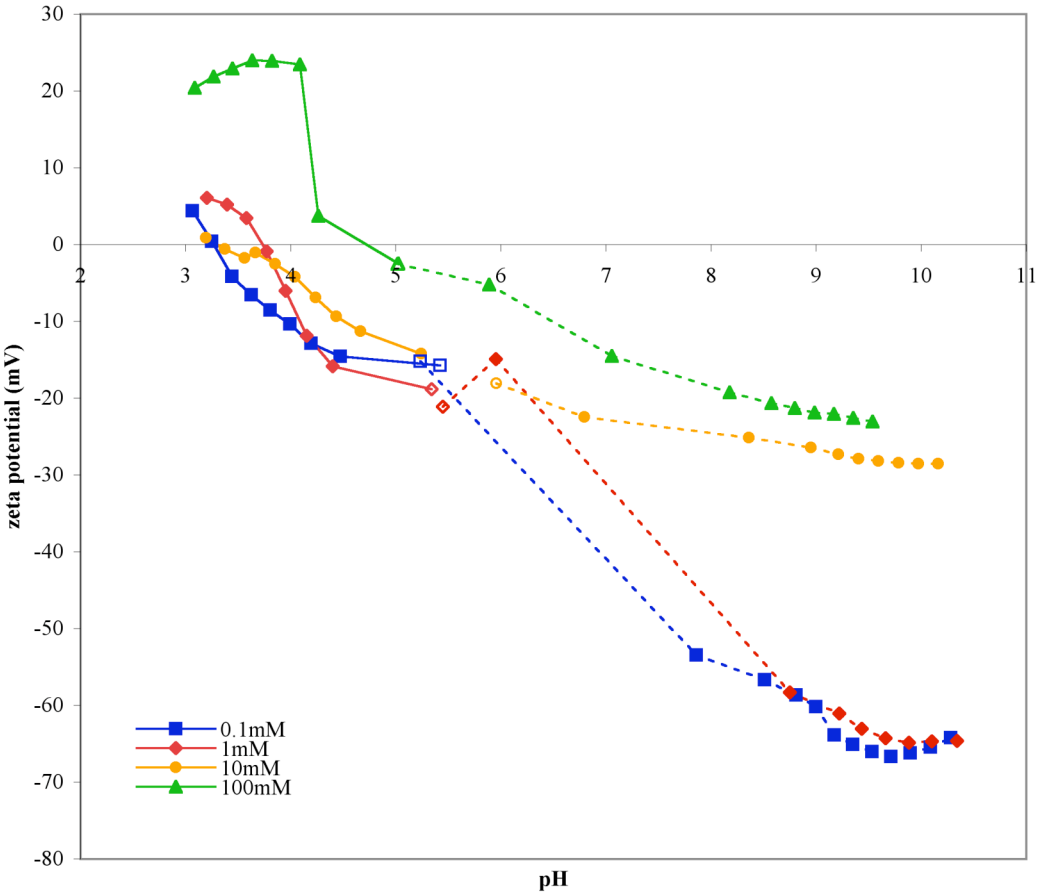

Figure 12. Zeta potential values for SLS frit examined using different concentrations of KCl solution. Curves were all obtained by titrating from the pH of the respective KCl solution with either HCl (solid) or KOH (dashed).

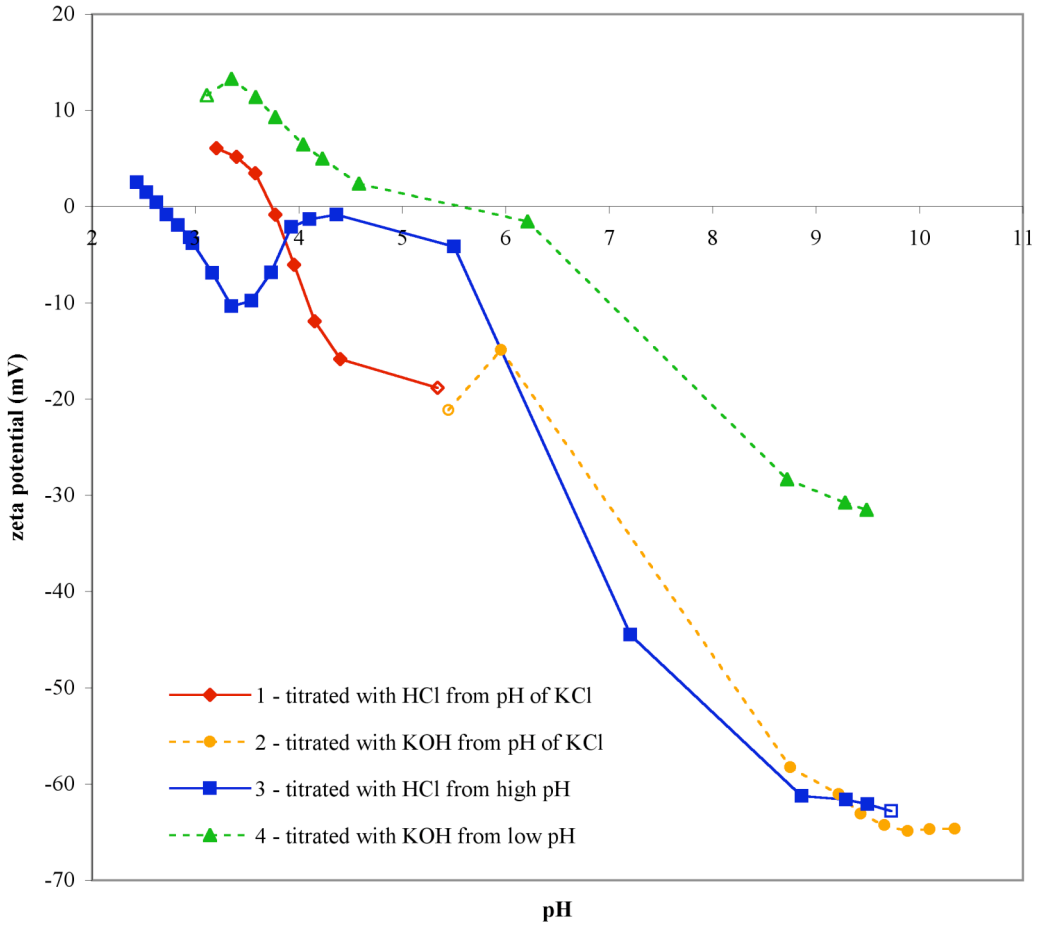

Figure 13. Zeta potential values for SLS frit in a 1 mM KCl solution. Curves were obtained by 1) starting with the original pH of the KCl solution and titrating with HCl (diamonds) or 2) KOH (circles), 3) adjusting the pH of the KCl solution with KOH and then titrating with HCl (squares) and 4) adjusting the pH of the KCl solution with HCl and then titrating with KOH (triangles).

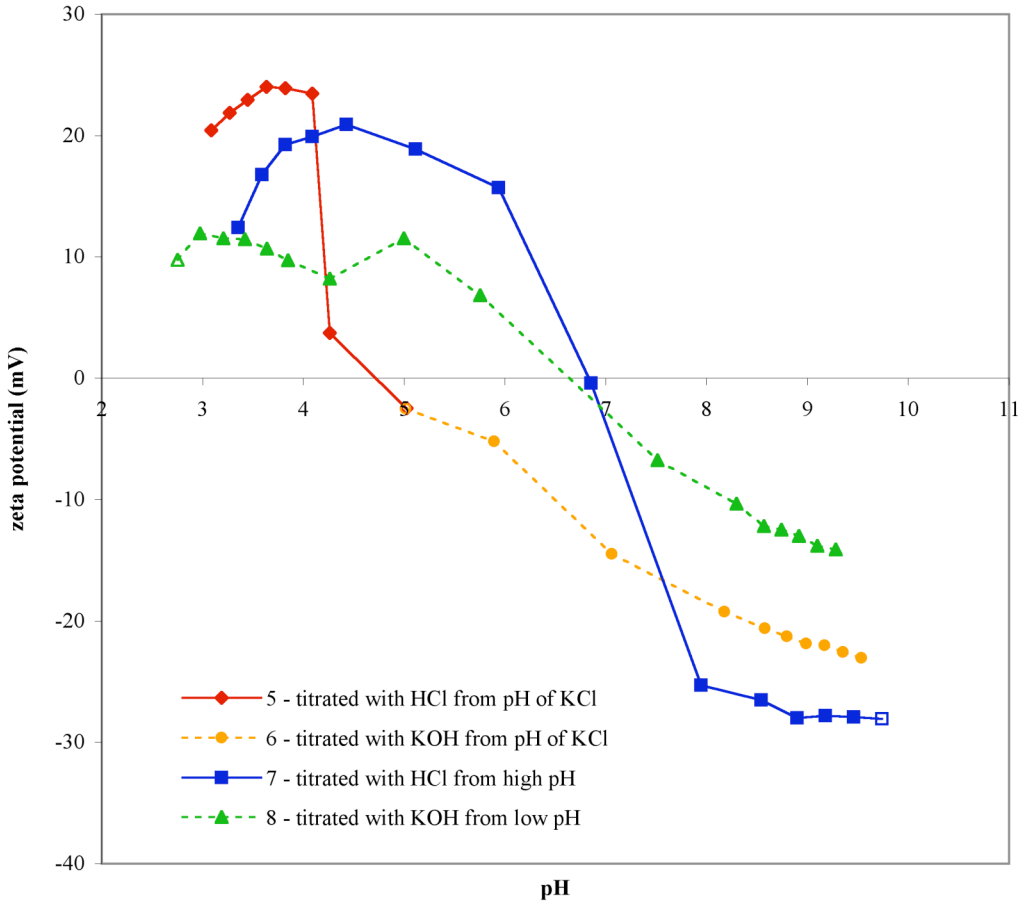

Figure 14. Zeta potential values for SLS frit in a 100 mM KCl solution. Curves were obtained by 5) starting with the original pH of the KCl solution and titrating with HCl (diamonds) or 6) KOH (circles), 7) adjusting the pH of the KCl solution with KOH and then titrating with HCl (squares) and 8) adjusting the pH of the KCl solution with HCl and then titrating with KOH (triangles).

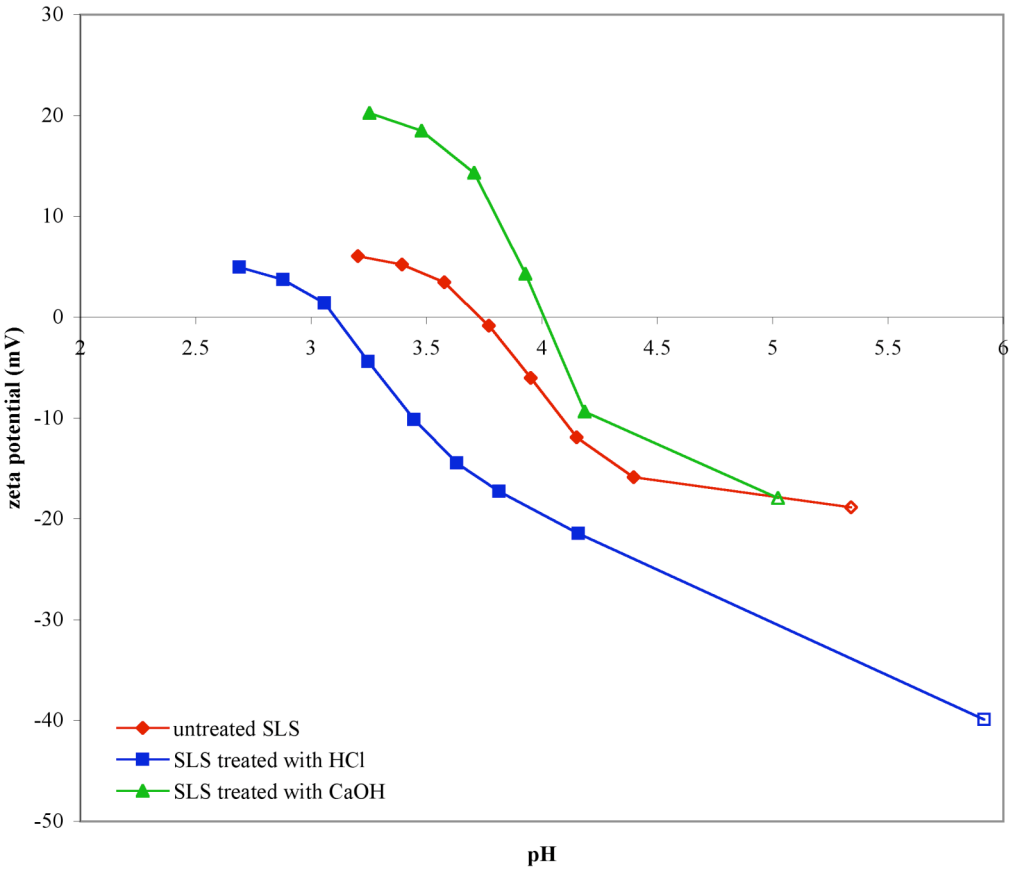

Figure 15. Streaming potential measurements performed in a 1 mM KCl solution for SLS frit (diamonds) and SLS frit treated in solutions of HCl (squares) and $Ca(OH)_2$ (triangles) for 48 hours.

X DISCUSSION

The production of microspheres from the glass frit will slightly alter the surface composition due to the volatilization of Na_2O as the frit passes through the flame.[34,35] The removal of the Na_2O causes two nonbridging oxygens to form a bridging bond, creating a more durable surface comparable to that of silica. However, Na^+ ions are very mobile and could potentially migrate to the surface during microsphere formation. The streaming potential measurements performed on SLS in Chapter 1 showed a higher IEP than silica suggesting that a sufficient amount of alkali and/or alkaline earth ions were still present at the surface.

The effects of changes in the indifferent electrolyte concentration on the zeta potential are well established and described in Ch 1. I. A. 3.[1,3,4] The 0.1, 1 and 10 mM curves in Figure 12 show the effects of EDL compression without chemical adsorption. It is unclear whether the sign reversal at the ends of the streaming potential curves are the result of double layer compression from an increase in ionic strength or specific adsorption of the counter-ions. Curves exhibiting plateaus indicate that the surface has become saturated with charge without the alteration of the EDL. Similarities in the zeta potential values between the 0.1 and 1 mM suggest that EDL compression is not occurring at the concentrations. High ionic strength also appears to cause low dU/dp correlation values ($R^2 \leq 0.7$). Elimination of the points with low correlation values on the 100 mM curves titrated from the pH of the KCl with either HCl or KOH, would give an IEP value around pH 6, closer to the IEP displayed by curves titrated from high and low pH. Low correlation values are also thought to have caused the minima at about a pH of 3 in the 1 mM curve titrated with HCl from high pH. A drastic increase in the ionic strength during the HCl titration could have encouraged the physical adsorption of Cl^- onto the oxide surface, altering the actual dU/dp values that should have been measured.

The appearance of discontinuities and minima around zeta potential values close to zero are most likely the result of difficulties with the instrument measuring a signal. A similar concentration of positive and negative charges present at an oxide surface around its IEP causes only a weak potential to be generated. In this case, the small potential is compounded with the low surface area, and hence low charge density, of the

microspheres. When electrokinetic instruments have trouble measuring a potential, a false signal is sometimes generated that can appear as a surface charge reversal.[1] Accurate zeta potential values will once again be measured after the surface has accumulated enough charge to generate a significant potential.

Chemical adsorption of the K^+ appears to have occurred for the 1 mM curve titrated from low pH and all of the 100 mM curves. Extreme pH can influence the IEP through alterations in the surface chemistry. At low pH, the Na^+ located at the microsphere surface will tend to exchange with the H_3O^+ in the acidic solution.[34,35] While low levels of ion exchange will preserve electroneutrality, higher levels will create a porous, silica-rich gel-layer that can hinder electrolyte flow and facilitate the adsorption of ions from the electrolyte solution.[19] The similarity in size and charge of the K^+ to the leached Na^+ makes it more likely to adsorb to the gel layer than the Cl^-. At high pH this gel-layer is not readily formed since the OH^- groups tend to directly attack the silica network.[34,35] Because of this direct structural dissolution, chemical adsorption of cations due to the formation of a hydrated layer is not likely to occur. This theory was supported by a steady decrease in the bulk conductivity of the solution as the titrant was added to the electrolyte solution. The 100 mM curve started at low pH also showed this trend, while all other curves started at neutral and high pH showed in increase in conductivity with titrant addition.

The basic shift in IEP for the SLS microspheres treated in the saturated $Ca(OH)_2$ solution indicates the chemical adsorption of Ca^{2+} onto the negatively charged SLS surface. Previous studies have also observed an increase in IEP, with di- and tri-valent cations having a greater tendency to chemically adsorb than monovalent cations.[3,6,36] This larger affinity for the oxide surface is thought to be the result of a higher charge concentration in combination with a greater cation to anion ratio larger than unity. While the surface charge was expected to become more basic than observed, the high pH of the saturated $Ca(OH)_2$ solution could have increased surface dissolution, making Ca^{2+} adsorption less likely to occur.[34,35] The appearance of more negative zeta potential values accompanied by a shift in the IEP to a more acidic pH, suggests that treatments of SLS with HCl lead to the leaching of basic alkali and alkaline earth ions. Horn and Onoda observed this effect after pre-rinsing SLS microspheres with concentrated HCl and

deionized water to remove any surface contaminants.[16] This curve does not exhibit the discontinuities observed for the untreated and $Ca(OH)_2$ treated microspheres since mobile ions have already released from the surface.

XI CONCLUSION

Examination of the surface charge on bulk materials and/or non-colloidal particles in aqueous solutions is best performed through streaming potential measurements. Surface examination using other electrokinetic techniques requiring colloidal particles would not have been representative of the flame polished microsphere surface or chemical durability.

While the EKA is capable of providing reproducible measurements with IEP values similar to those commonly reported, users should be aware of several parameters that can alter these results. The background electrolyte should be high enough to negate any effects from sample surface conductivity but low enough so as not to alter the EDL. Initial measurement pH is also important since oxide materials are highly sensitive to reactions with dissociated water molecules. Also, all electrokinetic instruments have difficulty measuring accurate potential values around the IEP of the oxide material.

CHAPTER 2: DNA ADSORPTION ONTO GLASS SURFACES

XII LITERATURE REVIEW

A. Importance of DNA Isolation

Deoxyribonucleic acid, commonly known as DNA, contains all of the information needed to form and maintain a biological organism. DNA consists of four types of monomers, which when arranged into specific sequences are called genes and are the basis for the formation of proteins.[37,38] Since proteins are responsible for most cell functions, different genes can cause drastically different traits to be expressed leading to a large variety of organisms and even significant diversity within the species. Although 99.9% of the human genome is the same, there are 13 DNA segments, consisting of about 3 million base pairs, that are unique to the individual. This unique region is called the DNA fingerprint and is utilized in a wide range of applications ranging from the establishment of paternity to the identification of a crime suspect or a physically unidentifiable victim. This technique is more useful than blood type examination since blood type is not unique to the individual. DNA fingerprinting also requires a lesser amount of sample that does not need to be fresh.

The need for clean, undamaged DNA in the applications discussed above has encouraged the development of easy and reliable isolation techniques. Determining which technique to use depends on the molecular weight of the DNA as well as the desired quantity and purity after isolation.[37-41]

B. Techniques for the Isolation of DNA

DNA isolation techniques begin with lysing the cell membrane and the digestion of proteins and all other cellular content except for the DNA.[37-41] Commonly used quick isolation methods involve protein digestion at high temperatures and/or the precipitation

of the cell lysate using high salt concentrations. The digested or precipitated layer is then removed and the DNA is extracted using alcohol precipitation. These methods isolate DNA quickly but in low yields and are often contaminated with unremoved cell lysate which can lead to DNA degradation. A larger quantity of better quality DNA can be isolated using organic compounds. However, residual organics can inhibit future DNA processing such as replication. The chemical waste produced from organic isolation methods is also toxic and presents an environmental hazard.

One of the safest and most effective methods to isolate high purity DNA is through DNA adsorption onto an inorganic substrate such as silica. The silica surface and the DNA backbone are both negatively charged, and so additional agents must be used to overcome electrostatic repulsion and encourage DNA adsorption. Chaotropic salts are a frequently used additive since they decrease the tendency of the DNA to hydrogen bond with water and also form a positively charged bridge between the DNA phosphate group and the substrate surface. Adsorbed DNA is eluted from the substrate by rinsing the surface with a low salt buffer solution containing a chelating agent which has a higher affinity for the chaotropic agent than the DNA.

The use of oxides that are positively charged at the pH range of DNA purification eliminates the need for the fairly hazardous and costly chaotropic agents. Porous columns packed with hydroxyapatite (HA) powder have been found to isolate a greater quantity of DNA from cells than silicate based materials in the absence of a chaotropic agent.[39,42] Because the DNA is also more tightly bound to the HA surface, a concentrated phosphate buffer solution is needed to eluted the DNA since it has an even higher affinity for the HA surface than the EDTA.

C. Structure of DNA

DNA is a single or double stranded polymer chain made up of subunits called nucleotides shown Figures 16 and 17.[38,42-48] Each nucleotide consists of a five carbon sugar ring, a phosphate group and one of four nitrogenous bases. The phosphate groups form strong bonds between the fifth and third carbon atoms (5' and 3') of the sugar rings to form a sugar-phosphate backbone. Under physiological conditions (neutral pH, relative humidity $\geq$ 92% and various electrolyte ions), the sugar-phosphate backbone will carry a

negative charge due to the phosphate group which has an acid dissociation constant of ~2.[49] Counter-ions such as calcium and sodium must be present in solution at sufficient concentration to neutralize the repulsive forces between the negative charges on the phosphate groups. The nitrogenous bases, adenine (A), guanine (G), cytosine (C) and thymine (T), are separated into two types depending on their structure; A and G are called purines and are made up of a five- and six-membered ring compound while C and T each consist of a six-membered ring and are called pyrimidines.[38,42-47] Nucleotide bonding is specific, with A only bonding with T and C only bonding with G. This complementary pairing is due to the highly directional nature of the hydrogen bonding between molecules; A and T have two available hydrogen bonds while G and C have three. The extra hydrogen in the G-C bond makes it about 30% stronger than the A-T bond and is one of the factors in determining the melting temperature of a specific DNA molecule.

The most stable and commonly observed DNA structure in physiological environments is called B- form.[38,42-47] A schematic of this structure is shown in Figure 17 with specific properties listed in Table VII. In this structure, two complementary strands of nucleotides can interact with each other through hydrogen bonding of the nitrogenous bases resulting in a twisted "ladder" like structure. This structure exhibits a greater stability in physiological environments than the other naturally occurring forms since it has the smallest repulsive phosphate-phosphate electrostatic term under these conditions.[50] The right handed helical structure is believed to be the result of stacking forces between the nucleotides, with stronger forces encouraging a more helical shape.[38,42-47] Stacking forces arise due to the hydrophobic nature of the nucleotide rings perpendicular to their hydrogen bond and from the pi bonds occurring between the aromatic rings of bonded base pairs. Each nucleotide is vertically spaced about 3.4 Å apart and is oriented nearly perpendicular to the sugar phosphate backbone. However, the alignment is imperfect between the base pairs and leads to the formation of two distinct groove widths in the helix; the wide major groove and the narrow minor groove. Since bases conform to a specific orientation within the helical structure, the same atoms will always be visible for a specific nucleotide depending on whether it is located in the major or minor groove. For example, when examining a B-DNA molecule the C-6, N-7 and C-8 atoms of the purine rings and the C-4, C-5 and C-6 of the pyrimidine rings will always be

visible in the major groove, while the C-2 and N-3 of the purine and the C-2 of the pyrimidine is always visible in the minor groove.

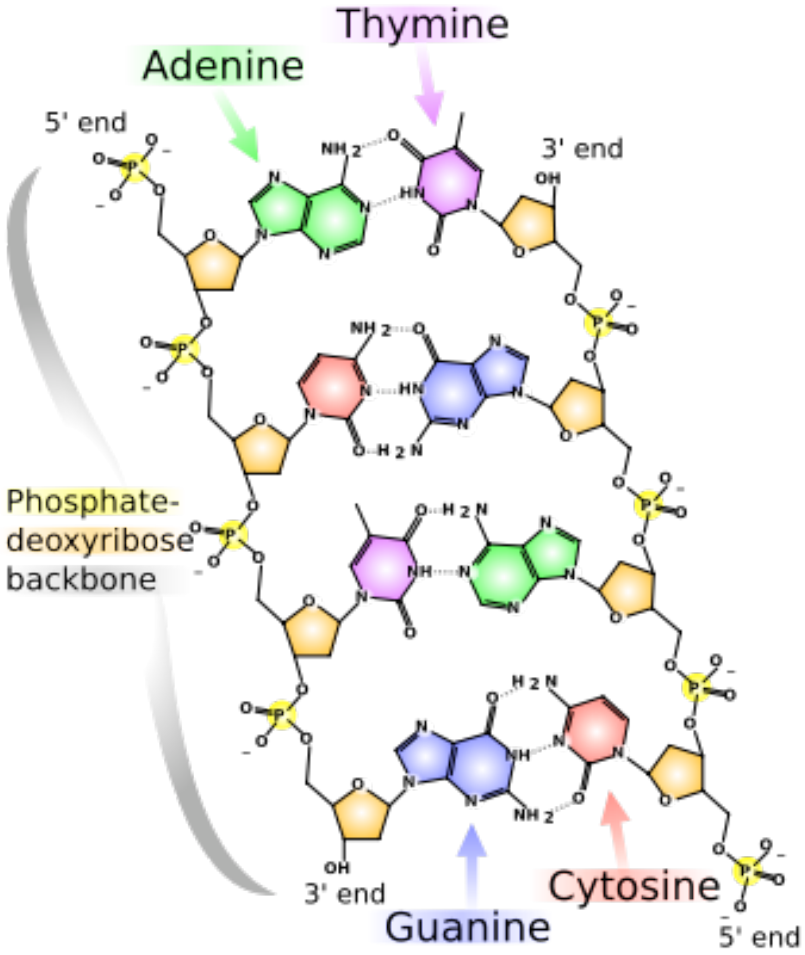

Figure 16. Nucleotides of DNA.[48]

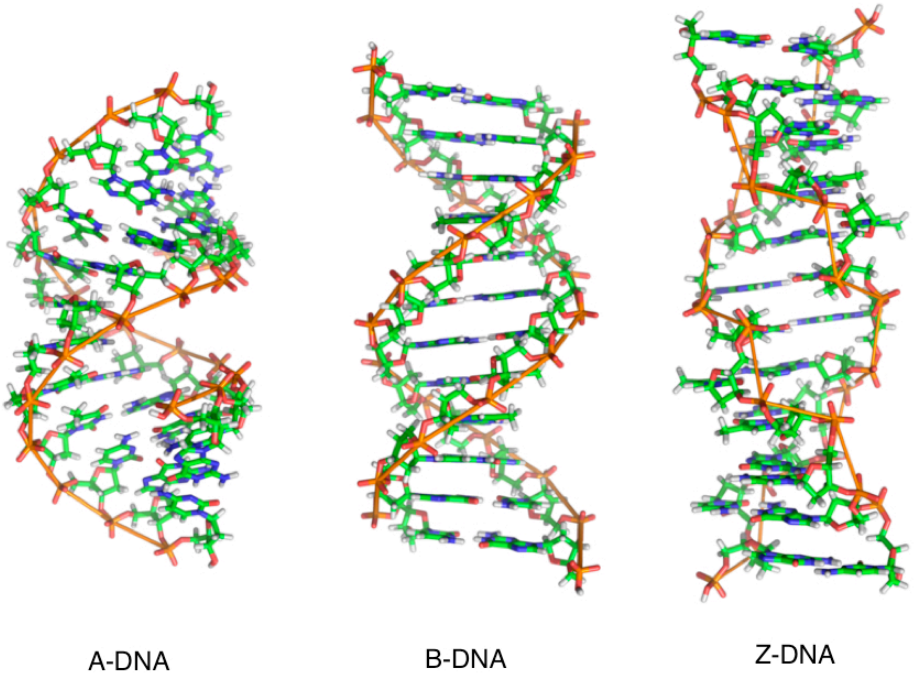

Figure 17. Structure of A-, B- and Z- form DNA.[48]

Table VII. Specific Properties of A-, B- and Z- form DNA.

Geometry Attribute	A-DNA	B-DNA	Z-DNA
Helix handedness	right	right	left
Repeating unit (bp)	1	1	2
Rotation per bp	33.6°	35.9°	60°/2bp
Avg. bp/turn	10.7	10.0	12.0
Inclination of bp to axis	+19°	-1.2°	-9°
Rise/bp along axis (A)	2.3	3.3	3.8
Pitch/turn of helix (A)	24.6	33.2	45.6
Diameter (A)	25.5	23.7	18.4

* base pair - bp

D. DNA Environment in a Eukaryotic Cell

All living organisms other than bacteria consist of eukaryotic cells which are characterized by membranes surrounding the nucleus and other organelles.[38] DNA is contained in the nucleus and is attached to proteins in a complex known as chromatin. The chromatin is surrounded by a viscous liquid called nucleoplasm which contains nucleotides and enzymes. The nucleus also contains a "sub-organelle" called the nucleolus which is composed of a fibrous bundle of ribosomal DNA and proteins. DNA located inside the nucleus is used in the control of gene expression, while the DNA located inside of the nucleolus is involved in the formation of ribosomes which assemble proteins. Our inability to mimic or even determine cellular DNA conditions makes it difficult to predict its conformation in this environment. While B-DNA is the most common form, various conditions in the surrounding medium are likely to cause conformational changes to either sections of the helix or entire strands.[42,46,47,50-57]

E. DNA Configuration and Stabilization in an Aqueous Environment

1. Various DNA Configurations

Depending on the base pair sequence and solution environment, entire strands or sections of the B-DNA helix can be altered to either the A- and/or Z- forms shown in Figure 17. The specific properties of the helices, listed in Table VII, were determined using x-ray diffraction on single crystals of DNA.[53,55,58] Although structural changes will affect the interaction of DNA with light and molecules in solution, key properties such as specific base pair binding are not affected.[42,46,47] While the A-DNA conformation has never been detected in cells, the Z- form is known to exist in small segments of B-DNA strands and is thought to have a role in gene expression.[42,46,47,53,55,58]

2. Influence of Cation Type and Concentration

The stability of the B-DNA double helix is highly dependent on the type and concentration of cations in solution.[50,52-54,56,57,59,60] Monovalent cations tend to shield and stabilize the negatively charged phosphate groups through the formation of weak ionic or electrostatic bonds.[53,57] These ions have also been found to interact directly with the

nitrogenous bases in A-T dominated sections of the minor groove. When direct bonding occurs, a water molecule is typically released since both the cations and the DNA molecule are hydrated. Divalent cations however, can use their hydration sphere to form both indirect and/or direct covalent bonds with the DNA without the release of water. FTIR spectroscopic methods performed by Ahmad et al. showed that calcium ions preferred to bond directly to the negatively charged phosphate backbone. Weaker, indirect bonds were also found to form in the G-C rich sections of the major groove, specifically with nitrogen atoms on G bases.[52]

Structural modifications to the B-DNA form will occur as the electrolyte concentration is varied from a physiological environment. Biological fluids normally contain ~1-4 mM/L of divalent cations such as Ca^{2+} and Mg^{2+} and $\geq$ 100 mM/L of monovalent cations such as sodium.[61] Negatively charged electrolytes are also present but do not interact directly with the phosphate backbone.[42,46,47] While whole strands can undergo conformational changes, it is more common for only sections of the helix to transform. For example, under low salt concentrations the G-C rich nucleotide sequences of the B-DNA will move toward the major edge of each base pair creating the thicker A-DNA helix[53]. While high ionic strength solutions tend to favor the Z-DNA configuration, alternating purine and pyrimidine sections can also cause this conformation to be present under physiological salt concentrations.[42,46,47,53]

When the ionic strength becomes very low, the negative charges on the phosphate backbone begin to repel one another, causing the double helix to separate into two strands. This process, called denaturing, is reversible and is performed in procedures where single strands are necessary, such as in DNA replication.[42,46,47]

3. Influence of Water Molecules

The hydrophilic exterior and the hydrophobic interior of the DNA molecule are instrumental in the formation and stability of the double helix in aqueous solutions.[42,46,47,53] The double stranded helical conformation is favorable over a single stranded structure because the hydrophobic bases become shielded from the water molecules as they bind to one another. This configuration also allows the hydrophilic phosphate groups to become highly solvated.

Drew et al. found that water molecules situated within the minor groove of B-DNA, form an ordered network with the phosphate groups.[53] This network extended down the groove and preferentially occurred in A-T dominated sections. Water molecules associated with the major groove and the phosphate backbone were found to be structurally disordered. When the relative humidity was decreased down to 75%, the dehydrated helix tended to transform to A-DNA.[55] While A- or Z- can form depending on the base pair sequence of the strand, transitions were found to occur readily in G-C rich sections and rarely in the A-T rich segments.[53,55]

4. Influence of Temperature and pH

An increase in temperature can cause the double helix structure to denature. The temperature at which half of the DNA strand is denatured is called the melting temperature, and is based on the length and specific nucleotide sequence.[42,46,47,62] Strands with larger amounts of triply hydrogen bonded G-C will take more energy to melt than strands containing larger amounts of doubly hydrogen bonded A-T. The melting temperature for short strands ($\leq$ 20 nucleotides) can be approximated by adding 2˚C for every A-T pair and 4˚C for every G-C pair. This calculation cannot be used for larger strands however, since nearest neighbor interactions between adjacent nucleotides must also be accounted for.[62] While denaturation can be reversed by decreasing the temperature, the sequence and time at a specific temperature must be carefully controlled or complementary strands will not recombine in the correct manner.

Alkaline pH can also cause the DNA to denature.[40,44,45] At pH $\geq$11, the aromatic rings of the bases tend to ionize, disrupting their ability to participate in hydrogen bonding. This method of denaturation is often preferred to changes in temperature which can cause fragmentation due to the breakage of the phosphate bonds between the nucleotides. Acidic pH can also cause fragmentation since H^+ disrupt the strong covalent bonds between the sugar and phosphate groups that make up the DNA backbone.

F. Biological Buffers used for DNA Storage

Buffers used during *in vitro* testing of biological systems must maintain specific conditions that mimic the environment in the cells.[63,64] Ideal buffer properties include

1) a pKa which can remain between pH 6 and 8 through the addition of various types and concentrations of ions, temperature and exposure to atmospheric CO_2
2) any complexes formed with metals should be soluble and have known binding constants
3) a high solubility in aqueous media to enable the formation of concentrated solutions, but a low solubility in all other solvents
4) no light absorption above 240 μm since this can greatly interfere in the UV examination of biological molecules

One of the most commonly used buffers is Tris(hydroxymethyl)aminomethane (Tris) because of its low cost and its availability in highly purified forms.[63-67] The buffering ability of the Tris molecule, shown in Figure 18, is due to its primary amine which can protonate or deprotonate with changes in pH. Its slightly basic nature (pKa ~8.3) tends to keep DNA ionized between pH 7-9 and therefore soluble in solution.

The limitations of the Tris buffer include its sensitivity to changes in temperature (a decrease in pKa of ~0.03 for every ˚C rise in temperature) and its inability to bind with cations commonly present in storage solutions.[63-67] Contamination of a Tris based DNA storage solution with di- or tri-valent cations can cause conformational changes, or in most severe cases, fragmentation. Cations can also cause DNA degradation since their presence is often needed in enzymatic reactions used to sever the base pairs. To prevent this damage, a chelating agent, such as Ethylenediaminetetraacetic acid (EDTA), is often added to the Tris buffer.[46] EDTA is a polyprotic acid that is able to form 1:1 complexes with di- and tri- valent cations and various organic molecules. The EDTA molecule, shown in Figure 19, has two groups of lone pair electrons on the amine groups and four carboxylic acid groups. The carboxylic acid groups are fully protonated at low pH, but become fully deprotonated at higher pH and are able to chelate. Figure 20 shows a schematic of a metal-EDTA complex with a metal ion.

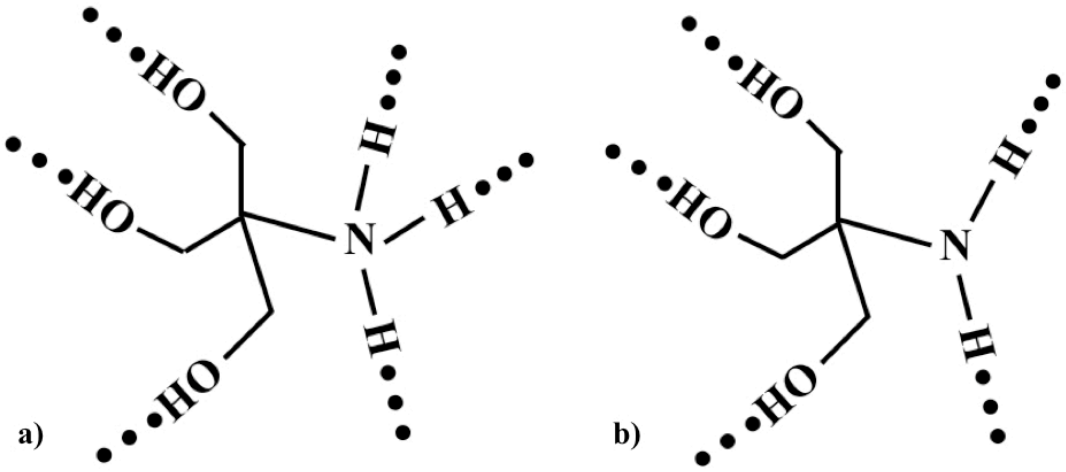

Figure 18. A a) protonated and b) deprotonated Tris molecule.

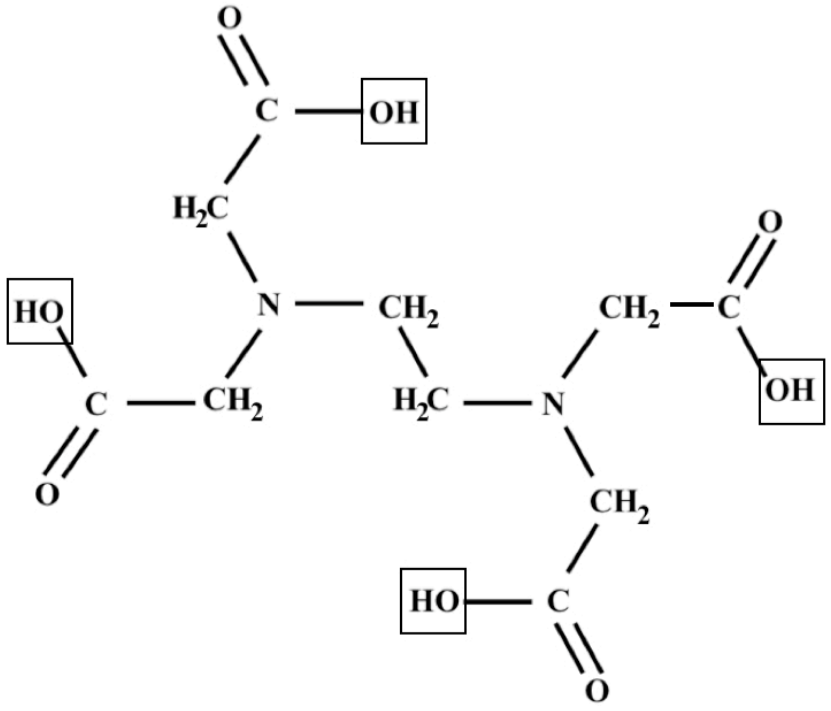

Figure 19. Fully protonated EDTA molecule. Removal of the H^+ from the boxed in OH groups represents the fully deprotonated form.

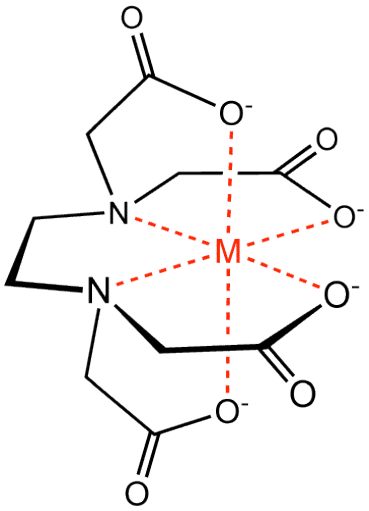

Figure 20. Schematic of an EDTA/metal ion complex.[48]

G. Concentration and Conformation Determination of DNA

Ultra Violet (UV) absorbance spectroscopy is one of the quickest and easiest methods used to determine the concentration of DNA in solution**.** The heterocyclic aromatic rings of the base pairs absorb light between 200 and 300 nm.[42,46,47,62] While each of the bases exhibits a unique absorbance spectrum, these curves blend together when examining a strand of DNA to produce a curve with only one maximum at ~260 nm. However, the measured absorbance value for a strand is about 40% lower than the absorbance of the individual base pairs in solution. This decreased absorbance is due to stacking interactions between the base pairs which disrupt the aromatic rings ability to interact with light. This effect is also observed when a double stranded helix denatures into single strands.

UV absorption is also used to determine if there are any contaminants present in solution; protein contamination is visible at ~280 nm, salts and/or chaotropic agents absorb at ~230 nm and an absorbance band at ~320 nm indicates the presence of insoluble light scattering components.[59]

UV light can also be used to examine the chiral structure of the DNA double helix. A chiral molecule will absorb the clockwise component of circularly polarized light differently than the counterclockwise component.[42,46,47,62,68-70] Circular dichroism

(CD) spectroscopy measures this absorption difference between 200 and 300 nm to determine the conformation of DNA in solution. Figure 21 shows the CD spectra for a double helix in A-, B- and Z- conformation. Combinations of these curves will be observed if parts of the same strand are in different conformations.

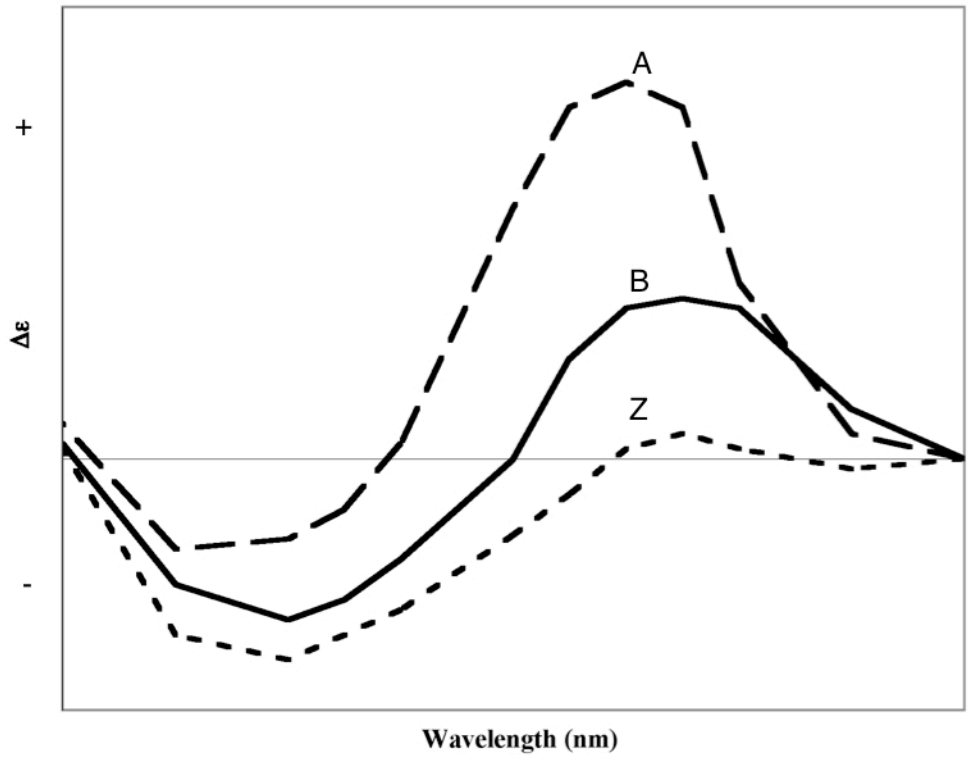

Figure 21. CD spectra of A-, B- and Z- DNA.

XIII INTRODUCTION

The isolation of DNA from cell debris is important in a wide range of applications ranging from the establishment of paternity to the identification of a crime suspect or a physically unidentifiable victim.[37,38] Commonly used quick isolation methods often involve chemicals that can lead to DNA degradation and are toxic to both humans and the environment.[38-41] One of the safest and effective small scale isolation techniques utilizes the electrostatic interactions between the negatively charged DNA backbone and a silica scaffold.[12,14,40,41] Because both the DNA and the silica surface exhibit a negative charge at the pH of the solutions used during isolation, electrostatic attractions are produced through the addition of chaotropic salts to the DNA containing solution. Chaotropic salts decrease the tendency of the DNA to hydrogen bond with water molecules and also provide positive charges which can form salt bridges between the DNA and the glass surface. Creating a material with an inherent positively charged surface could provide an increase in the electrostatic attraction, therefore allowing a greater amount of DNA to be isolated without the use of fairly costly and moderately hazardous chaotropic agents.

Calcium aluminate glass microspheres were examined as a possible scaffold material for the isolation of DNA. The results from Chapter 1 showed that calcium aluminate-based glasses exhibited a positively charged surface at the pH of the solutions commonly used during DNA isolation. The use of glass samples has advantages over positively charged crystalline materials because of its flexibility in both chemical composition and form. Due to the calcium aluminates tendency to be chemically unstable, the effects of ion dissolution on DNA conformation were also examined.

XIV EXPERIMENTAL PROCEDURE

A. Sample Preparation

The formation of the calcium aluminate and SLS microspheres used in these experiments was described in Ch 1. III. A. Smaller frit sizes were also used to produced microspheres in the size ranges 43-106 μm and <43 μm.

B. Microsphere Surface Area Estimation and Environmental Scanning Electron Microscopy

The procedure for ESEM examination was discussed in Ch 1. III. A.

The surface area of the microspheres was estimated using density values obtained from helium pyncnometry and microsphere diameters measured using ImageJ on ESEM images. The microspheres were assumed to be solid through visual ESEM examination and after density measurements using the Archimedes method on bulk samples produced similar values to those obtained using helium pyncnometry. An 11 point BET measurement was used to measure the surface area of a commercially available DNA isolation filter.

C. DNA Adsorption and Isolation from Cells

A 10 mg/ml calf thymus DNA solution from Invitrogen® was diluted to various concentrations in a 1 M (12 wt%) Trizma® hydrochloride buffer solution at pH 7.4 (Tris) from Sigma®. Diluted solutions were stored at -20˚C until use, when a desired amount was extracted and allowed to equilibrate at 22-25˚C before adsorption experiments were performed. All experiments took place in this temperature range.

DNA adsorption experiments were performed using various incubation times (0, 1, 5 or 15 minutes) in solutions used for the microsphere pre-rinse, and DNA attachment and elution. CA, CASi, CAFe and SLS microspheres were weighed out to 0.1 $\pm$ 0.0003 g and placed in filtered centrifuge tubes from Pall Life Science with a filter pore size of 0.45 μm. Pre-rinsing with 100 μl of Tris was performed and included any microspheres remaining on the side of the tube. The samples were gently agitated for the duration of

the pre-rinse. The tubes were then centrifuged for 2 minutes at ~14,000 g to remove any excess solution before incubation in the DNA containing solution. All centrifuging was performed using these parameters because it recovered almost all of the solution. The filter containing the microspheres was removed, placed into a clean tube and then incubated with 100 μl of a 1 mg/ml DNA solution. A 1 mg/ml solution was chosen because it produced UV absorbance values in a range previously determined to provide reproducible values.[62] After centrifuging, the filters were placed in clean tubes and rinsed with de-ionized water to elute any adsorbed DNA from the microspheres.

DNA adsorption experiments using a 0.1 mg/ml DNA solution suspended in a 0.35 wt% (30 mM) Tris solution were also performed on the CAFe and SLS microspheres, as well as a commercially available DNA isolation column from Qiagen®. The Qiagen® filter contained a silicate mat composed of fibers ~2 μm in diameter. CAFe microspheres in the size ranges 106-150 μm, 43-106 μm and <43 μm were used during adsorption studies. Only the larger two size ranges were used for the SLS microspheres since no microspheres in the <43 μm size range could be produced. The microspheres and the Qiagen® filter were incubated in 50 μl the 0.35 wt% Tris pre-rinse solution for 2 minutes and then centrifuged. Microsphere sample size was kept to 0.02 g and not agitated during incubation to mimic the conditions used during the nucleic acid isolation from cells described below. The samples were incubated with the 0.1 mg/ml DNA solution and one of the various elution buffers for 1 minute in succession, with centrifuging performed in between.

Nucleic acid isolation from mouse leukaemic monocyte macrophage cells (RAW2647 cell line, American Type Tissue Culture Collection) was performed using the Qiagen® filter and CAFe and SLS microspheres in the 43-106 μm size range, and on the <43 μm CAFe microspheres. Isolation was performed using the Qiagen® protocol, provided in Appendix A, with both DNA and RNA isolation since no RNA degrdation enzymes were added to the cell lysate. The various buffer solutions used during the isolation procedure are listed in Table VIII. Solutions from both the cell isolation and 0.1 mg/ml DNA solution were examined using both UV absorbance and gel electrophoresis.

Table VIII. Buffer Solutions used During Nucleic Acid Isolation from Cells.

Name	Component
Qiagen Lysis buffer - AL	guanidine hydrochloride
Qiagen 1st wash buffer - AW1	guanidine hydrochloride
Qiagen 2nd wash buffer - AW2	unknown
Qiagen elution buffer - AE	10 mM Tris 0.5 mM EDTA pH 9
High Phosphate Buffer - PE	30 mM Tris 30 mM Na_2HPO_4 pH 8
High EDTA buffer - EE	30 mM Tris 30 mM EDTA pH 8
50-50 Mixture of the PE/EE buffers	30 mM Tris 15 mM Na_2HPO_4 15 mM EDTA pH 8

D. Ultra-Violet Spectroscopy

The microsphere pre-rinse, as well as the DNA attachment and elution solutions made in Ch 2. XIV. C., were examined using a UV spectrometer (UV/VIS/NIR Spectrometer, Perkin Elmer, Waltham, MA). UV examination was performed by placing 40 µl of solution into a UV transparent cuvette containing 1 ml of a Tris-EDTA buffer solution at pH 7.4 (Tris EDTA) from Fluka®. The Tris EDTA buffer was chosen because of its good buffering capacity. Optical absorption spectra were collected from 200 to 350 nm to examine the UV absorption band of the DNA base pairs at ~260 nm, with salt absorption visible at ~230 nm and any insoluble light scattering components visible at

~320 nm.[62] The concentration of DNA adsorbed to the microspheres was calculated by taking the difference between the absorbance of the original DNA solution and the DNA solution that had been rinsed over the microspheres. The amount of DNA that was eluted from the microspheres was also calculated based on the absorbance of the original DNA solution. The calculations for the amount of DNA adsorbed to the microspheres are shown in Appendix B.

UV spectra were collected for DNA solutions mixed with solutions containing different concentrations of calcium and aluminum. The preparation of these solutions is discussed in Ch 2. XIV. F. These solutions were measured in both Tris and Tris-EDTA background solutions to examine the effects of EDTA on the salt solutions.

UV examination of DNA was also performed on a different spectrometer that does not require the use of cuvettes (NanoDrop ND-1000, Thermo Scientific, Waltham, MA). DNA concentration quantification with the 'drop' spectrometer eliminates the need to place the DNA solution in a buffer filled cuvette which dilutes the sample and can lead to inaccurate measurements. In this instrument, 1-2 μl of sample is placed between two fiber optic cables. A pulsed xenon flash lamp sends light through the droplet which has been compressed to a 1 mm path length. The instrument is able to provide accurate UV/Vis readings on DNA concentrations between 2-3700 ng/μl, 50x higher than the concentrations measured by the standard cuvette spectrometer used above. The concentration of DNA was calculated using the Beer-Lambert law and is performed in Appendix B. The NanoDrop was used in studies involving the 0.01 mg/ml DNA solution and the cells.

E. Inductively Coupled Plasma-Optical Emission Spectroscopy

The amount of ions leached from the microspheres during mixing with the DNA and Tris solutions were tested using ICP-OES. The microspheres were treated using the same procedure for DNA attachment described in Ch 2. XIV. C. The solutions were tested for all the cations present in the various glass compositions. ICP-OES samples were prepared by placing 80 μl of the centrifuged solution into a mixture of 1 ml de-ionized water and 1 ml nitric acid. The nitric acid was used to help inhibit precipitation of leached species from solution.

F. Circular Dichroism Spectrometry

A circular dichroism spectrometer (Circular Dichroism (CD) Spectrophotometer, AVIV, Lakewood, NJ) was used to examine the conformation of the DNA that had been mixed with either the glass microspheres or solutions containing different concentrations of calcium or aluminum. The B-form DNA used in this study exhibits a CD spectra with maxima and minima of similar magnitudes at ~278 and ~248 nm, respectively. Solutions were examined from 200 to 350 nm using a silica cylindrical cell with a 0.1 mm path length.

The DNA solutions were mixed with the CA and CAFe microspheres using the same procedure described in Ch 2. XIV. C. At least 300 µl of solution was needed to fill the cylindrical cell and to ensure that there was enough DNA to provide an accurate measurement, 90 µl of the centrifuged DNA solution was mixed with 300 µl of Tris.

One calcium solution was formed from the CA glass by mixing 2 g of the <43 µm frit with 12 ml of Tris for 24 hours. The solution, called CAs to identify it from the CA, was separated from the powder through centrifuging and the concentration (mM) was determined using ICP-OES. Other calcium solutions were made by mixing the appropriate amount of calcium chloride (CCl) or calcium nitrate (CN) into Tris to form a 100 mM solution. The aluminum solution was made in the same manner as the calcium salt solutions but using aluminum nitrate (AN) instead. Varying amounts of the different calcium and aluminum solutions were mixed with the DNA solution and Tris to simulate different ion concentrations.

G. Thermal Gravimetric Analysis

Thermal gravimetric analysis (TGA) was used to examine residual solution remaining on the microspheres after centrifuging. CA and SLS microspheres were treated with de-ionized water and Tris for the same time intervals as those experienced during DNA adsorption experiments. The samples were labeled with the appropriate microsphere composition followed by: a number for incubation time in Tris, a number and “di” for incubation time in de-ionized water, a number-number for two successive incubation periods in Tris and a number-number “di” (ex 15-15di) for incubation in Tris followed by incubation in de-ionized water. The numbers correspond to the incubation

time in minutes. Samples were placed in silica pans and measurements were performed from room temperature to 400˚C with a 10˚C /min heating rate.

XV RESULTS

A. Microsphere Surface Area Estimation and Surface Examination

The 43-106 μm CAFe and SLS frit produced microspheres similar to those produced from the 106-150 μm frit but with the microspheres exhibiting diameters close to either ~50 or ~80 μm. The CAFe <43 μm frit that passed through the flame produced well shaped microspheres with almost no irregularly shaped debris. The SLS <43 μm frit did not produce microspheres in this size range, instead the frit formed into agglomerated particles or hollow microspheres with diameters >150 μm. The specific surface area of the Qiagen® filter was obtained by multiplying the BET measured surface area by the mass of a single filter bed. Table IX shows the various properties for the samples used in the DNA isolation experiments.

The ESEM image of the CA microspheres in Figure 22 showed that while Tris residue had collected in between the microspheres and in small patches on the surface, there was no apparent damage to the glass surface. The Tris surface debris was present on all the microspheres after the pre-rinse and/or attachment testing, with similar amounts present for the 1 and 15 minute incubation periods. Little or no debris was noticed on microspheres after the 0 minute pre-rinse and the elution in de-ionized water. The series of images in Figure 23 show a Tris patch boiling during ESEM inspection. EDS analysis of the debris, shown in Figure 24, detected Cl^- in the dried residue.

Figure 25 is an ESEM photo of the Qiagen® filter showing a spacious mat of fibers with individual fiber diameters of ~2 μm. EDS performed on the fibers indicate that the glass is most likely an aluminoborosilicate, although this is an assumption since boron cannot be detected in the glass due to the limitations of the detector.

The CAFe and SLS microspheres used in the DNA isolation from cells and eluted with the PE buffer are shown in Figure 26. CAFe microspheres that remained in the buffers overnight, shown in Figure 26c, exhibited minor surface roughening.

B. Ultra-Violet Spectroscopy

The DNA solutions exhibit an absorption maximum that varied between 256 and 258 nm. The quantity of theoretically adsorbed DNA was calculated based on the difference between the measured absorbance after rinsing the DNA over the microspheres and the maximum absorbance value of the original DNA solution. The concentration of nucleic acids isolated from the cell was obtained using Beer's Law. Both methods used to determine DNA and nucleic acid concentration are shown in Appendix B. Absorbance curves generated using the cuvette spectrometer are labeled 'cuvette obtained' while curves generated using the drop spectrometer are labeled 'drop obtained'.

Figure 27 shows that the amount of DNA attached to the microspheres increases with increasing pre-rinse times in Tris. The largest and most reproducible adsorbance values were obtained by performing a 15 minute Tris pre-rinse followed by a 15 minute incubation in the DNA solution. All data was obtained from samples that were incubated with the DNA solution for 15 minutes. After a 15 minute pre-rinse, the various compositions had adsorbed similar amounts of DNA with the exception of the CAFe which showed a concentration almost twice as large. Negative concentrations represent UV absorbances that were higher than the absorbance of the initial amount of DNA incubated with the microspheres. Figure 28 shows a decrease in absorbance at ~260 and ~230 nm after successive Tris pre-rinses over the CA microspheres. The solutions containing eluted DNA were too low to be accurately measured, with absorbance values falling close to the standard deviation value of ~ 0.02.

A maximum calcium concentration of ~6.2 mM was produced from the CA frit incubated with Tris for 24 hours. Longer incubation periods did not produce higher calcium concentrations. Figure 29 shows the UV absorbance spectra of DNA after mixing with the CAs, CCl or CN solutions with a Tris-EDTA solution as the background buffer in the UV transparent cuvette. The CCl and CN solutions show little effect on the DNA absorbance at ~260 nm, while the 5 mM CAs solution caused a slight increase. The curves begin to diverge from the DNA absorbance curve at ~240 nm, with the CN absorbance increasing and the CCl and CAs absorbance decreasing. The AN solution mixed with DNA in Figure 30 showed a large decrease in absorbance with increasing

aluminum concentration. It should be noted that while all of the calcium aluminate solutions maintained a pH of ~7.4, the AN solution was drastically more acidic with a pH of ~3.8.

The absorbance of the salt solutions mixed with Tris are shown in Figure 31, with AN and CAs both exhibiting a significant absorbance at ~260 nm. The CAs solutions also show a maxima around this wavelength which does not occur in the other solutions. Tris rinses over the CA microspheres produced similar absorbance spectra to the CAs solution.

A summary of the absorbance characteristics of the various solutions incubated with CA microspheres (i.e. pre-rinse, DNA solution, etc.) is shown in Figure 32. The absorbance at ~260 nm of the DNA solution incubated with the unrinsed microspheres is similar to that of the added absorbances from the pre-rinse and original DNA solution.

The drop spectrometer eliminated inconsistencies due to pipetting since the pre-rinse and DNA attachment solutions could be directly examined without being diluted and transferred to a solution-filled cuvette. The concentration of theoretically adsorbed and eluted DNA is shown in Table X. Similar amounts of DNA should have adsorbed to samples with the same composition and microsphere size, regardless of the buffer used for elution, since each sample was initially treated using the same DNA attachment procedure. However, variations in these values were observed, with most samples exhibiting higher concentrations than the ~1.6×10^{-3} $\mu g/cm^2$ concentration calculated for complete monolayer adsorption of entire DNA strands. This calculation, shown in Appendix B, was based on the size of the DNA strand and ignored any phosphate backbone repulsion between strands.

The amount of theoretically adsorbed DNA was always lower than the amount of eluted DNA, except for the CAFe 43-106 μm samples where the values were the same. The UV absorbance at 230 nm for the adsorbed DNA solutions was significantly higher than the absorbance for the AE eluted solutions, but was usually much lower than the PE eluted solutions. The samples rinsed with the PE, EE or PE/EE buffers showed a greater concentration of eluted DNA than the samples rinsed with the AE buffer. No clear strand sizes could be determined from the gel electrophoresis data since the concentration of adsorbed and/or eluted DNA was very low. The UV absorbance curves looked similar to

those of the nucleic acids isolated from the cells shown in Figure 33. Niether the gel electrophoresis or UV absorbance data were shown below because of the low DNA concentrations and similarity of the UV absorbance curves to the cell data.

When normalized for surface area, the 43-106 μm CAFe and SLS microspheres were able to isolate the largest amount of DNA from the cells as shown in Table XI. The samples eluted with the PE and PE/EE buffers once again showed a much higher DNA concentration than the samples eluted with the AE buffer. Although the UV curves are normalized to the buffer solution being examined, samples rinsed with the PE buffer still show significantly higher salt concentrations (i.e. absorbance at ~230 nm) than the other buffers. The 43-106 μm CAFe microspheres eluted with the AE and EE buffers had similar absorbance values.

Gel electrophoresis performed on these samples showed that larger DNA strands (~12,000 bp) were eluted using the AE and EE buffers while only small fragments were recovered using the PE buffer. The gel, shown in Figure 34, also shows that the AE buffer rinsed over the 43-106 μm CAFe and SLS microspheres isolated a greater quantity of smaller strands (~1000 bp) than the <43 μm CAFe microspheres. The presence of only small strands of DNA ($\leq$100 bp) from the samples eluted with the PE buffer was unexpected since the UV absorbance values showed significantly higher DNA concentrations.

C. Inductively Coupled Plasma-Optical Emission Spectroscopy

Figure 35 shows the concentration (mM) of Ca(II) leached from the microspheres after various incubation times in Tris. ICP-OES results from incubating in the DNA solution produced similar results. Only Ca(II) was found to leach from the microspheres in measurable amounts. The CA microspheres showed the highest amount of leached Ca(II) while the CAFe and SLS showed only a small amount after 24 hours.

D. Circular Dichroism Spectrometry

Figures 36 and 37 shows that CAs and CN solutions show a minor decrease in the $\Delta\varepsilon$ value with concentrations at ~5 mM. The CCl spectra behaved in the same manner as the CN and was therefore not shown here. No difference in spectra was noticed between the

10 mM CN solution and the highest concentration of 25 mM. The AN solution showed a steady decrease of Δε above Al(III) concentrations of 2.5 mM, as shown in Figure 38.

E. Thermal Gravimetric Analysis

Mass loss shown in Table XII indicated that similar amounts of Tris concentrated on both the SLS and CA microspheres, with little difference between a 1 and 15 minute incubation period. Most of the Tris appeared to be removed from the CA microspheres after a 1 minute rinse in de-ionized water since the mass loss was similar to that of the untreated microspheres. The CA samples showed a large increase in weight loss after the same period in de-ionzied water and an increased variability in the measured values. The SLS 15-15 di and SLS 15 di show similar mass loss that is slightly larger than that of the untreated SLS microspheres.

Table IX. Average Microsphere Properties.

Sample	Microsphere Diameter (cm)	Density (g/cm^3)	Sample Mass (g)	SA (cm^2)
CA, CASi, CAFe 106-150 μm	0.0123 ± 0.0011	2.8 ± 0.1	0.1 ± 0.0003	5.2 ± 0.1
SLS 106-150 μm	0.0124 ± 0.0011	2.5 ± 0.1	0.1 ± 0.0002	5.8 ± 0.1
Qiagen filter	N/A	N/A	0.0133 ± 0.0002	280 ± 31
CAFe <43 μm	0.0028 ± 0.0014	2.8 ± 0.1	0.02 ± 0.0002	2.6 + 0.3
CAFe 43-106 μm	0.0065 ± 0.0044	2.8 ± 0.1	0.02 ± 0.0002	1.1 ± 0.9
SLS 43-106 μm	0.0065 ± 0.0044	2.5 ± 0.1	0.02 ± 0.0003	1.2 ± 0.9

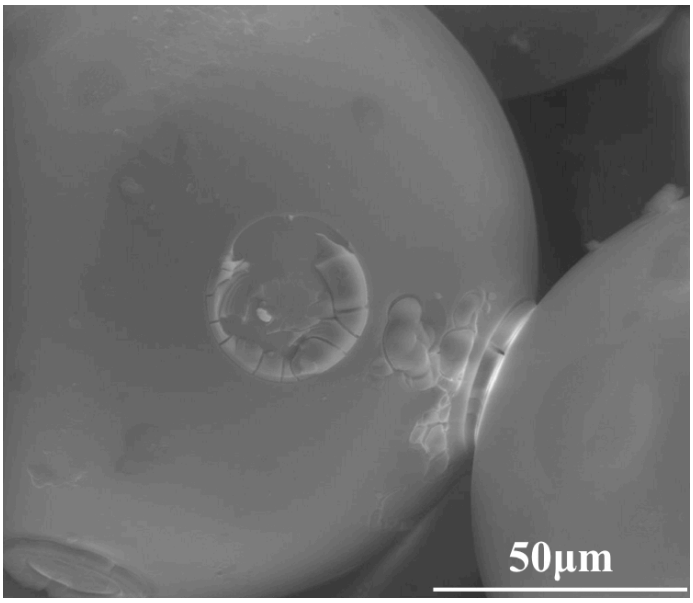

Figure 22. ESEM image of the CA microsphere surface after a 15 minute incubation in a 1 M (12 wt%) Tris solution.

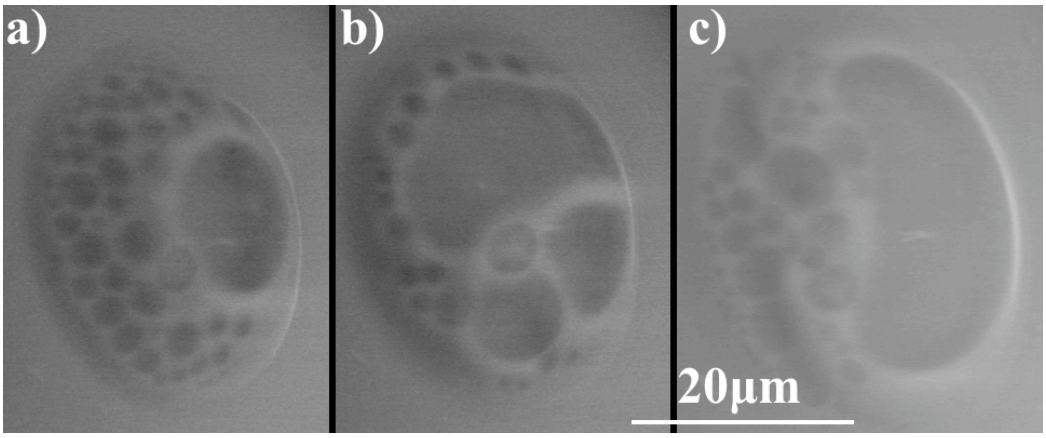

Figure 23. A series of ESEM images showing Tris boiling on the CA microsphere surface during a close examination with the electron beam.

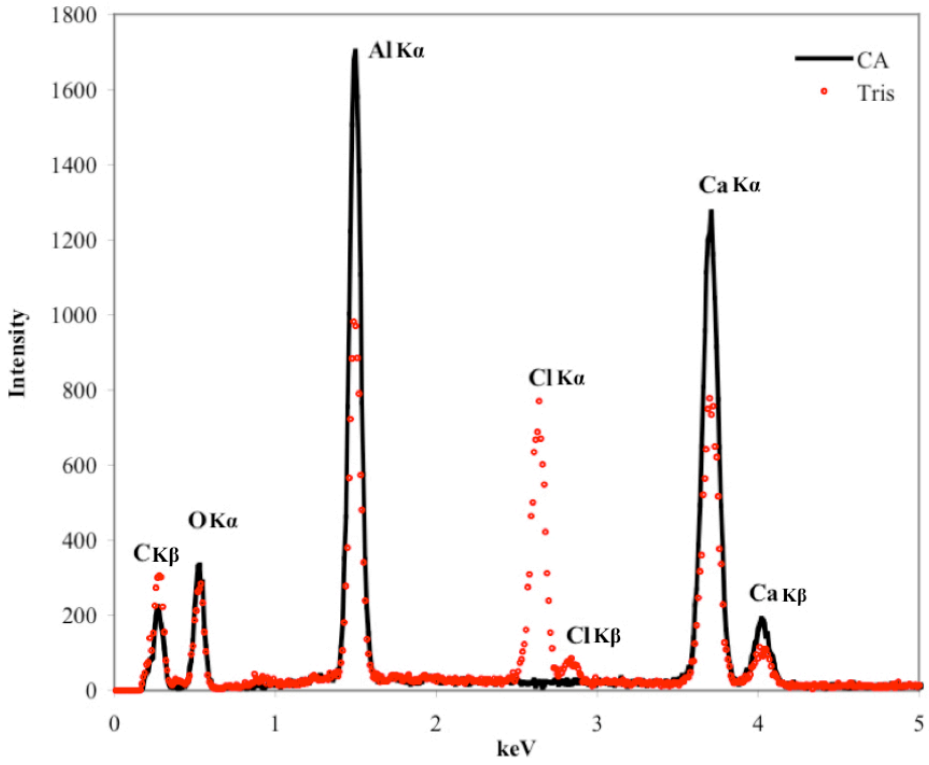

Figure 24. EDS spectra of a CA microsphere surface and Tris debris.

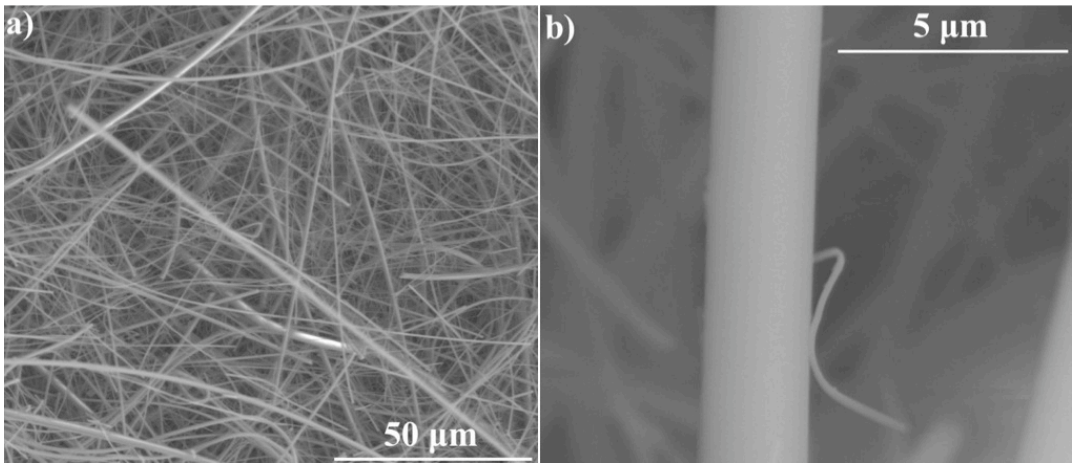

Figure 25. ESEM images of fibers from a Qiagen® filter mat.

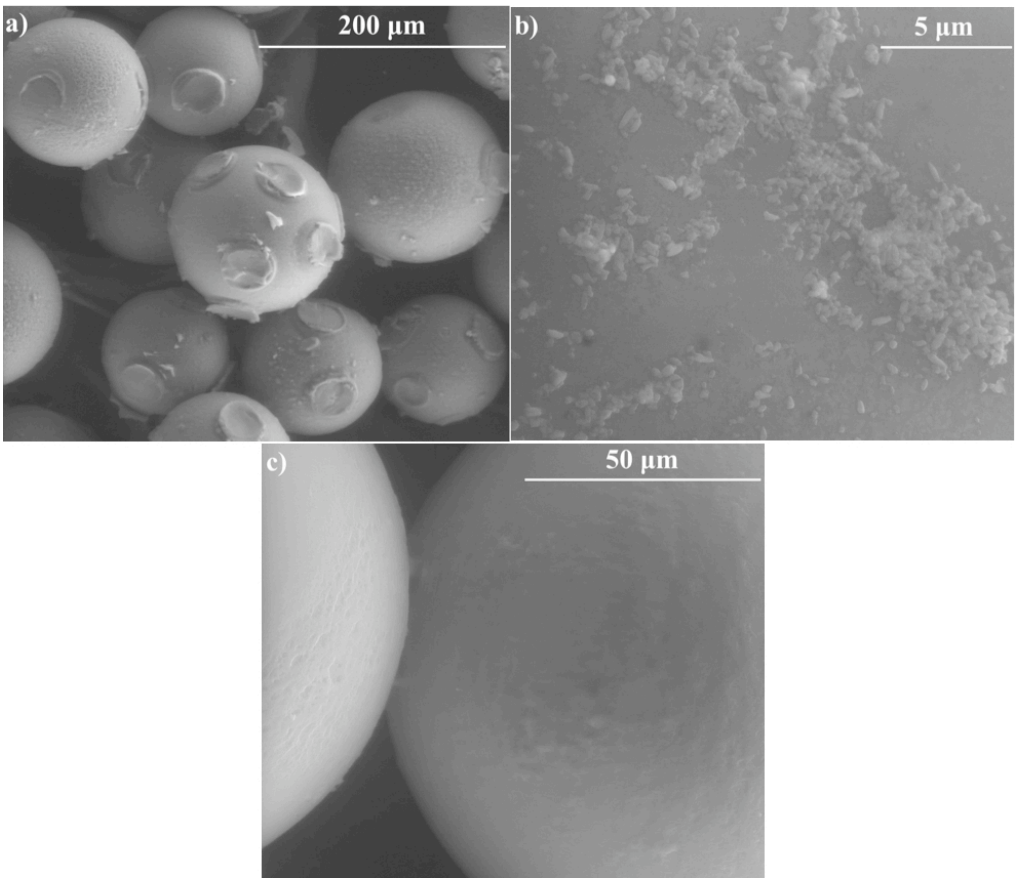

Figure 26. ESEM images of the dried a) CAFe and b) SLS microspheres after nucleic acid isolation and elution with a PE buffer. Image c) shows a CAFe microsphere that had been left in the PE/EE buffer for 24 hours due to incomplete centrifuging.

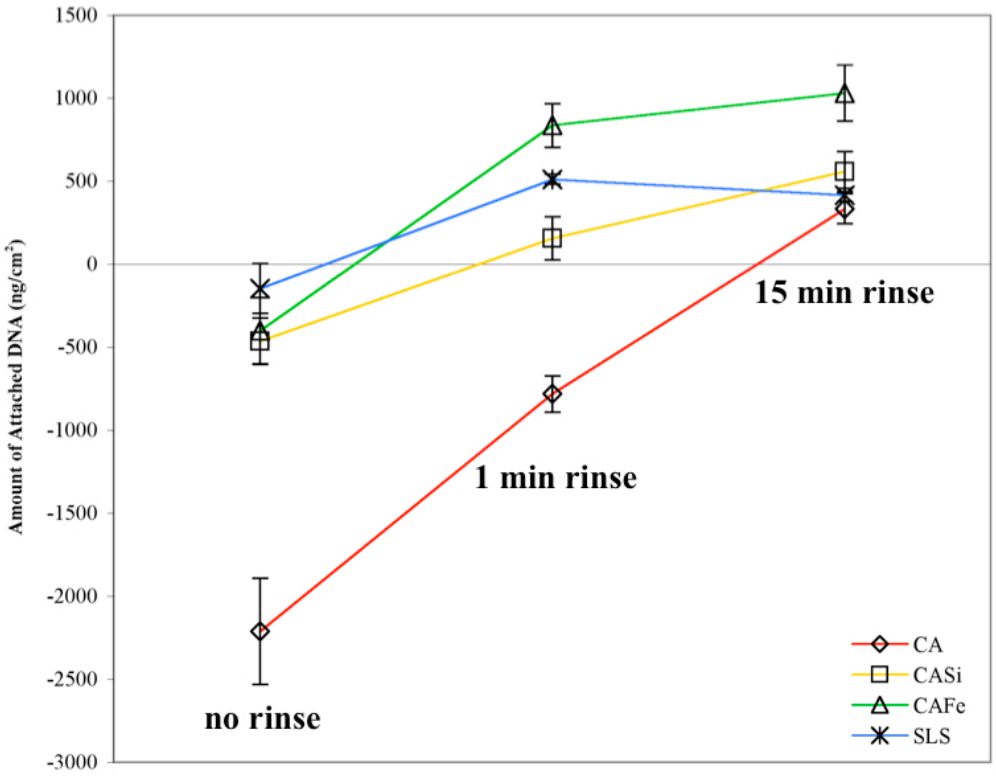

Figure 27. Concentration of DNA adsorbed onto the CA, CASi, CAFe, and SLS microspheres after 15 minutes of mixing with 1 mg/ml DNA susupended in a 1 M Tris solution. The 1 min and 15 min rinse labels indicate a 1 or 15 minute pre-rinse in the Tris before a 15 minute incubation in the DNA solution.

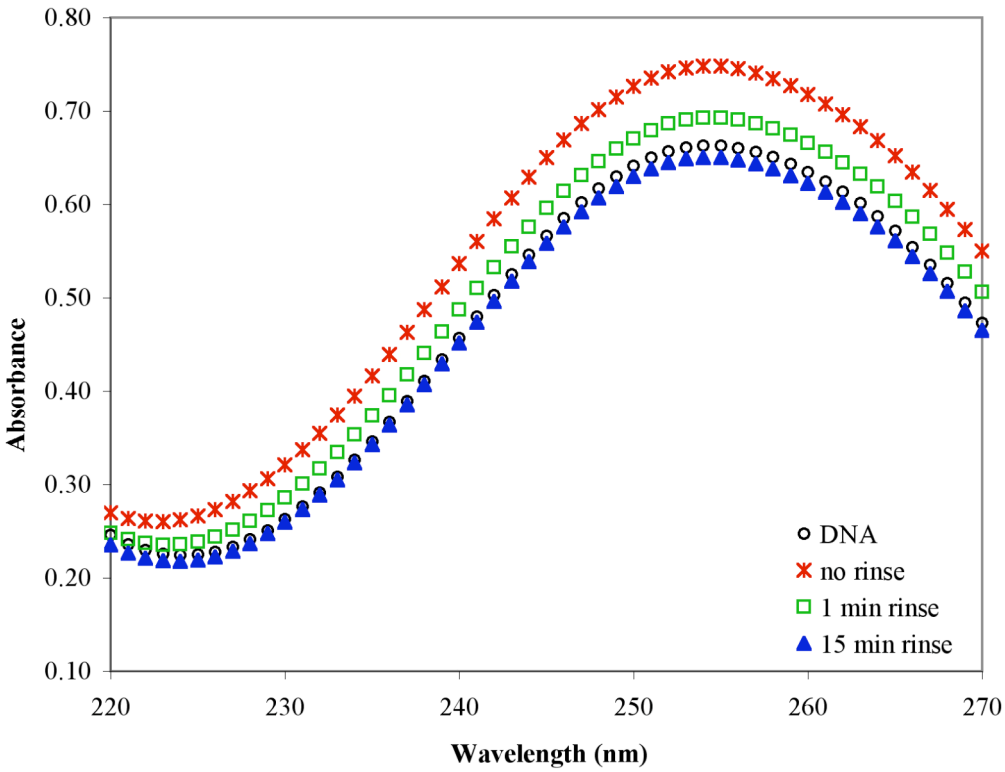

Figure 28. Cuvette obatined UV absorbance spectra of DNA after incubation with unrinsed, and 1 and 15 minute pre-rinsed CA microspheres. Error is within the symbol markers on the curves.

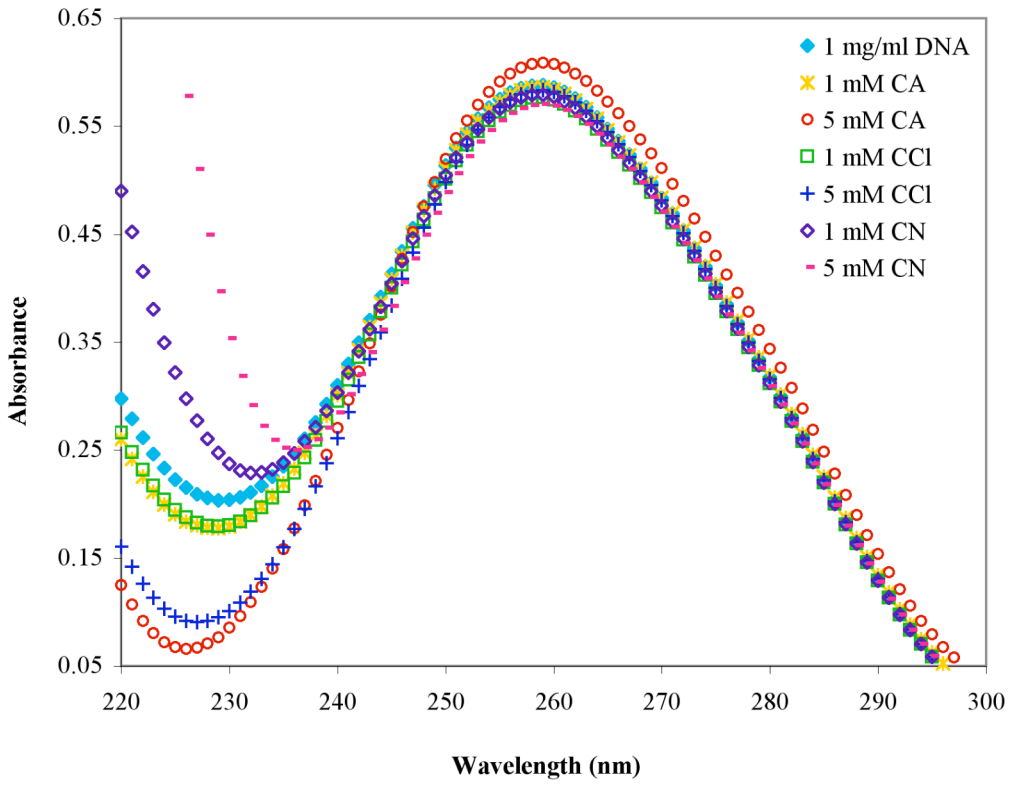

Figure 29. Cuvette obtained UV absorbance spectra of the DNA solution mixed with the CAs, calcium chloride (CCl) and calcium nitrate (CN) solutions. Error is within the symbol markers on the curves.

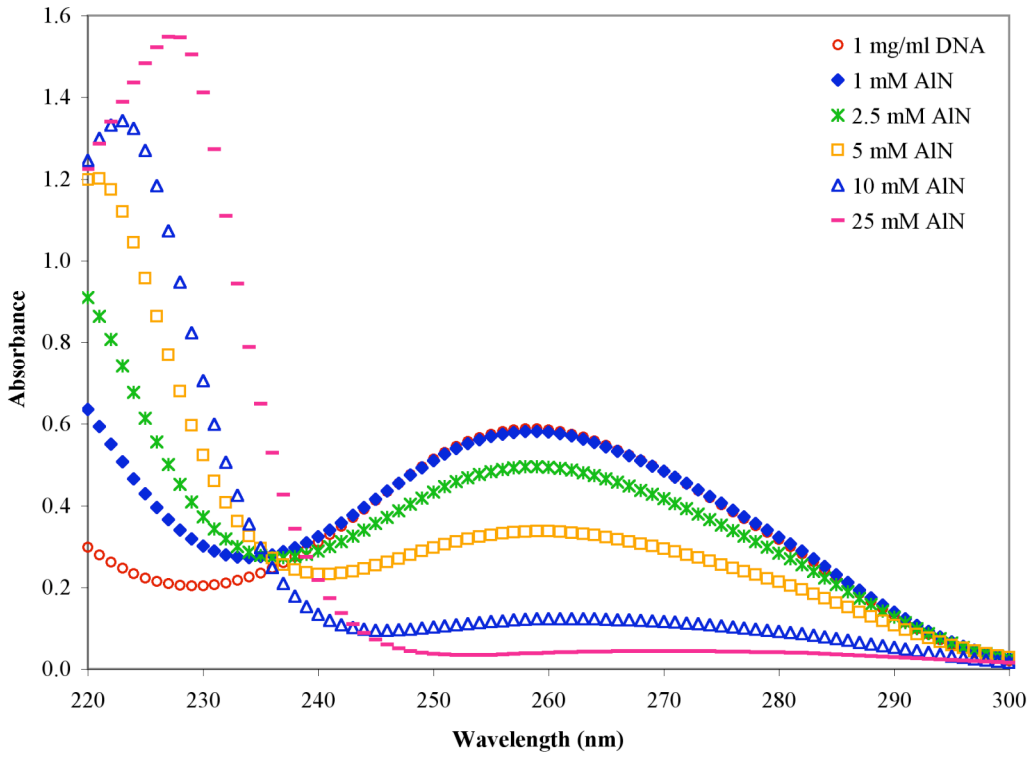

Figure 30. Cuvette obtained UV absorbance spectra of the DNA solution mixed with the aluminum nitrate (AN) solutions. Error is within the symbol markers on the curves.

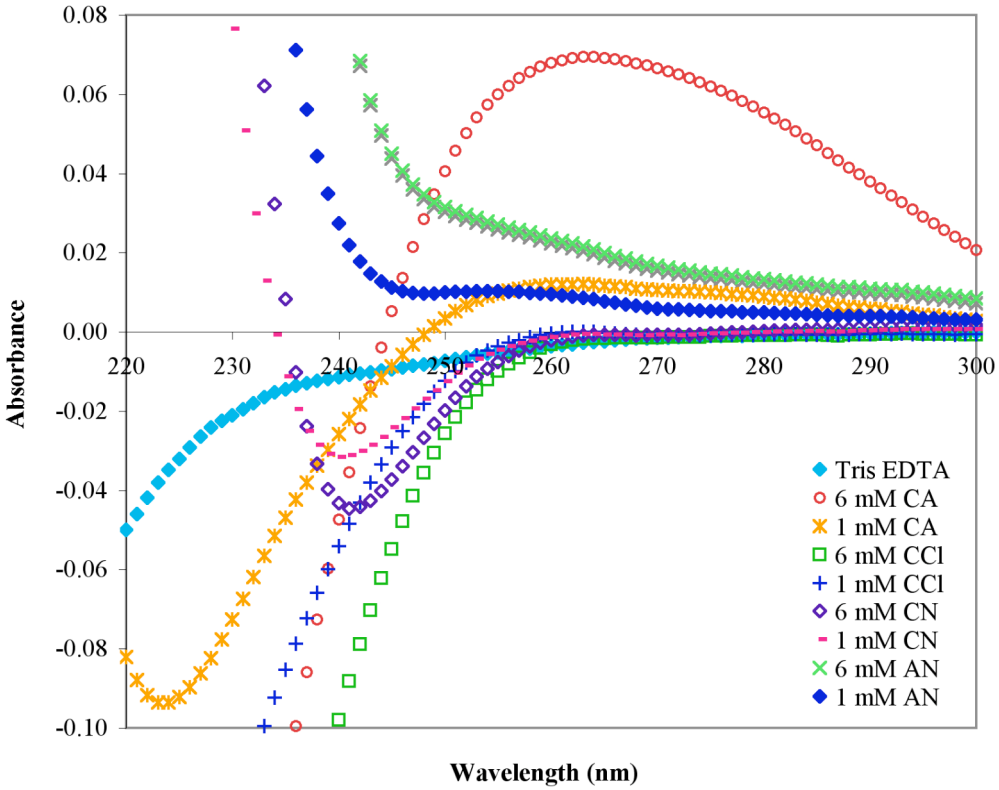

Figure 31. UV absorbance spectra of the Tris mixed with the CAs, calcium chloride (CCl), calcium nitrate (CN), and aluminum nitrate (AN) solutions. Error is within the symbol markers on the curves.

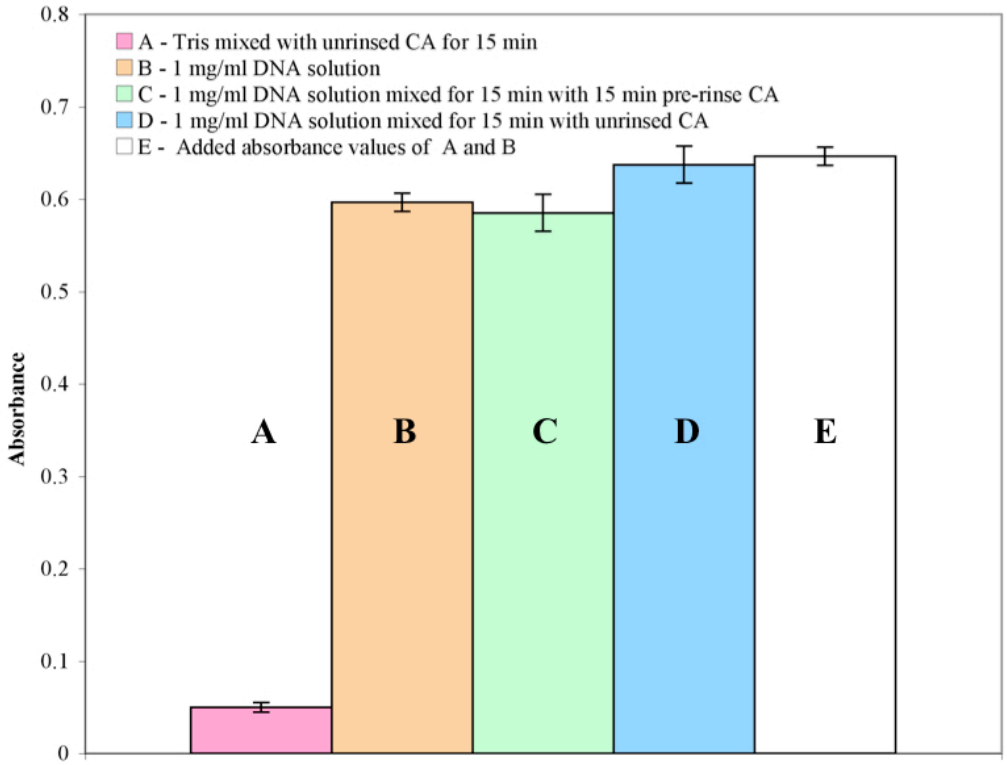

Figure 32. UV absorbance at ~260 nm of the A) ions leached from the CA after mixing for 15 minutes in Tris, B) 1 mg/ml DNA solution, C) 1 mg/ml DNA solution mixed for 15 minutes with the 15 minute pre-rinsed CA microspheres D) 1 mg/ml DNA solution mixed with unrinsed CA microspheres for 15 minutes and E) added absorbance values of A and B.

Table X. Concentration of Adsorbed and Eluted DNA After Sample Incubation in the 0.1 mg/ml DNA Solution. Error on All Absorbance Values was ± 0.004.

Sample/Solution		UV absorbance at 230 nm	UV absorbance at 260 nm	Concentration of Adsorbed/Eluted DNA ($x10^{-3}$ μg/cm^2)
0.1 mg/ml DNA		0.070	0.152	N/A
Qiagen filter	Adsorbed	0.056	0.114	0.09 ± 0.01
	AE Elute	-0.012	0.150	0.35 ± 0.14
CAFe <43 μm microspheres	Adsorbed	0.096	0.133	4.8 ± 2.3
	AE Elute	0.026	0.041	10.4 ± 2.3
CAFe 43-106 μm microspheres	Adsorbed	0.086	0.137	9.0 ± 2.1
	AE Elute	0.015	0.015	9.0 ± 2.2
SLS 43-106 μm microspheres	Adsorbed	0.079	0.155	-1.6 ± 2.8
	AE Elute	0.010	0.012	6.6 ± 1.5
Qiagen filter	Adsorbed	0.025	0.039	0.27 ± 0.14
	PE Elute	0.008	0.007	0.02 ± 0.01
CAFe <43 μm microspheres	Adsorbed	0.103	0.148	1.0 ± 2.2
	PE Elute	0.168	0.144	36.4 ± 3.2
CAFe 43-106 μm microspheres	Adsorbed	0.074	0.145	4.2 ± 2.1
	PE Elute	0.119	0.083	49.6 ± 2.8
SLS 43-106 μm microspheres	Adsorbed	0.080	0.096	30.7 ± 2.1
	PE Elute	0.072	0.072	39.5 ± 2.7
CAFe 43-106 μm microspheres	Adsorbed	0.100	0.145	4.2 ± 2.3
	EE Elute	0.027	0.064	38.3 ± 2.4
CAFe 43-106 μm microspheres	Adsorbed	0.099	0.139	7.8 ± 2.1
	PE/EE Elute	0.069	0.197	117.8 ± 3.1

Adsorbed - Amount of theoretically adsorbed DNA calculated from the UV absorption value of the DNA that did not adsorb to the sample

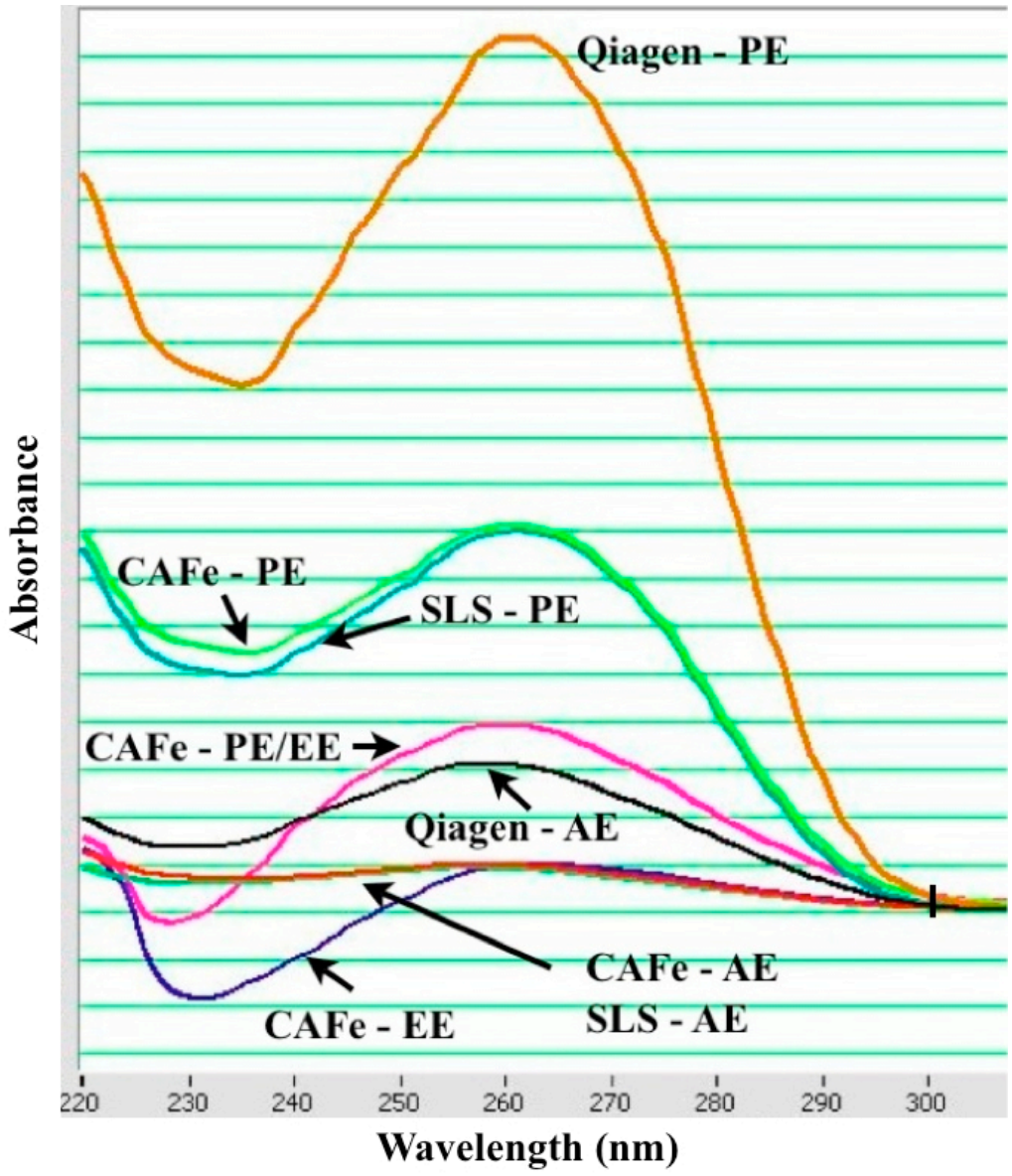

Figure 33. Drop obtained UV absorbance curves for the nucleic acids isolated from the cells. The black band located at ~300 nm represents the error for all of the curves.

Table XI. Concentration of Nucleic Acids Isolated from the Cells. Error on All Absorbance Values was ± 0.004.

Sample/Solution		UV absorbance at 230 nm	UV absorbance at 260 nm	Concetration of Nucleic Acid in Solution (μg)	Concentration of Isolated Nucleic Acid (μg/cm^2)
Qiagen	AE Elute	0.68	1.54	15.42 ± 1.41	0.06 ± 0.01
CAFe <43	AE Elute	0.21	0.11	2.08 ± 1.52	0.80 ± 0.58
CAFe 43-106	AE Elute	0.36	0.49	4.90 ± 1.67	4.46 ± 1.52
SLS 43-106	AE Elute	0.30	0.45	4.52 ± 1.23	3.77 ± 1.03
Qiagen	PE Elute	5.73	9.20	92.02 ± 1.22	0.33 ± 0.05
CAFe <43	PE Elute	2.82	4.05	40.54 ± 2.10	15.59 ± 0.81
SLS 43-106	PE Elute	2.35	4.00	39.96 ± 2.45	33.30 ± 2.04
CAFe 43-106	EE Elute	-0.90	0.48	4.82 ± 2.33	4.38 ± 2.12
CAFe 43-106	PE/EE Elute	-0.07	1.96	19.62 ± 2.31	17.84 ± 2.10

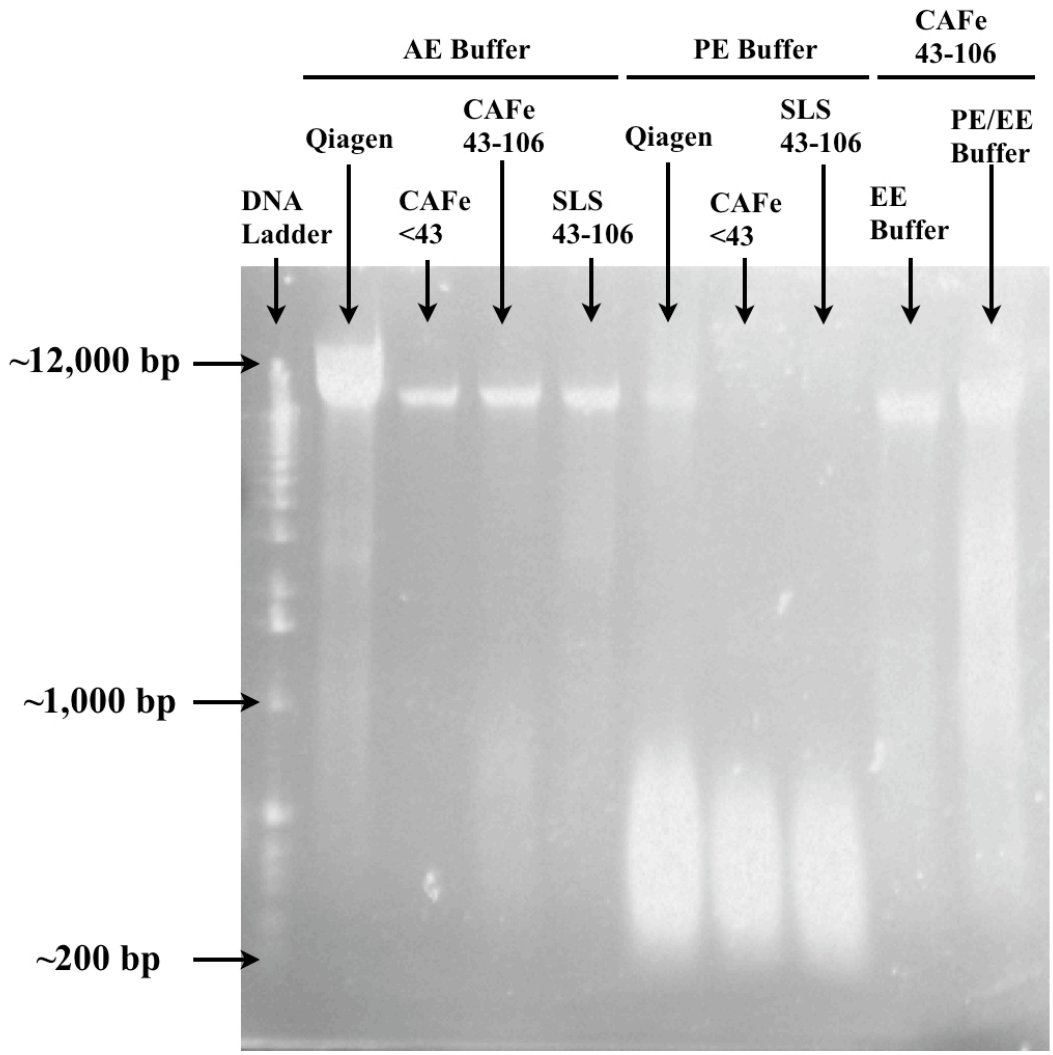

Figure 34. Gel electrophoresis performed on the nucleic acids isolated from the cells.

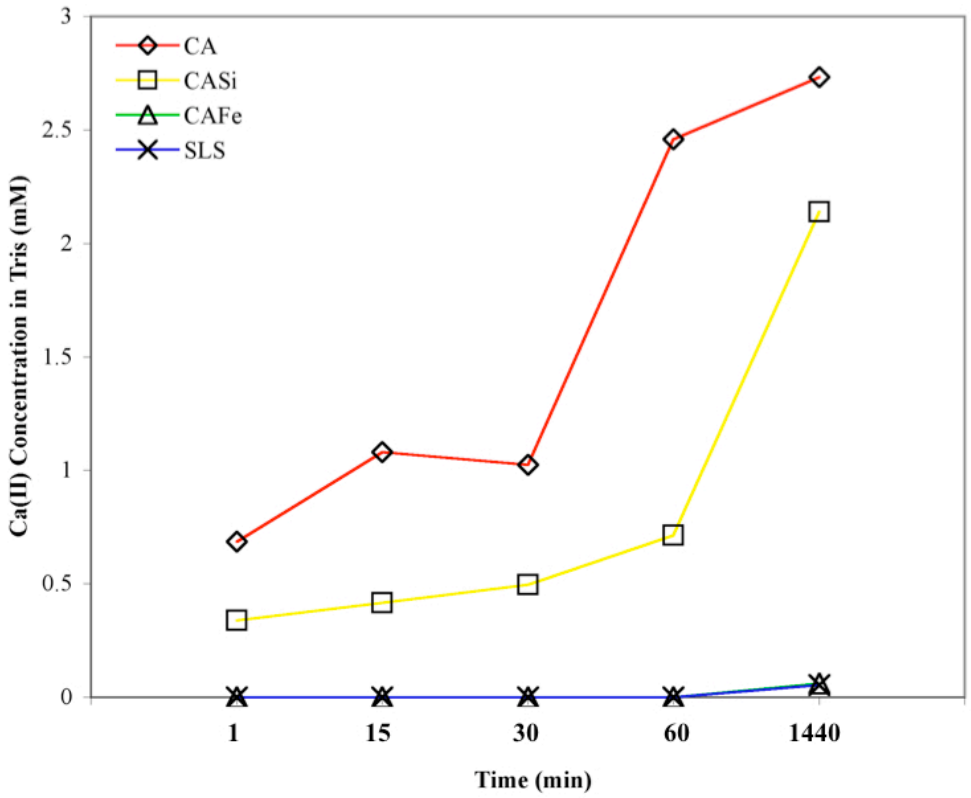

Figure 35. Concentration of Ca(II) ions leached into the Tris from the CA, CASi, CAFe and SLS microspheres after various time periods. Error is within the symbol markers on the curves.

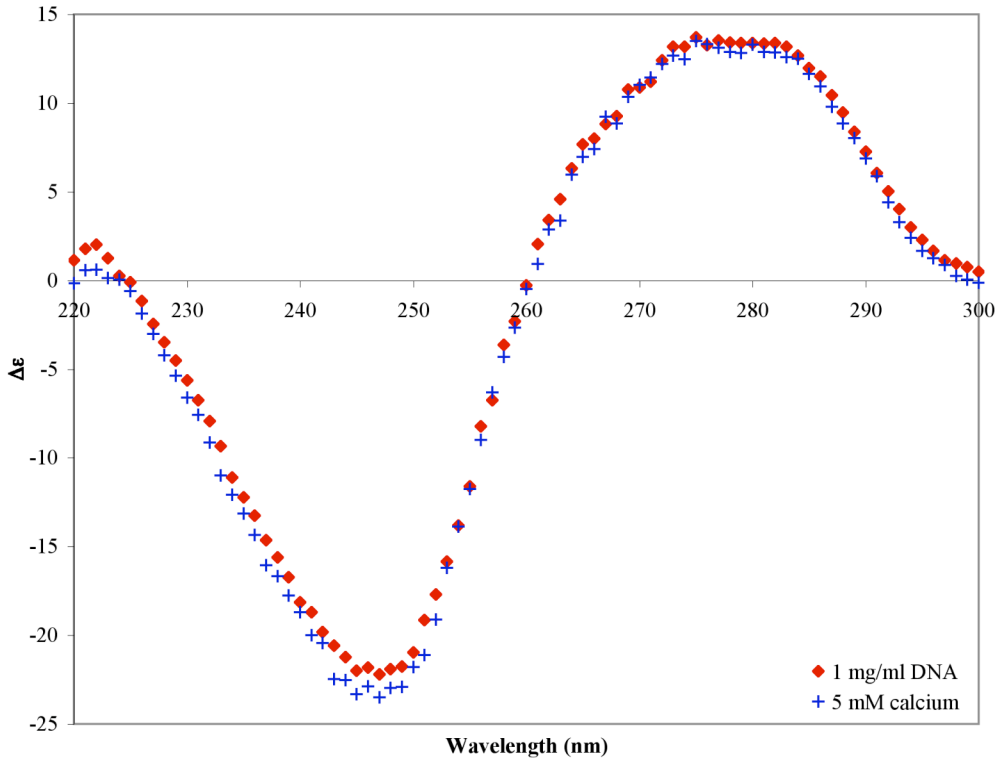

Figure 36. CD spectra of a 1 mg/ml DNA solution mixed with CAs solutions of varying concentrations. Error is within the symbol markers on the curves.

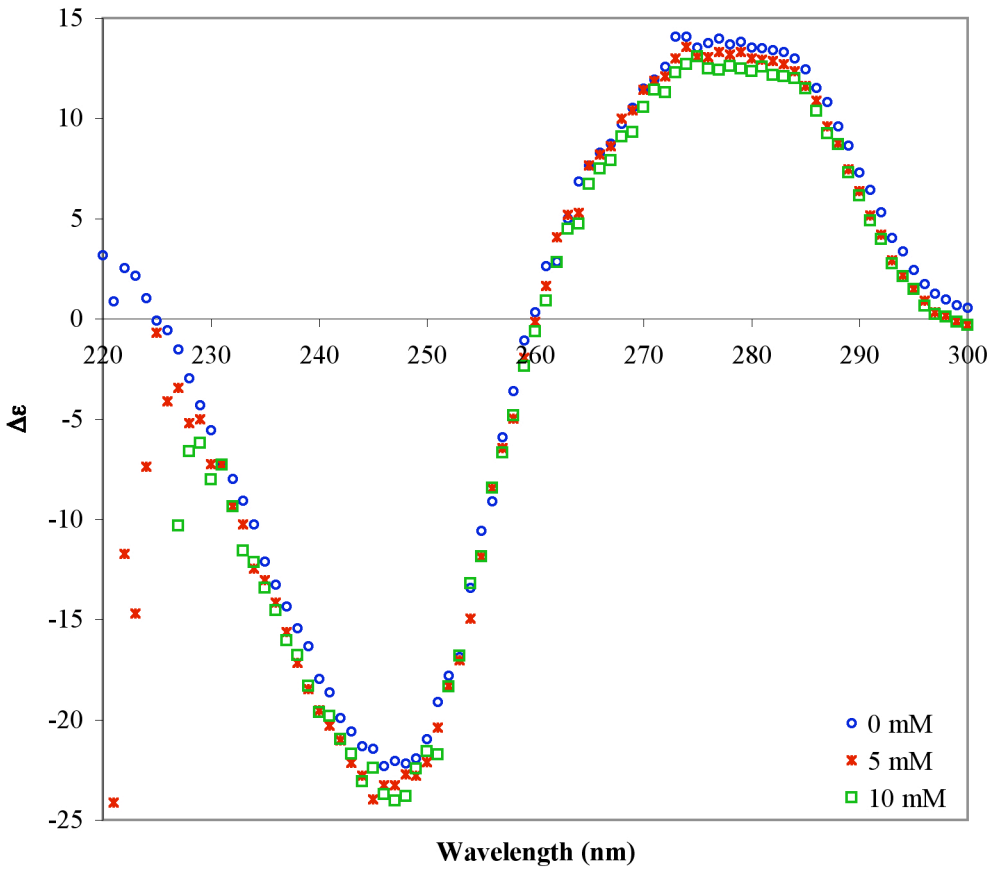

Figure 37. CD spectra of a 1 mg/ml DNA solution mixed with CN solutions of varying concentrations. The 10 mM spectra showed the same magnitude as the 25 mM spectra. Error is within the symbol markers on the curves.

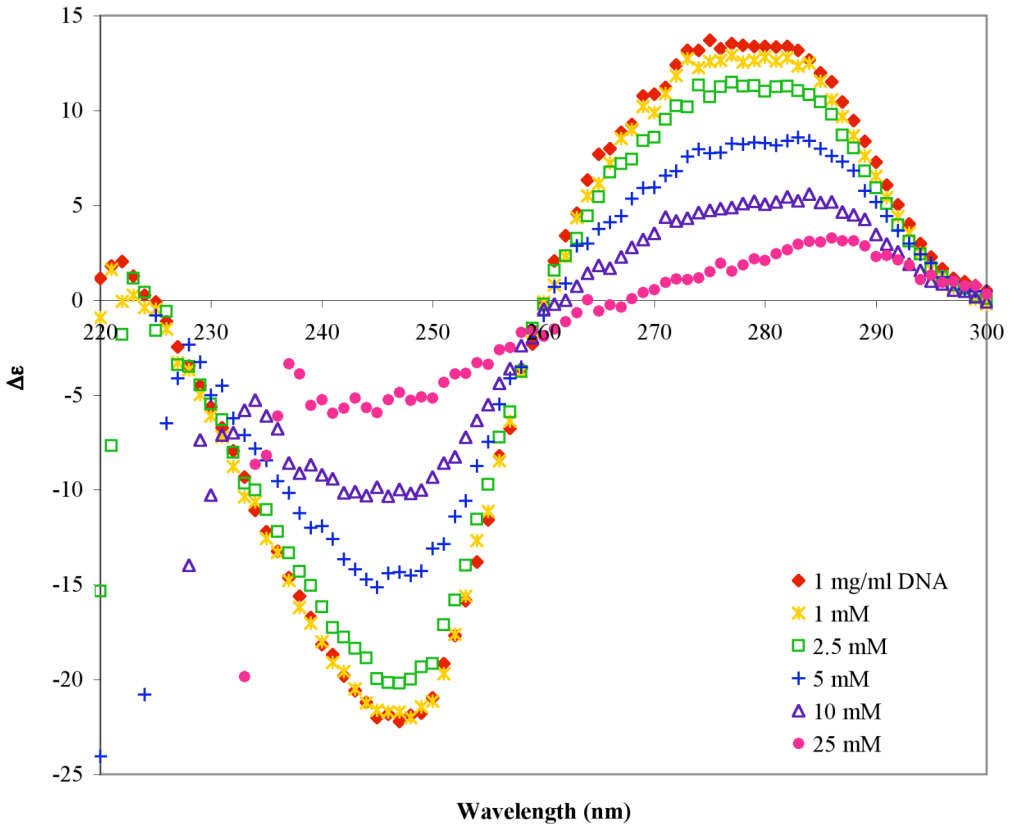

Figure 38. CD spectra of a 1 mg/ml DNA solution mixed with AN solutions of varying concentrations. Error is within the symbol markers on the curves.

Table XII. TGA from CA and SLS Microspheres Incubated with and Tris and De-ionized Water for Various Time Periods.

Sample	% Mass Loss
untreated CA	0.34 ± 0.05
CA 1	0.43 ± 0.02
CA 15	0.43 ± 0.02
CA 15-15	0.34 ± 0.10
CA 15-1 di	0.38 ± 0.10
CA 15-15 di	0.33 ± 0.10
CA 1 di	1.32 ± 0.10
CA 15 di	3.08 ± 0.10
untreated SLS	0.29 ± 0.06
SLS 15	0.45 ± 0.03
SLS 15-15	0.48 ± 0.03
SLS 15-15 di	0.36 ± 0.03
SLS 15 di	0.35 ± 0.03

XVI DISCUSSION

A. DNA Adsorption

An accurate assessment of DNA adsorption onto the microsphere surfaces was hindered by the dissolution of their surfaces. Silicate based glasses used for DNA isolation are pre-rinsed with acidic, aqueous solutions that remove mobile alkali or alkaline earth ions. Pre-rinsing the calcium aluminates with these solutions does not eliminate mobile ions since the leached ions are the result of network dissolution due to aqueous attack. The presence of Tris in solution diminishes aqueous attack through hydrogen bonding to the water molecules and the formation of a protective coating over the surface. A more detailed explanation of these mechanisms is presented in Chapter 3.

A 15 minute Tris pre-rinse enabled accurate absorption readings, although specific interactions between the Tris, DNA, and microsphere surfaces are unclear. A theoretical maximum adsorption limit of ~1.6 ng/cm^2 was calculated assuming monolayer attachment of the entire DNA phosphate backbone and neglecting any repulsion between the strands. The measured absorbance values were over 100x this calculated value, indicating that the Tris was allowing multi-layer adsorption to occur. The Tris concentration is 100x those normally observed in biological solutions, and is therefore expected to behave in a similar manner as the chaotropic agent guanidine hydrochloride. Guanidine hydrochloride is present in Qiagen® isolation solutions and is used to promote DNA adsorption onto the silicate fibers.[48] The guanidinium cation, shown in Figure 39, is protonated at physiological pH (pKa ~12.5) and encourages DNA adsorption to the negatively charged silicate surface through hydrogen bonds formed by its protonated amine groups. The molecule also disrupts water molecules associated with the DNA backbone that can hinder its ability to interact with even a positively charged surface. The Tris molecule stabilizes the helix in the same manner, but its binding abilities are weaker since at physiological pH only about half of the Tris molecules will possess a positive charge on their amine group.[63,64,67] The high DNA adsorption values are likely the result of hydrogen bonded Tris-DNA complexes becoming entrapped in the Tris debris that collects between the microspheres. The positively charged amine group

would be expected to interact more strongly with the negatively charged SLS surface than the positively charged calcium aluminate surfaces. This interaction is unclear from the % mass loss of both the SLS 15-15 di and SLS 15 di samples, which were slightly larger than the untreated SLS microspheres, indicating a small amount of surface hydration. The similarity in mass loss between the CA 15-15 di and the untreated CA suggests that while the hydrogen bonding between the CA and the Tris is weak, the interaction between the re-suspended Tris and water molecules is strong enough to inhibit aqueous attack of the CA surface.

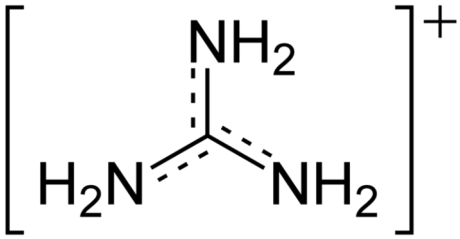

Figure 39. Guanidinium cation.[48]

The negatively charged phosphate backbone of the DNA showed a greater affinity for the CAFe microspheres in the absence of chaotropic agents. Variations in the concentration of adsorbed DNA between samples of the same composition and morphology arise due to the way in which the DNA adsorbs onto the sample surface. Complete adsorption of the entire DNA backbone is improbable; instead the backbone is likely to adsorb at one or several locations down the strand, leaving the unattached segments free in solution. Partial adsorption can either encourage or hinder further DNA attachment depending on its repulsive interaction volume in solution. A mostly stationary strand would have a lower interaction volume in solution and therefore have a greater possibility to adsorb more DNA in the surrounding region. Another possible reason for variation in the adsorbed concentration is that the DNA is not chemically bound to the surface. If a large strand is only able to attach one small segment, there is a

high possibility of desorption due to physical forces during incubation and/or centrifuging.

The difference in concentration of adsorbed and eluted DNA could be the result of a higher concentration of ions leached from the sample or buffer salts in solution. The concentration of DNA adsorbed to the samples was calculated using the difference between the measured UV absorbance at 260 nm and the absorbance of the original 0.1 mg/ml DNA solution. Therefore, a higher measured absorbance due to leached ion contamination would make it appear that less DNA had actually adsorbed to the sample. A higher measured absorbance at 260 nm for the elution buffers would falsely indicate that a larger amount of DNA had been eluted from the sample, since the measured absorbance value is directly used in the DNA concentration calculation. The calculated DNA concentrations are sensitive to small changes in UV absorbance, with changes of ~0.004 corresponding to a change DNA concentration of ~$2x10^{-3}$, ~$1x10^{-3}$ and $0.1x10^{-3}$ $\mu g/cm^2$ for the 43-106 μm and ≤ 43 μm microspheres, and the Qiagen® filter, respectively. The DNA concentrations calculated from the AE and EE elution buffers are thought to be more accurate since the absorbance at 230 nm is low and the original DNA absorbance is not necessary to calculate the concentration. The PE and PE/EE elution buffers show the highest concentration of eluted DNA but their significantly higher UV absorbance values and the shape of their curves suggested erroneous results.

The addition of chaotropic agents to the cell debris effectively shielded the negative charge on 43-106 μm SLS microsphere surfaces since the quantities of isolated nucleic acid were similar to those isolated by the 43-106 μm CAFe microspheres. While the larger microspheres appear to be more effective at isolating nucleic acid from the cells than the Qiagen® filter, testing needs to be performed using similar surface areas before a direct comparison can occur. A smaller microsphere sample size had to be used during these experiments because incomplete centrifuging of the surfactant-containing lysis solution and cell debris occurred with larger sample sizes. Larger sample sizes are currently being investigated using a stabilized bed of microspheres so that the porosity cannot shift and decrease during centrifuging.

Establishing how nucleic acids tend to adsorb onto the sample surface or become physically entrapped in the microsphere bed is important in determining why the larger

microsphere sizes isolated a greater quantity of nucleic acids than the smaller microspheres or the Qiagen® filter. Similar amounts of nucleic acids were expected to have adsorbed onto the different sized CAFe microspheres due to their similar surface areas, while the Qiagen® filter was expected to adsorb a much greater quantity than the SLS microspheres since its surface area was over 20x larger. The similarity in concentration of isolated nucleic acids using the CAFe and SLS microspheres suggests that under the influence of a chaotropic agent, the major factor in nucleic acid isolation ability is substrate morphology and size. The Qiagen® filter contains a mat composed of ~2 μm silicate fibers which are much thinner than the genomic nucleic acid strands which can range from a couple microns to centimeters in length. The high curvature of the fibers are unable to isolate strands longer than $\geq$ 50,000 bp due to the shearing force generated during centrifuging. The use of microspheres was anticipated to increase adsorption ability via the reduction of strand repulsion through lower surface curvature and by their ability to physically entrap the larger strands in the tightly packed microsphere mat. The microsphere samples did not appear to adsorb larger strands than the Qiagen® filter. This result may be due to the physical entrapment of larger strands within the packed bed of microspheres, as well as a greater affinity for the microsphere surface. The highly concentrated PE buffer was originally used to enhance the removal of these larger strands since it is known elute nucleic acids from other positively charged surfaces, such as hydroxyapatite.[39,46,73] Once again, the concentration of nucleic acids isolated using the AE and EE buffers are considered to be more accurate than the PE and PE/EE buffers for the same reasons discussed above, but also from the results of the gel electrophoresis data discussed below.

While the PE and PE/EE buffers appear to have eluted the most nucleic acids from the samples, gel electrophoresis shows that denaturing and/or fragmentation of DNA is occurring. The presence of high molecular weight strands in the Qiagen-PE is only the result of the much higher quantity of nucleic acids originally isolated from the cells. Nucleotides are only cleaved mid-strand via endonucleases, which were not present in the solutions during nucleic acid isolation. Therefore, the source of fragmentation may have come from the high concentration of the Na_2HPO_4 buffer. Under extremely high salt concentrations, the DNA double helix will denature due to the

repulsive forces between the salts originally present around the backbone to electrostatically shield the negatively charged phosphate groups. RNA and denatured DNA strands will be observed at the same location as the double stranded DNA on the electrophoresis gel but will fluoresce with lower intensity. Although low molecular weight strands travel farther through the gel, the single stranded entities travel the same distance as their heavier double stranded counterparts due to their lower number of negatively charged phosphate groups and the complex conformations they form to increase their stability. The instability of the single strands could have allowed their end groups to be sheared off by the dissociated Na_2HPO_4 groups. Repeated shearing of the end groups would eventually cause the low molecular weight strands that appear in the gel in Figure 34. Currently, the effects of various Na_2HPO_4 concentrations on double stranded DNA are being examined using CD spectroscopy and gel electrophoresis.

The accuracy of some of the UV absorbance values are questionable since several variables can invalidate Beer's Law. Beer's Law assumes that there is a linear correlation between a solution's measured absorbance and the concentration of absorbing species in solution. However, this assumption is only true for dilute solutions (< 10 mM) where the distance between absorbing species is large enough not to effect the charge distribution of its neighbors. When either absorbing or non-absorbing species in a solution becomes too high, the absorbance-concentration correlation factor becomes non-linear. The concentration of both the nucleic acids and the PE, EE and PE/EE buffer solutions were large enough to produce non-linear correlation factors and therefore artificially high UV absorbance values. Fortunately, UV spectrometry is rarely used to quantify the concentration of nucleic acids in solution. Components present in the buffer solutions that could inhibit accurate absorbance measurements are irrelevant if there are no interferences with downstream applications of nucleic acids, such as the replication of DNA through PCR. The CD spectra showed no significant changes in $\Delta\varepsilon$ of DNA after incubation with the calcium aluminate based microspheres. This indicated that no severe conformational changes occurred due to reactions with the microsphere dissolution products.

B. DNA Interactions with Hydrated Cations

Aluminum nitrate is excluded from the discussion on interactions with DNA due to the formation of precipitation upon mixing with the DNA solution. The pH increase of the acidic aluminum nitrate solution upon mixing with the buffer causes an insoluble aluminum hydroxide to form. DNA can be become entrapped during the precipitation process. As a result, the large decrease in UV and CD values are due to precipitation and not conformational changes in the DNA molecule.

The difference in UV absorbance between the dissolved calcium salt solutions and the solution containing calcium leached from the microspheres is not fully understood. Divergence of the salt solutions spectra obtained on the Perkin Elmer at ~230 nm is the result of the different anions associated with the calcium salts. Low energy electronic transitions are more probable for the nitrates, which still contain a nitrogen-oxygen bond after dissociation.[8,74] The absence of the chemical bond in both the calcium chloride and CAs solution supports this theory. However, the absorption appears to be environment specific since all of the salt solutions show an increase in absorbance at ~230 nm during examination with the drop spectrometer. Any or all of the changed parameters (undiluted solution, lower Tris concentration, absence of EDTA) could have affected this low wavelength absorbance.

Previous studies on the interactions between cations and the Tris molecule were investigated using the associated chloride or nitrate salt.[63,64,67] The calcium binding constants calculated under these conditions assume that both free and solvated cations are available to form a coordinate bond with the lone pair of electrons on the primary amine of the Tris molecule. The model for these calculations not only uses the erroneous idea that free cations exist in solution but also neglects any possible anion interactions.[8] Electron competition between the calcium and the protons in solution could be affected by the small amount of association between the solvated ions. The formation of calcium-Tris complexes and/or the occurrence of any non-bonding interactions could be examined in more detail using FTIR spectroscopy. If variations in the Tris and calcium concentrations produced spectral changes, the strength of these interactions could be examined using isothermal titration calorimetry.

XVII CONCLUSION

DNA exhibited a greater affinity for the positively charged CAFe microsphere surfaces than for the negatively charged surfaces of the SLS microspheres and the Qiagen® filter in the absence of chaotropic agents. Physical entrapment of the DNA between the tightly packed microsspheres is thought to have produced the greater adsorption to the SLS microspheres over the Qiagen® filter.

The addition of chaotropic agents to the solution increased the ability of both the SLS microspheres and the Qiagen® filter to isolate DNA from the cells. However, the lower quantity of nucleic acid isolated by the <43 μm CAFe microspheres compared to the SLS microspheres indicates that microsphere size plays a significant role in nucleic acid adsorption capacity.

Gel electrophoresis did not indicate that the microspheres isolated higher molecular weight strands than the Qiagen® filter, although this could be due to an inability to elute physically trapped high molecular weight strands. Adsorption experiments using high molecular weight DNA with a known size and various elution buffers could be used to validate this prediction. If the microspheres are able to isolate larger DNA strands than the Qiagen® filter, they could potentially be used in laboratory scale filters as opposed to the more complicated processes normally performed to isolate strands >50,000 bp.

UV spectroscopy provided inaccurate nucleic acid concentrations if the solution being examined contained a high concentration of UV absorbing and/or non-absorbing species. At high concentrations, the Beer's Law coefficient relating UV absorbance to the absorbing species concentration becomes non-linear and therefore invalidates the equation. While microsphere dissolution could have contributed to inaccurate UV absorption measurements, the dissolution products are not thought to interact with the nucleic acids in a manner that could inhibit their use in downstream applications.

CHAPTER 3: INTERACTIONS OF GLASS SURFACES WITH DEIONIZED WATER AND TRIS(HYDROXYMETHYL)AMINOMETHANE

XVIII LITERATURE REVIEW

A. Hydration of Calcium Aluminates

1. Crystalline Calcium Aluminates

The hydration of crystalline calcium aluminates has been extensively studied due to interest in the reactions occurring during the formation of hydraulic cements. Hydraulic calcium aluminate-based cements harden and become chemically stable after reactions in water form hydrated crystals that can interlock and eventually bond to one another.[26] Most studies have focused on the hydration of crystalline $3CaO•Al_2O_3$ (C3A), $CaO•Al_2O_3$ (CA), or Mayenite - $12CaO•7Al_2O_3$ (C12A7), which are components in high alumina cements.[27-30,75-77]

The hydration process begins through congruent dissolution of the calcium aluminate matrix. The conductivity and pH of the solution will increase as calcium and aluminum ions leach into the solution.[78] Nucleation occurs once the solution has become supersaturated, eventually driving the formation of the hydrated crystalline phases.[27-30,75,76,79] Similar phases are usually formed, irrespective of the anhydrous composition, and depend on temperature and hydration conditions. Hydration occurring between 5 and 25˚C initially produces an amorphous $Al(OH)_3$ gel layer along with needle and hexagonal plate crystals most commonly characterized as $CaO•Al_2O_3•10H_2O$ (CAH10), $2CaO•Al_2O_3•8H_2O$ (C2AH8), $4CaO•Al_2O_3•19H_2O$ (C4AH19) or $4CaO•Al_2O_3•13H_2O$ (C4AH13), depending on the hydration conditions. Most crystals precipitate from the solution but the amorphous gel layer has been observed to form hexagonal hydrates over time. Regardless of the formation mechanism, the structure consists of alternating layers of hydrated calcium aluminate plates of cationic $Ca_2Al(OH)_6^+$, separated by hydrated anions. The $Ca_2Al(OH)_6^+$ planes have been described as a regular arrangement of

calcium and aluminum in a distorted octahedral coordination or as agglomerates of calcium and $(Al(OH)_6)^{3-}$ ions. The exact structure of the anionic layer is unknown with reported structures ranging from simple OH^- molecules to various hydrated states of aluminate anions, $(Al(OH)_x)^{y-}$. When aluminate anions are present they can form in both octahedral coordination, $(Al(OH)_6)^{3-}$, as well as in $(Al(OH)_4)^-$ distorted tetrahedrons. Any structural voids are occupied with water molecules or dissociated forms thereof. Ultimately, variations in temperature, local water shortages and/or acetone rinses used to halt the hydration process, can dehydrate the water layers to produce even more complex structures. The dehydration of C2AH8 in ambient atmosphere has been reported to produce C2AH7.5, C2AH5, and C2AH4 successively with increasing temperature. Upon dehydration, the basal spacing respectively decrease from 10.6, 8.7 to 7.4 Å. At a temperature of ~600˚C all the water is thought to be removed from the system and with increased heating CaO and C12A7 are formed.

The hexagonal plates initially form a protective coating around the unreacted CA, however these phases are not stable in water and usually decompose with continued hydration and/or temperatures above 30˚C.[27-30,75,76] The dissolution of these phases is accompanied by the formation of a less soluble cubic phase, $3CaO•Al_2O_3•6H_2O$ (C3AH6). However, if CO_3^{2-} is present in solution, this conversion does not occur, regardless of the hydration period. Replacement of the anionic hydroxyl by carbonate is thought to block phase conversion by inhibiting the free movement of the hydroxyl ions within this layer via hydrogen bonding.[29,76]

Considered to be the only stable hydrated phase, C3AH6 is thought to nucleate in solution, with the dissolution of the hexagonal hydrates maintaining the necessary solution composition for crystal growth.[27-30,75,76] The crystal structure of C3AH6 has been well characterized as a hydrogarnet in which the calcium and aluminum are located on special positions with eight and six fold coordination, respectively, and the hydroxyl ions are located at the Ia3d positions of the body centered cube.[30,80] The unit cell contains 8 formula units and can crystallize into a variety of isometric forms including cubes, rhombic dodecahedra and octahedra. This phase remains stable up to ~275˚C where it is converted to an unknown dehydrated species resembling C12A7.[30,79] While a variety of forms have been reported based on the relative humidity during drying, full

decomposition occurs around ~500˚C and leads to the formation of CaO and C12A7. Recombination of the CaO and C12A7 at ~1050˚C leads to the formation of C3A.

Traetteberg observed the hydrated phase conversions macroscopically in cement slurries.[26] The slurries began to thicken soon after hydration due to the formation and interlocking of the hexagonal plates. As the platelets converted to the cubic phase the slurry became more fluid since these rounded crystals do not physically interlock. After extended time periods, the slurry hardened due to the formation of chemical bonds between adjacent crystals.

The surface area/volume of water (SA/V) ratio also influences calcium alumiante hydration.[29,81] The less hydrated C4AH13 phase is thought to form instead of C4AH19 in samples with a high SA/V. Insufficient amounts of water can also inhibit the dissolution and conversion of the hexagonal hydrates to the less soluble C3AH6 phase. However, if the heat generated during hydration cannot be dissipated, such as in a small water pocket, conversion can occur. Localized temperatures above 30˚C have been reported to enable the formation of C3AH6, which continues to form even after the temperature has decreased. [27-30,75,76] Direct formation of C3AH6 from crystalline C3A can occur if the temperature of hydration is above 60˚C.

2. Amorphous Calcium Aluminates

Most studies involving amorphous calcium aluminates have been focused on their optical properties. Their low optical loss and high infrared cut off wavelength (~6 μm) make them ideal materials for low loss fibers and infrared waveguides.[32,82] Unfortunately, only small quantities of glass can be produced without crystallization and most of these must still be quenched. These glasses also exhibit low chemical durability and hydration behavior similar to that observed in the crystalline form. Although these difficulties have limited the study of these glasses as potential optical materials, their hydration properties have been utilized as quick setting agents in cement.[25] Nakagawa et al. examined the difference in the hydration times between amorphous and crystalline C12A7 after the amorphous form was found to solidify at a much faster rate.[25] Initial rapid hydration rates were found to quickly retard, and after 15 minutes the degree of hydration between the amorphous and crystalline samples had reached similar levels. Similar hydration levels were attributed to the formation of the protective C2AH8

hexagonal phase which initially inhibits the dissolution of the material. No explanation was given for the initial higher rate of hydration of the amorphous material.

B. Reactions Between Calcium Aluminates and Polymeric Compounds

The addition of organic compounds to calcium aluminates has been found to retard or completely inhibit the formation of the hydrated precipitates and their phase conversions at elevated temperatures.[76,83] The ability of an organic to inhibit hydration/conversion is largely dependent on the number and position of oxygen functional groups (i.e. hydroxyl, carbonyl, or carboxyl) in the molecule. These groups shield the surface from aqueous attack through hydrogen bonding to water molecules and the oxide surface. For example, aromatic sugar molecules or aliphatic molecules containing a large number of oxy-side groups were found to inhibit the conversion of the hexagonal phase to the cubic phase down to concentrations of ~0.2 wt% and up to temperatures of ~40˚C. The addition of smaller aliphatic molecules, such as propanol, were only able to retard conversion at ambient temperatures, even at concentrations of ~1 wt%. Singh el al. determined that organic adsorption can also occur through strong electrostatic interactions.[84] At neutral pH the acidic hydroxyls of the sucrose carbons were observed to electrostatically bind to the basic -$AlOH2^+$ groups on the alumina surface.

Poly(vinyl alcohol/acetate) (PVA) is one of the most common polymeric additives used to retard hydration and to improve the strength and chemical durability of ceramic composites.[75,85] PVA physically increases flexural strength and toughness by acting as a rheological aid to minimize pore size and also through chemical reactions between the polymer and inorganic ions in solution. During the hydration of a PVA/calcium aluminate cement mixture, the PVA becomes hydrolyzed and forms a cross-linked polymer matrix with the aluminum ion leached from the cement surface. The hydrolysis reaction produces an acetate ion that reacts with leached calcium to form calcium acetate. If enough PVA is present ($\geq$ 5 wt%), hydration of the surface can be prevented (this process is shown in Figure 40). In lower concentrations, the hexagonal hydrates will form but will be intercalated with the cross-linked aluminum product. Conversion to the cubic phase was found to eventually occur around 80˚C.

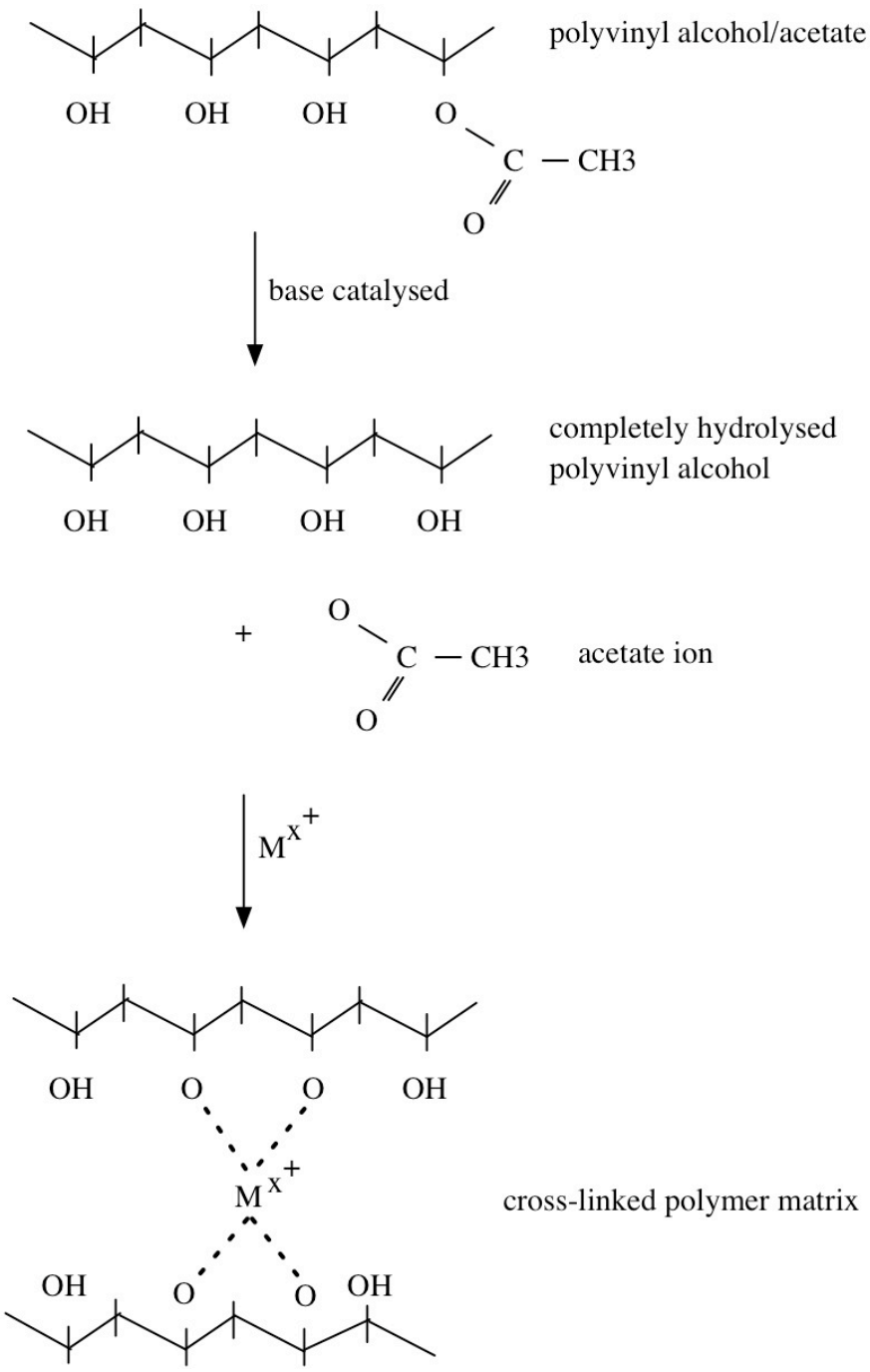

Figure 40. Reaction of polyvinyl alcohol/acetate with a metal ion in solution.

XIX INTRODUCTION

The hydration reactions of crystalline calcium aluminates have been thoroughly investigated due to their use in cementous materials.[27-30,75,76] The hexagonal crystalline precipitates that form during hydration at ambient temperatures are meta-stable with respect to the cubic phase, which forms at temperatures above 30˚C. While amorphous calcium aluminates form the same hydrated phases as the crystalline material, they initially exhibit a much higher rate of hydration.

The studies performed in Chapter 2 involving the attachment of DNA to binary calcium aluminates showed that the buffer solution used for DNA suspension, Tris(hydroxymethyl)aminomethane (Tris), inhibited the formation of the hydrated crystalline phases. Organic compounds have been observed to both inhibit crystal formation and/or phase conversion depending on the concentration and amount of oxygen functional groups available for interactions.[75,85,76,83,75] While larger molecules are better at inhibiting aqueous attack, the small size of the Tris molecule was compensated by the high concentration present in solution.

Both amorphous and crystalline binary calcium aluminates were incubated in de-ionized water using various SA/V ratios. The effect of de-ionized water-Tris (DI-Tris) mixtures on microsphere hydration was also examined.

XX EXPERIMENTAL

A. Sample Preparation

1. Glass and Microsphere Formation

Glass and microsphere formation was described in Ch 1. III. A.

2. Calcium Aluminate Solution Reactions

CA microspheres were incubated at 25, 40 and 75˚C in de-ionized water, Tris (12 wt% used in Chapter 2) and Tris solutions diluted with de-ionized water (DI-Tris). Samples were treated for various time periods and at different SA/V ratios depending on the experiment that was to be performed on the sample. CASi, CAFe, SLS and crystalline CA micropsheres, as well as amorphous and crystalline CA frit, were also incubated at 25˚C in de-ionized water and Tris.

Some CA samples incubated at 25˚C for 48 hours were dried and heat treated at 40, 125, and 250˚C for 3 hours.

B. Inductively Coupled Plasma – Optical Emission Spectroscopy

The ICP-OES procedure described in Ch 2. XIV. E. was used to determine the amount of ions leached from the microspheres during treatments with deionized water or Tris. Microsphere incubation was performed using a SA/V ratio of ~58 to mimic the conditions observed during DNA attachment using the 1 mg/ml DNA solution.

C. Environmental Scanning Electron Microscopy

The ESEM procedure described in Ch 2. XIV. B. was used to examine all of the samples made in Ch 3. XX. A. 2. above.

D. X-Ray Diffraction

Hydrated crystal formation on the samples made in Ch 3. XX. A. 2. was examined using an x-ray diffractometer (Kristalloflex 810 X-Ray Diffractometer (XRD), Siemens, New York, NY) with a copper source. Dried samples were crushed with a mortar and pestle into a fine powder. The powder was mixed with isopropanol and poured onto a zero background (zb) holder. XRD scans were measured from 5 to 70˚ 2θ using a 0.2˚ step size with a 3 second scan time.

High temperature XRD was also performed on untreated CA microspheres and those treated in de-ionized water at 25 and 40˚C for 48 hours. Heat treatments were performed at 25˚C intervals from room temperature up to 1050˚C. Cobalt was used as the x-ray source for these measurements. Jade 8 was used to analyze all of the diffraction patterns.

XXI RESULTS

A. Sample Preparation

Consistent hydration of the CA microspheres was difficult due to the occurrence of almost immediate agglomeration upon contact with de-ionized water. The microspheres showed extreme degradation that became more severe with increased time in solution and temperature. After extended time periods and/or temperatures $\leq 40^{\circ}C$, the microspheres formed into hardened white, clumps that became difficult to separate. CASi and CAFe microspheres also exhibited hardened clumping but unlike the CA microspheres, the agglomeration was delayed and the microsphere morphology was still visible after 24 hours in solution. Incubation in de-ionized water had no apparent effect on the SLS microspheres.

CA microspheres reacted in the Tris and DI-Tris solutions down to 0.35 wt% Tris retained their original morphology and the agglomerates were easily separated. The microspheres treated with the 0.24 wt% Tris solution looked similar to that of the CA microspheres reacted with de-ionized water.

Both the amorphous and crystalline CA frit mixed with de-ionized water showed delayed agglomeration upon contact. After several hours the frit solidified, however the solution contained a large amount of particulate matter only observed in CA microsphere solutions above 40˚C.

B. Inductively Coupled Plasma – Optical Emission Spectroscopy

The calcium aluminate-based microspheres showed a steady increase in the concentration of calcium and aluminum ions in solution that reached a maximum after about 60 minutes. Figure 41 shows that the CA spheres leached the largest amount of calcium into solution, ~33 mM, and the largest drop in concentration after 24 hours. Figure 35, previously shown in Ch 2. XV., showed a continuous increase in calcium leached from the CA over 24 hours, with a maximum concentration of ~2.7 mM. The concentration of aluminum leached from the CA and CASi, shown in Figure 42, increases in a similar manner to the calcium solutions, although with almost twice the

concentration. The concentration of aluminum leached from the CAFe increased in a similar manner as the calcium, until a drastic increase in concentration at 60 minutes. The SLS microspheres only showed a minor amount of both calcium and aluminum ions after 60 minutes in solution but decreased below detection limits after 24 hours. Sodium was found to have leached from both the SLS and CAFe surfaces with a maximum concentration after 24 hours of 1.68 and 135.8 mM, respectively.

Figures 43 and 44 show that more calcium and aluminum ions were present in solution during the incubation of CA microspheres in de-ionized water at 25˚C than at 40˚C.

C. Environmental Electron Scanning Microscopy

Figures 45a-h show the gradual formation of the hydration products over time in 25˚C deionized water with an SA/V of ~1. Surface degradation and the formation of an x-ray amorphous gel layer was visible after only 1 minute in solution. The formation of irregularly shaped hexagonal plates began around 1 hour and fully formed plates were visible after 12 hours. After 24 hours, hexagonal plates fully covered the microspheres which were mostly present as large agglomerates. The protective crystal layer was found to be up to ~50 μm thick in some areas, with individual plates averaging ~5 μm thick and ~20 μm wide. Some crystals as wide as ~100 μm were found to have formed between agglomerated microspheres. Micron-sized 'fluff' balls of irregular plate crystals were always observed, shown in Figure 45e, even after the appearance of the fully formed plates. After 120 hours in solution the crystals began to disintegrate into matted clumps, shown in Figures 45i and j.

CA microspheres hydrated at at 40˚C developed the same hydration products but over a shorter time period. Fully formed hexagonal plates were already visible after 8 hours and hexagonal plate degradation occurred around 48 hours with the appearance of the stable isometric phase. Figures 45k-m show the trapezohedron crystals normally observed during these experiments while Figures 45m and n show other forms of the same cubic phase. The rod-like crystals were always present in CA incubated at 40˚C while the cubes in Figure 45n only appeared in pockets of aggregated microspheres incubated at 25˚C.

Evaporation of the de-ionized water limited the examination of the hydration products after 120 hours for the microspheres incubated at 40˚C and 168 hours (1 week) for those incubated at 25˚C. Both samples showed the presence of a radially connected cone shaped crystals that appeared to have formed around the boarders of hollowed spheres.

Figures 46 and 47 show that although the CASi and CAFe microspheres have severely degraded after 24 hours in solution, very little crystallization occurred. Debris on the CASi consisted mainly of amorphous chunks and sparse patches of thin, irregular hexagonal plate crystals. The CAFe also showed large amounts of amorphous debris but only a few scattered thin plates. If crystalline material was observed, it was present as 'fluff' balls in patches on the surface as shown in Figure 47a. Figure 47b shows the amorphous hydration layers that were also observed.

The CA microspheres treated in Tris, shown in Figure 48, showed no signs of surface damage or crystallization. The microspheres were enveloped in a Tris matrix that only appeared slightly striated in the samples incubated at 75˚C. The Tris matrix began to disappear at heat treatments above 125˚C with the formation of a brown coating after the 250˚C treatment, shown in Figure 49.

CA incubated in 0.35 wt% Tris, shown in Figure 50, showed surface damage and a low amount of Tris debris between the spheres. More damage and Tris debris was observed for microspheres incubated at 75˚C than at 25˚C. Heat treated samples showed less Tris debris after the 250˚C treatment but a brown coating did not form.

Figure 51 shows the formation of distorted hexagonal plates on the CA microspheres treated in 0.24 wt% Tris at 25˚C. However, most of the surface was covered by amorphous material mixed with matted irregular flakes. Distorted trapezohedron appeared at 40˚C and covered the surface of the microspheres incubated at 80˚C. Heat treatments performed on the 25˚C samples did nothing to the appearance of the hydration products.

The amorphous and crystalline CA frits, as well as the crystallized microspheres, formed the same hexagonal plate phase at 25˚C as the amorphous CA microspheres.

D. X-Ray Diffraction

Samples treated for 48 hours with a SA/V ratio of 1 were found to produce the largest amount of well formed crystals. Other SA/V ratios produced similar crystals but with more amorphous material, making phase identification difficult. The slight amount of crystalline material formed on the CASi microspheres was determined to be the same phase as that formed on the CA microspheres. The amount of crystalline material formed on the CAFe microspheres was too low to be detected by XRD. Table XIII summarizes the characteristic basal spacings for the various hydrated crystalline phases formed in this study and also those of previously reported hydrates.

Figure 52 shows that the amorphous CA microspheres begin to crystallize at ~825˚C, with full crystallization achieved by ~925˚C. The phase was identified as a form of mayenite ($Ca_{11.3}Al_{14}O_{32.3}$) and is shown in Figure 53.

Figure 54 shows several possible phases for the hexagonal plate crystals formed at 25˚C. The calcium aluminum oxide hydroxide hydrate phase, $3CaO•Al_2O_3•Ca(OH)_2•18H_2O$ (C3ACH18), most closely matched the peak locations and intensities. The commonly observed C2AH8 phase was also found to match the peak locations fairly well, and was considered to be a more likely phase since C3ACH18 had never been reported in prior hydration experiments. Also, the characteristic basal spacings for the phases formed in this study are a combination of the reported basal spacings for the α- and β- C2AH8 phases shown in Table XIV. Figures 55 and 56 suggest that CAH10 could have also possibly formed during CA hydration at higher SA/V ratios. The hexagonal plates begin to dehydrate to a possible C2AH6 phase at ~50˚C, shown in Figure 57. Above this temperature, all peaks disappear until the formation of mayenite at ~825˚C.

Figure 59 shows the C3AH6 phase commonly reported to form in hydration studies performed at temperatures study $\geq$ 30˚C. An $Al(OH)_3$ phase could have also possibly formed. The characteristic basal spacings are a degree lower than those previously reported and is most likely the result of differences in the SA/V ratios. An unidentifiable minor phase is also present which disappears at ~250˚C. At ~275˚C, the basal spacings exactly match the previously reported spacings for C3AH6. Figures 60 and 61 shows that C3AH6 and $Al(OH)_3$ are stable until ~300˚C when dehydration leads

to the formation of another form of mayenite (C12A7). More peaks appear at ~825˚C where the amorphous material from the hydrated microspheres crystallizes to the previously reported form of mayenite.

Figure 61 shows an overlay of the hydrated crystal phases formed during the incubation periods at 25 and 40˚C discussed above. The presence of amorphous material is noticeable in both curves at ~12˚ 2θ.

The Tris solution completely inhibited the formation of any crystalline hydrates up to 48 hours at 75˚C. However, the Tris itself did crystallize as shown in Figures 62 and 63. The 0.35 wt% Tris solution showed results similar to that of the Tris solution and therefore the figures were not included.

The 0.24 wt% Tris solution inhibited hydrated crystal formation until 40˚C where C3AH6 formed along with crystalline Tris, shown in Figures 64 and 65. At 75˚C, shown in Figure 66, the Tris phase disappeared but the C3AH6 phase is still present, although exhibiting a lesser degree of crystallinity.

Figure 67 is an overlay of the hydration products formed during CA incubation in de-ionized water, 0.24 wt% Tris and Tris at 40˚C for 48 hours. C3AH6 formed during incubation in both the de-ionized water and 0.24 wt% Tris, but with the 0.24 wt% Tris showing a lesser degree of crystallinity and also a shift to higher d-spacings.

Figures 68 and 69 show that the crystalline material hydrated at 25˚C produces a similar hydrated crystal phase to that of the amorphous material. The C2AH8 phase fits the crystalline pattern better than the phase formed from the amorphous sample where the basal spacings were higher than those previously reported.

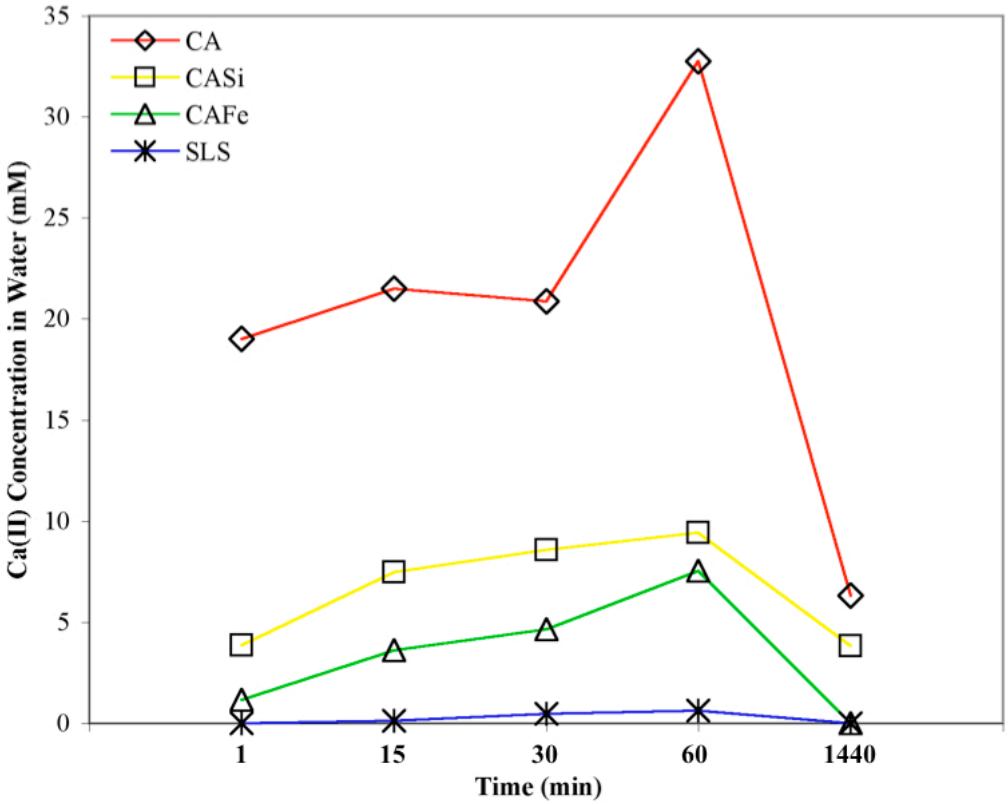

Figure 41. Concentration of Ca(II) ions leached into the de-ionized water from the CA, CASi, CAFe and SLS microspheres after various time periods. Error is within the symbol markers on the curves.

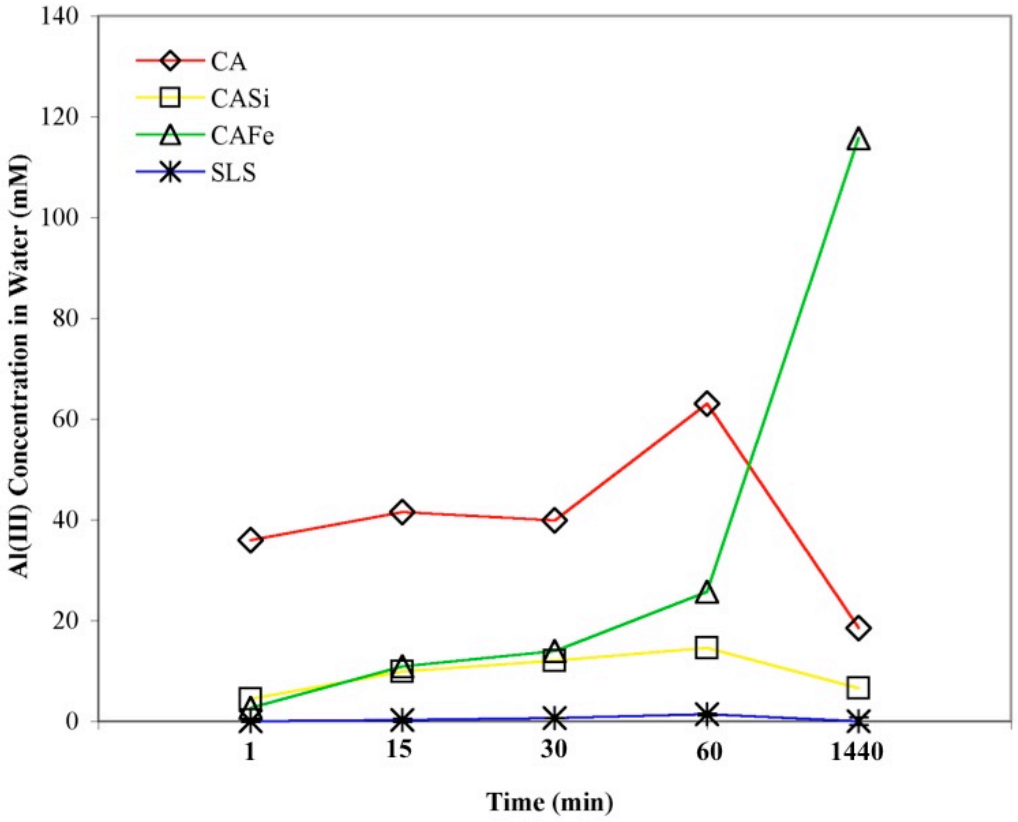

Figure 42. Concentration of Al(III) ions leached into the de-ionized water from the CA, CASi, CAFe and SLS microspheres after various time periods. Error is within the symbol markers on the curves.

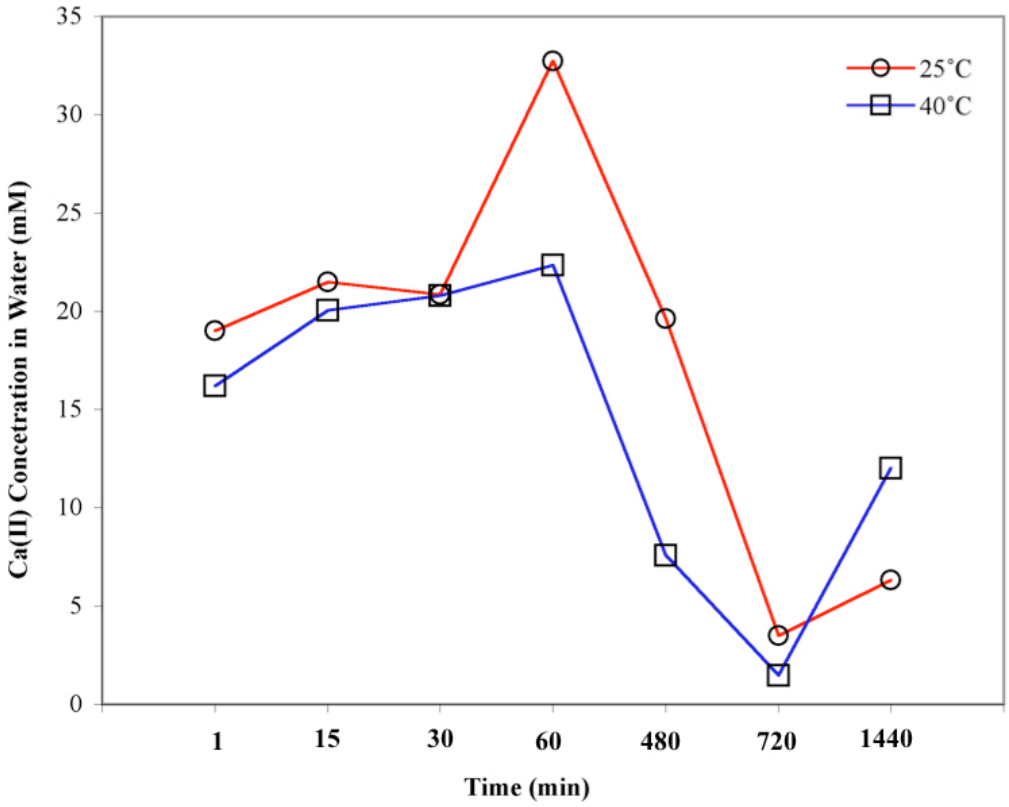

Figure 43. Concentration of Ca(II) ions leached into the de-ionized water from the CA microspheres after various time periods in 25˚C and 40˚C solutions. Error is within the symbol markers on the curves.

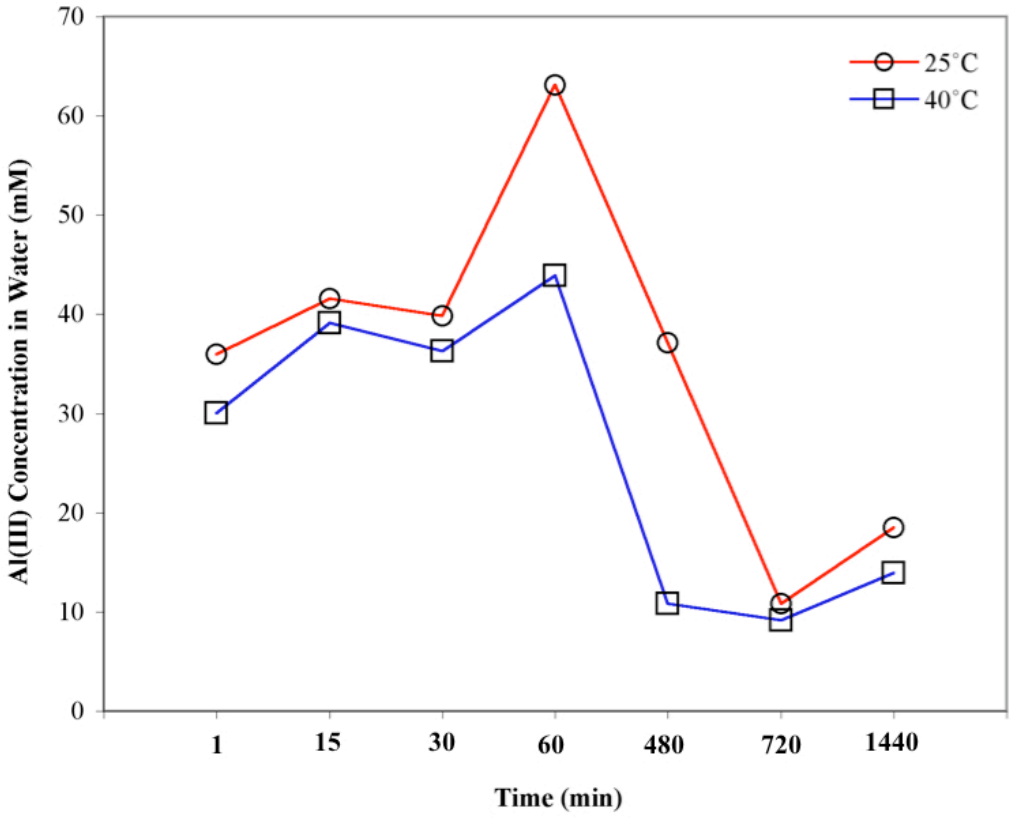

Figure 44. Concentration of Al(III) ions leached into the de-ionized water from the CA microspheres after various time periods in 25˚C and 40˚C solutions. Error is within the symbol markers on the curves.

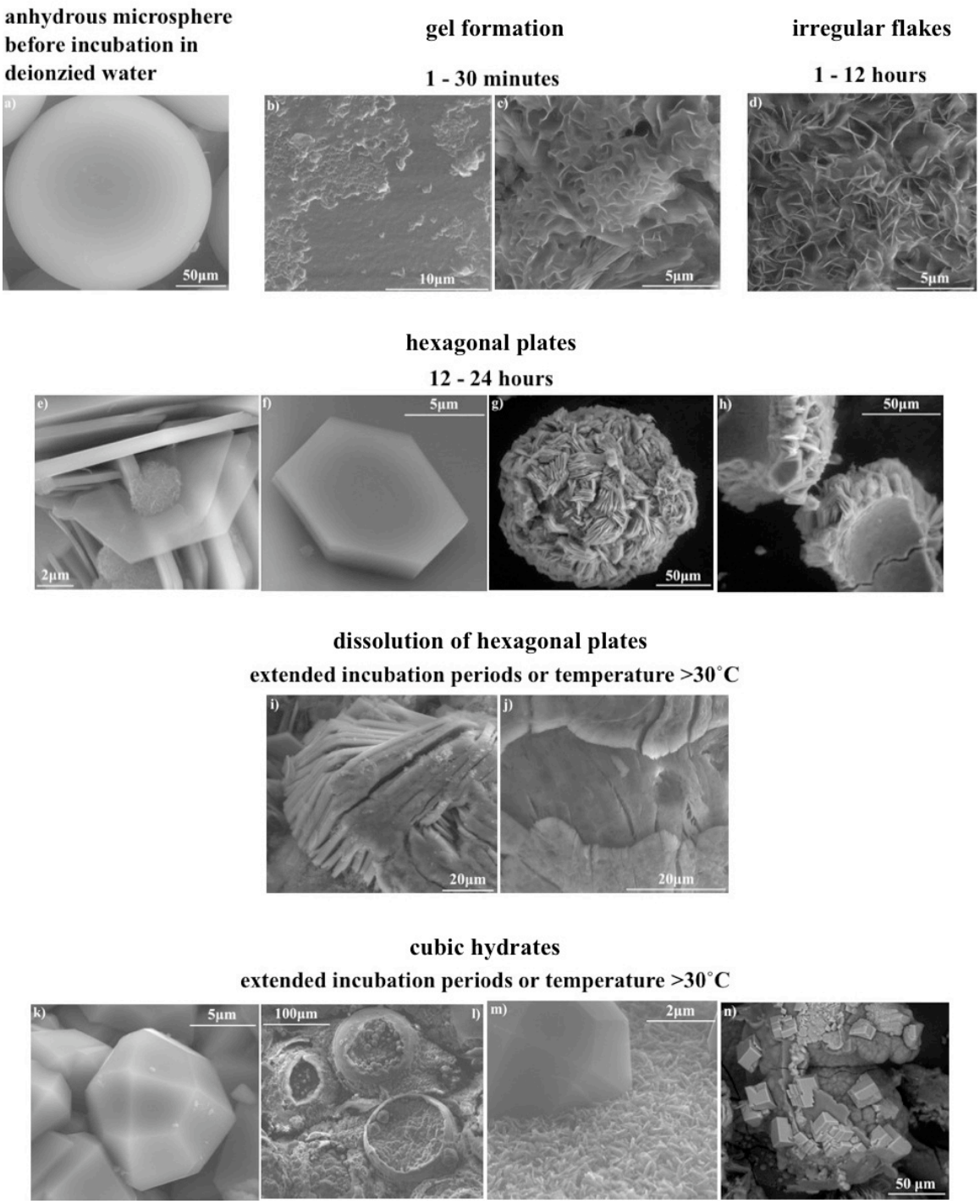

Figure 45. Timeline of hydration product formation on the CA surface during incubation in de-ionized water at both 25 and 40˚C.

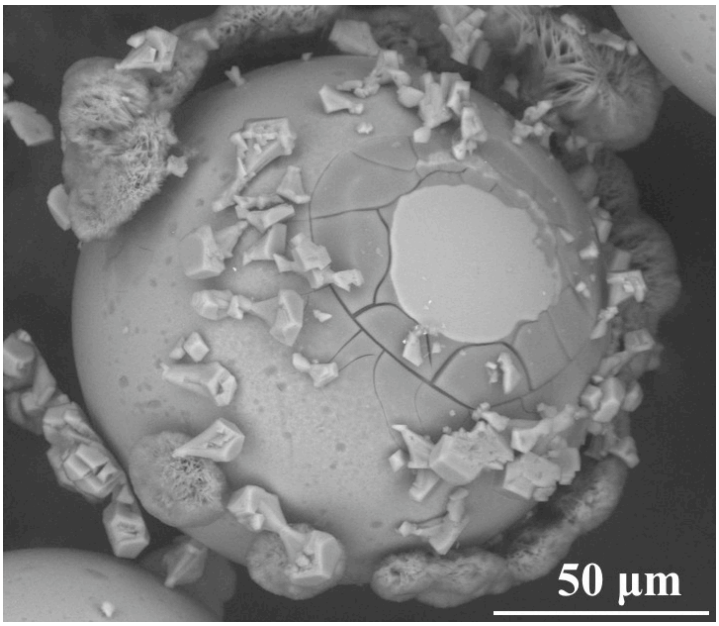

Figure 46. CASi incubated in de-ionized water for 24 hours at 25˚C.

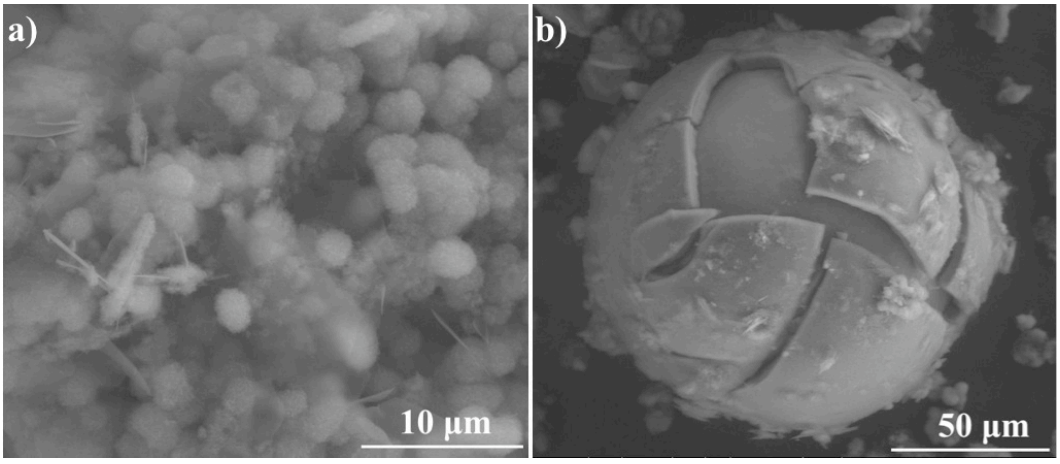

Figure 47. CAFe incubated in de-ionized water for 24 hours at 25˚C.

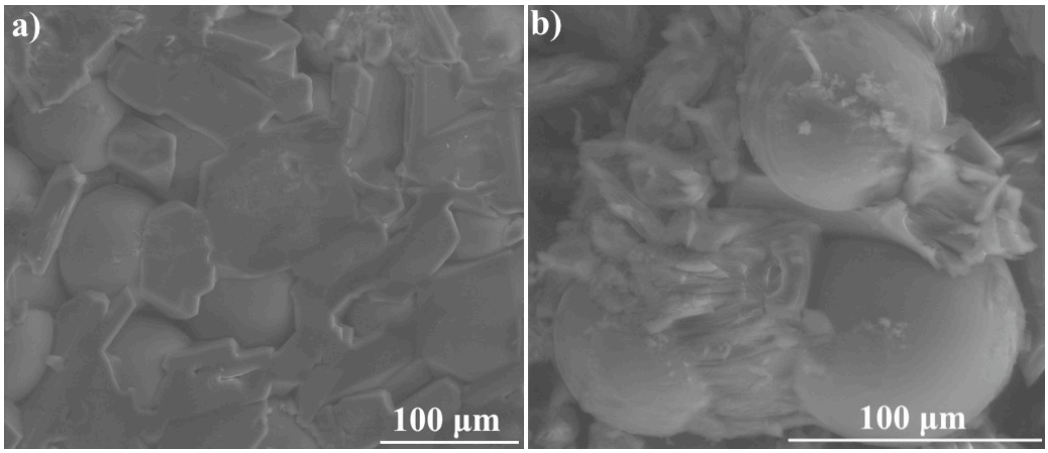

Figure 48. CA incubated in Tris for 48 hours at a) 25˚C and b) 75˚C.

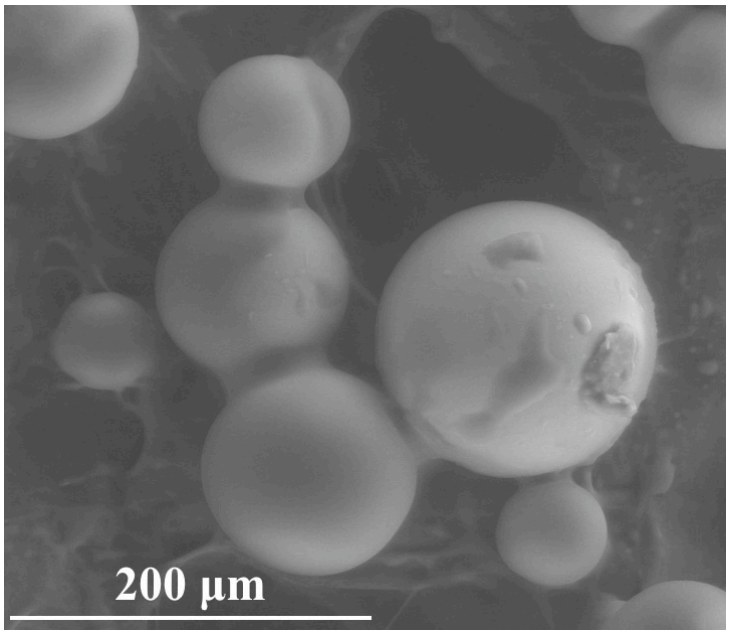

Figure 49. CA incubated in Tris for 48 hours at 25˚C and then heat treated for 1 hour at 250˚C.

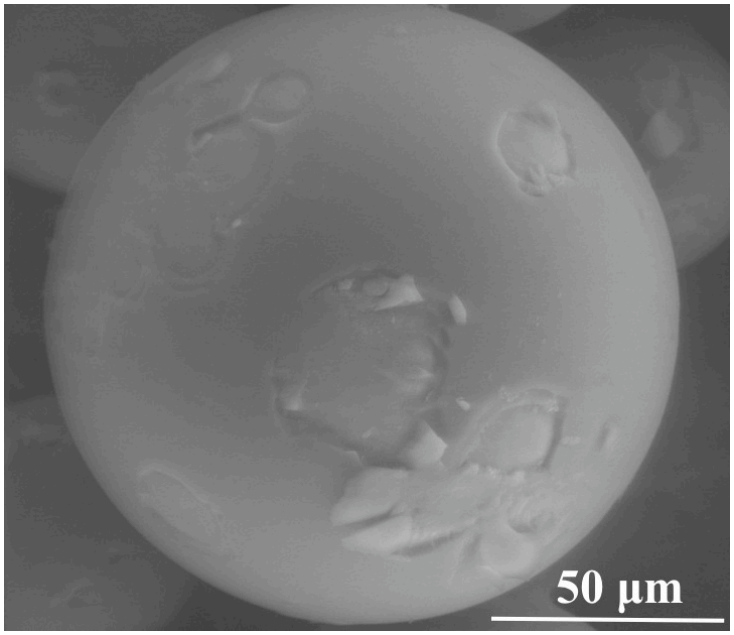

Figure 50. CA incubated in 0.35 wt% Tris for 48 hours at 40˚C.

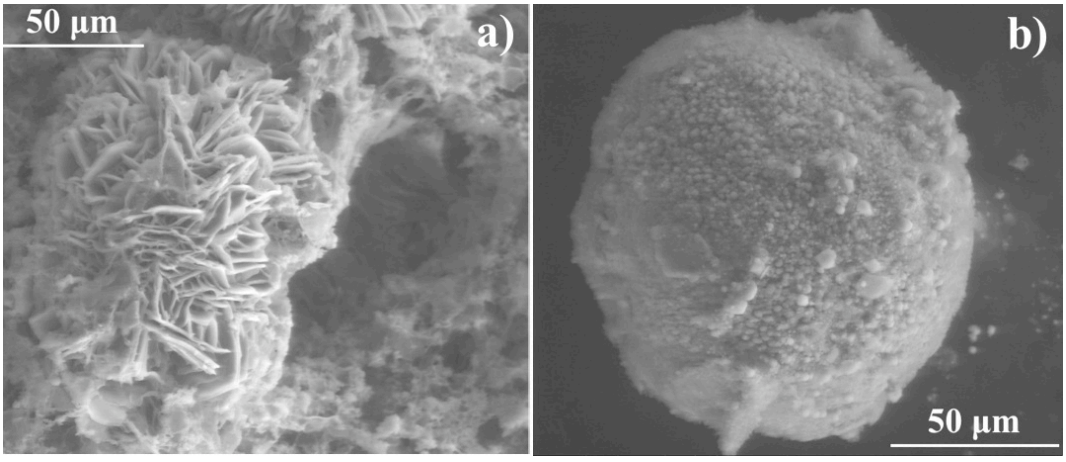

Figure 51. CA incubated in 0.24 wt% Tris for 48 hours at a) 25˚C and b) 75˚C.

Table XIII. Phase and Characteristic Basal Spacing of the Hydrated Crystals Formed During CA Incubation in De-ionized Water.

Solution	SA/V	Treatment*	Phase	Characteristic Basal Spacing (Å)			
de-ionized water	1	25˚C	C3ACH18 C2AH8	10.7	5.3	3.5	2.9
	58	25˚C	C3ACH18 C2AH8 CAH10	10.1	5.1	3.5	2.8
		25˚C - HT 50˚C	C2AH6	8.6	4.3	3.8	2.9
		25˚C - HT 125˚C	unidentified	7.4	3.7	2.8	2.4
		25˚C - HT 250˚C	unidentified	7.3	3.7	2.8	-
		40˚C	C3AH6 Al(OH)3	5.0	4.4	3.3	3.1
		40˚C - HT 275˚C	C3AH6	5.1	4.4	3.4	3.1
		40˚C - HT 300˚C	mayenite (C12A7)	4.9	3.0	2.7	2.5
12 wt% Tris	1	25˚C	Tris (C4H11NO3HCl)	10.7	5.3	3.5	2.9
0.25 wt% Tris	1	25˚C - HT 40˚C	Tris (C4H11NO3HCl) C3AH6	7.9	5.2	4.5	3.2
			Previously Reported Phases and Characteristic Basal Spacings (Å)				
			α - C4AH19	10.7	5.4	4.2	3.9
			α - C4AH13	8.2	4.1	3.9	2.9
			β - C4AH13	7.9	4.0	2.9	2.9
			C4AH11	7.4	3.9	3.7	2.9
			α - C2AH8	10.7	5.4	4.1	4.0
			β - C2AH8	10.5	5.2	3.5	2.9
			C3AH6	5.1	4.5	3.4	3.1

* incubation time in solution was 48 hours, HT patterns were collected using the high temperature XRD

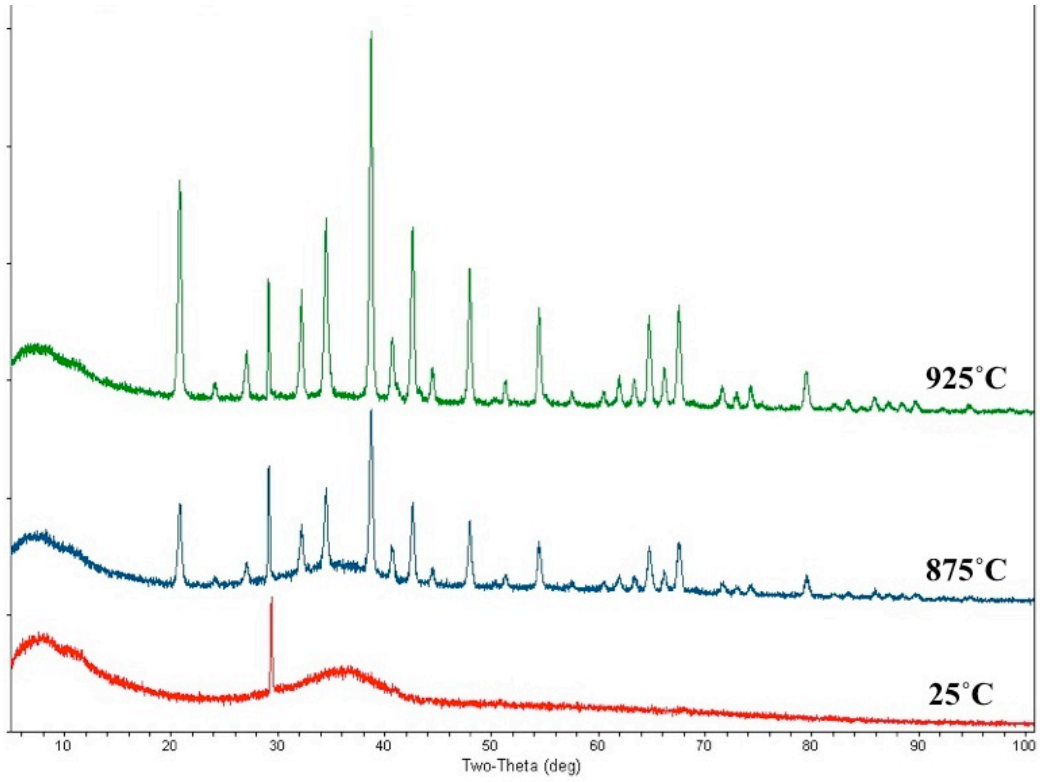

Figure 52. High temperature XRD pattern of the untreated CA microspheres. The peak at 30˚ 2θ is from the zero background holder.

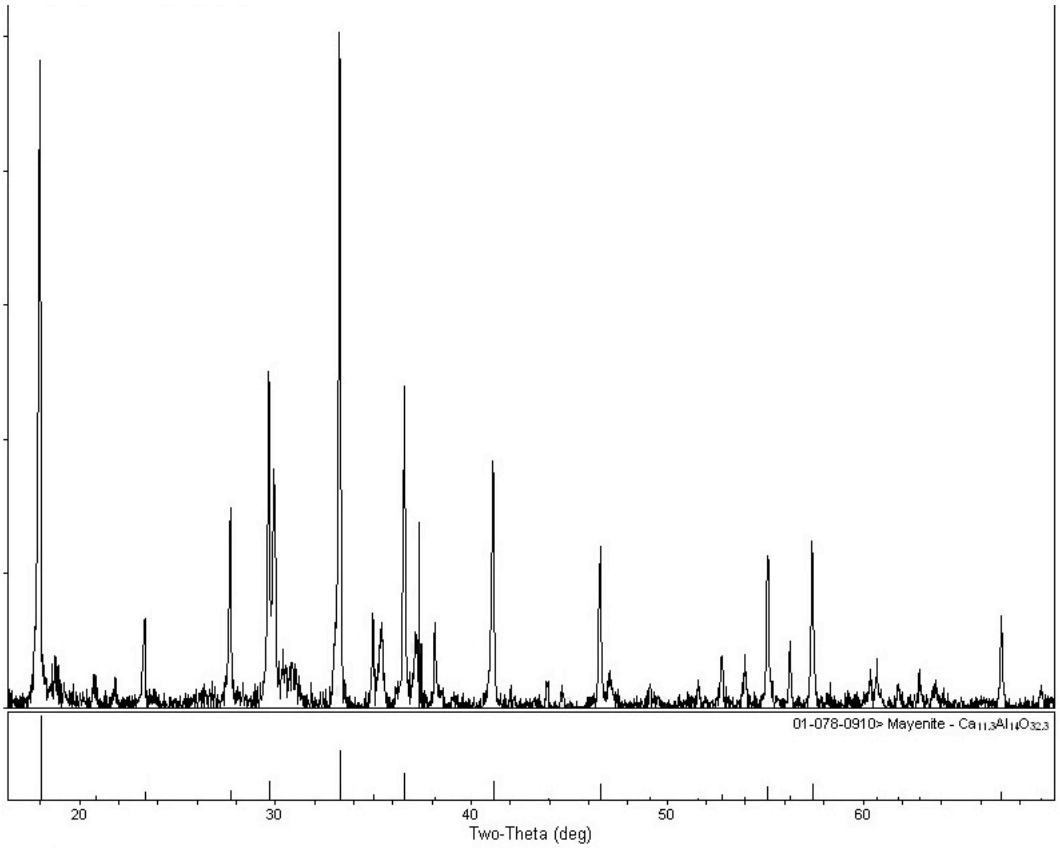

Figure 53. High temperature XRD pattern of the CA microsphere heated to 925˚C.

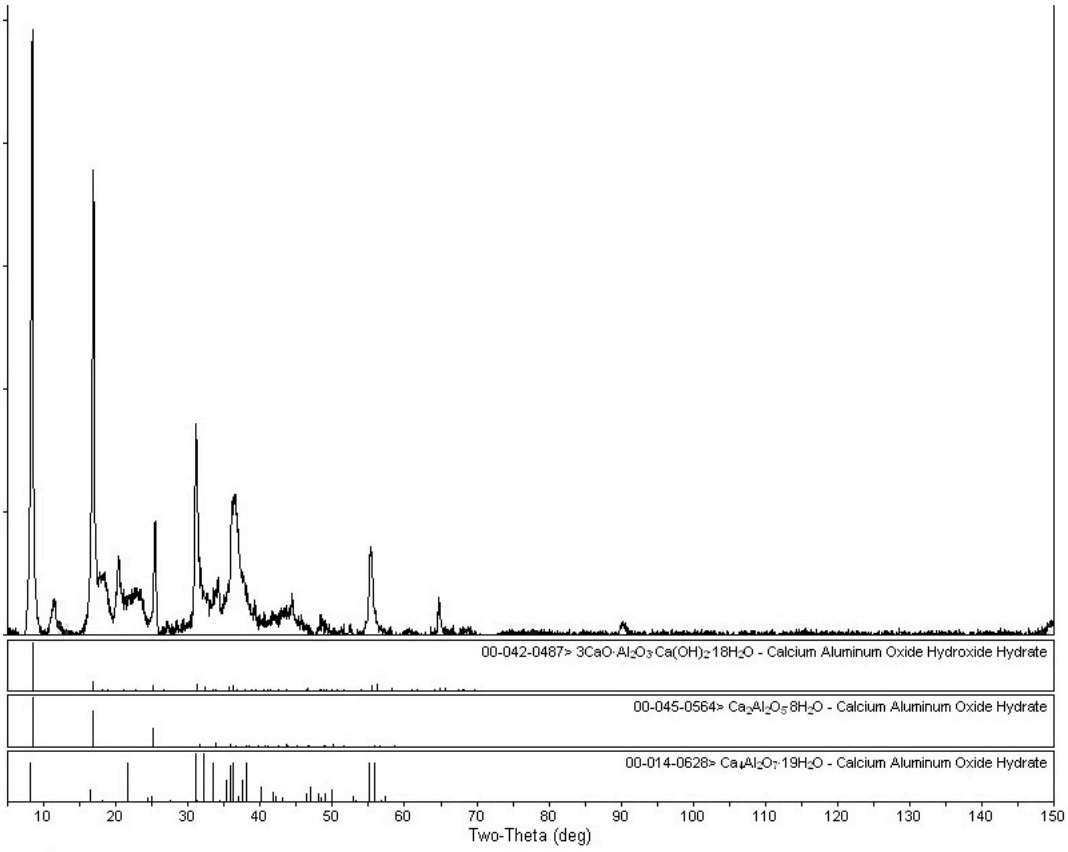

Figure 54. XRD pattern showing several possible phases for the hydrated crystals formed on the CA microspheres during incubation in de-ionized water at 25˚C for 48 hours, using a SA/V ratio of 1.

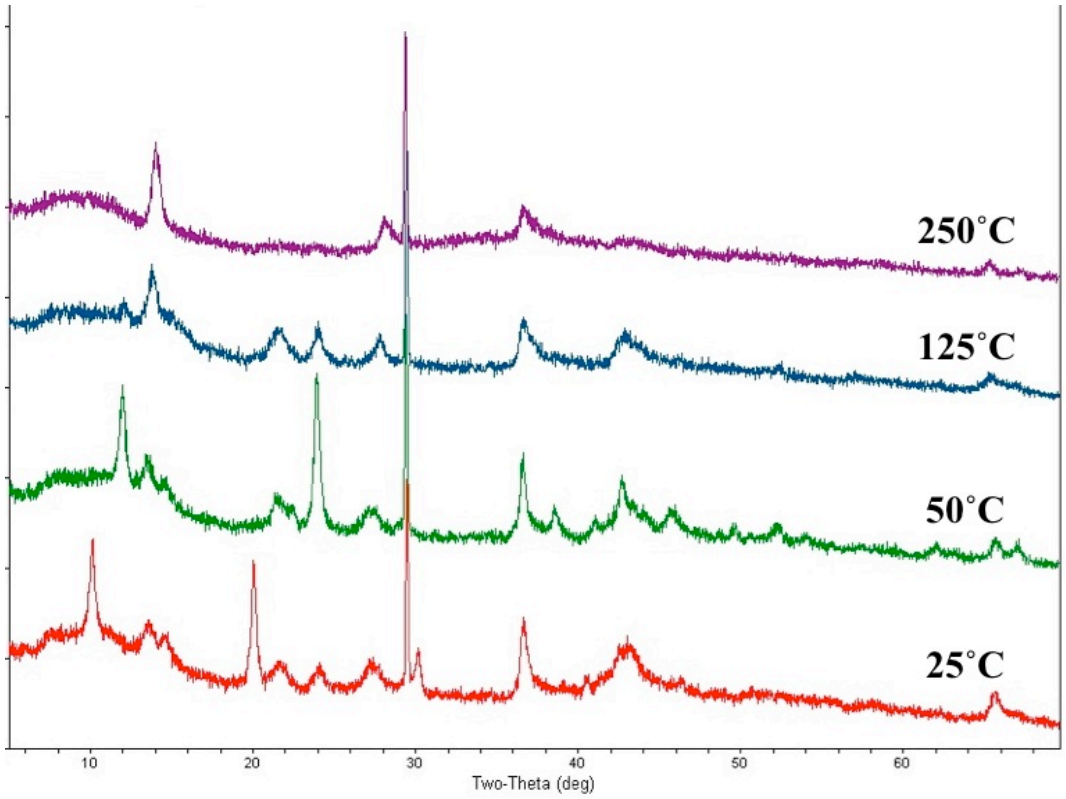

Figure 55. High temperature XRD pattern of the hydrated phases formed on CA microspheres incubated in de-ionized water at 25˚C for 48 hours.

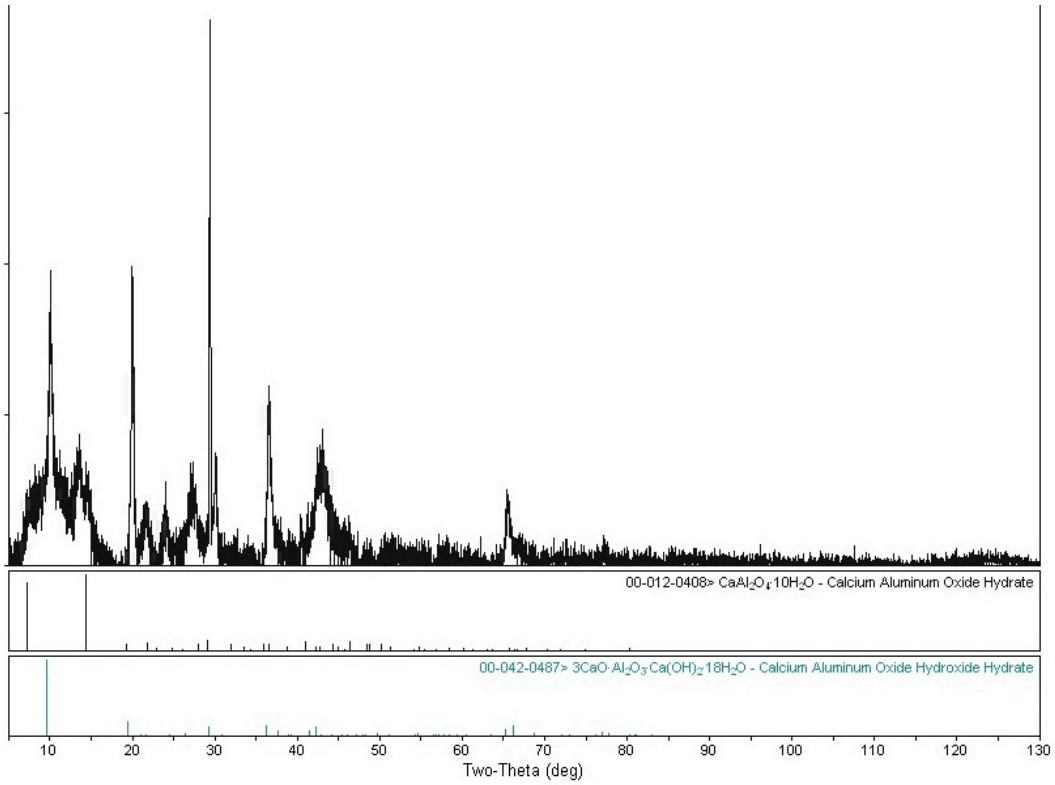

Figure 56. XRD pattern showing several possible phases for the hydrated crystals formed on the CA microspheres during incubation in de-ionized water at 25˚C for 48 hours, using a SA/V ratio of 58.

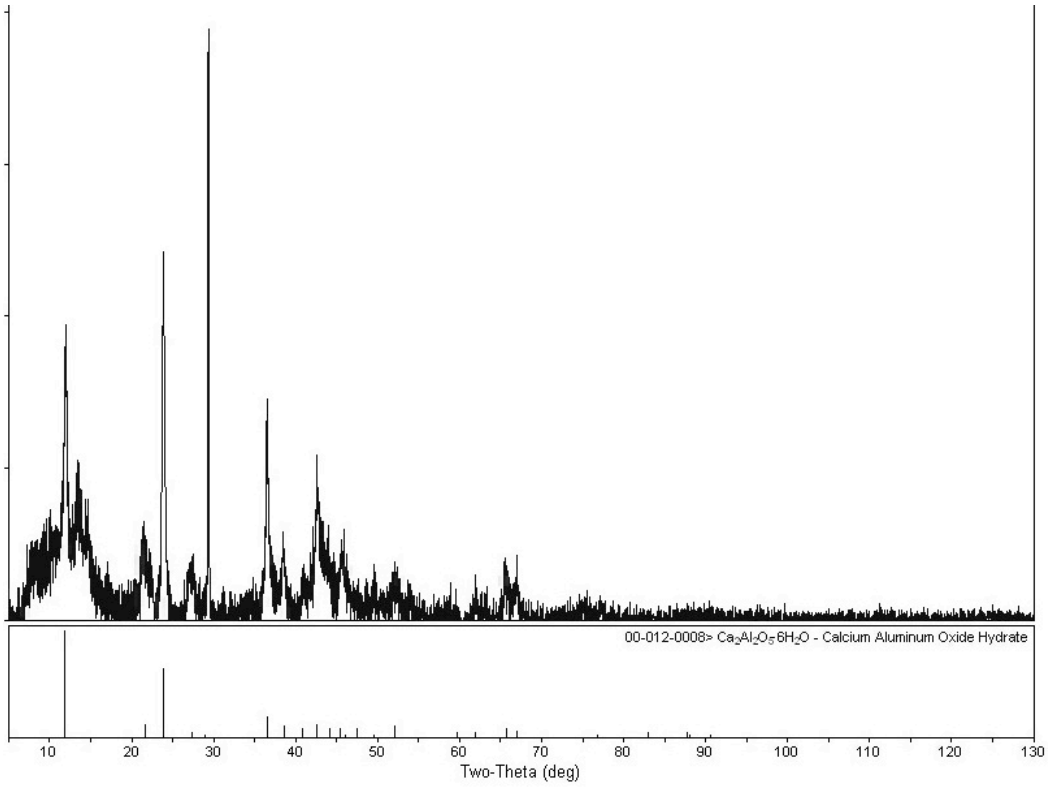

Figure 57. XRD pattern showing the phase formed on the CA microspheres during incubation in de-ionized water at 25˚C for 48 hours, using a SA/V ratio of 58, and then heat treated at 50˚C for 1 hour.

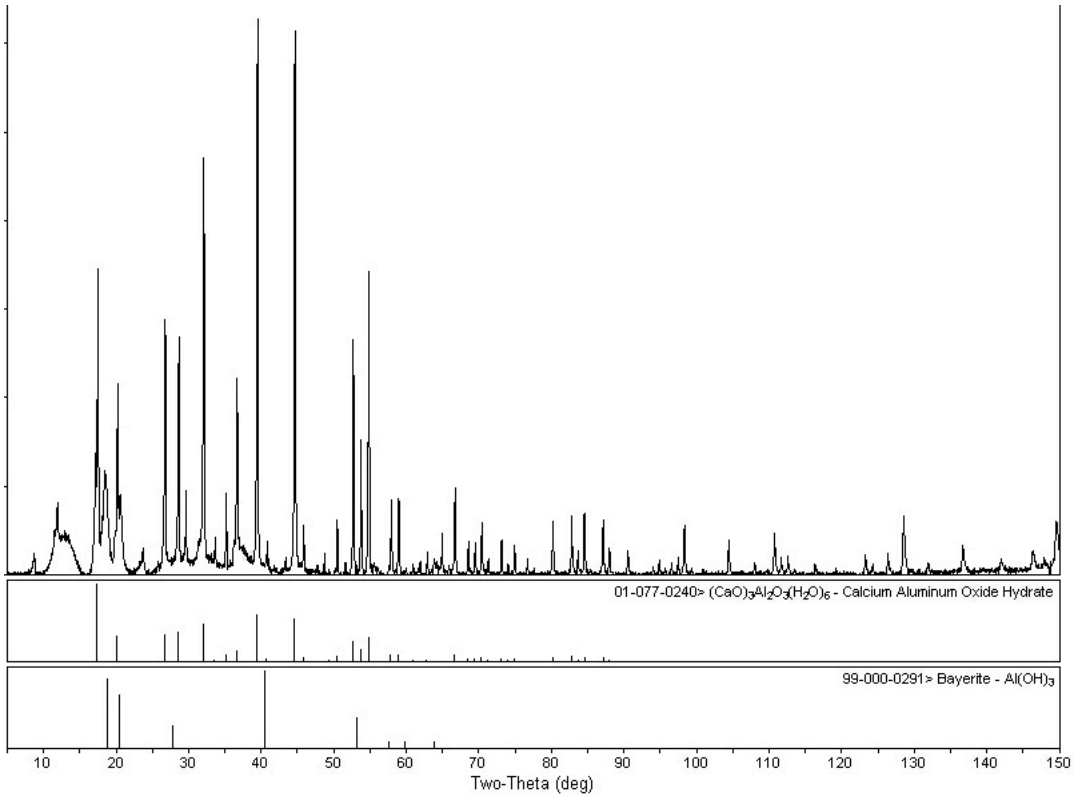

Figure 58. XRD pattern showing several possible phases for the hydrated crystals formed on the CA microspheres during incubation in de-ionized water at 40˚C for 48 hours, using a SA/V ratio of 58.

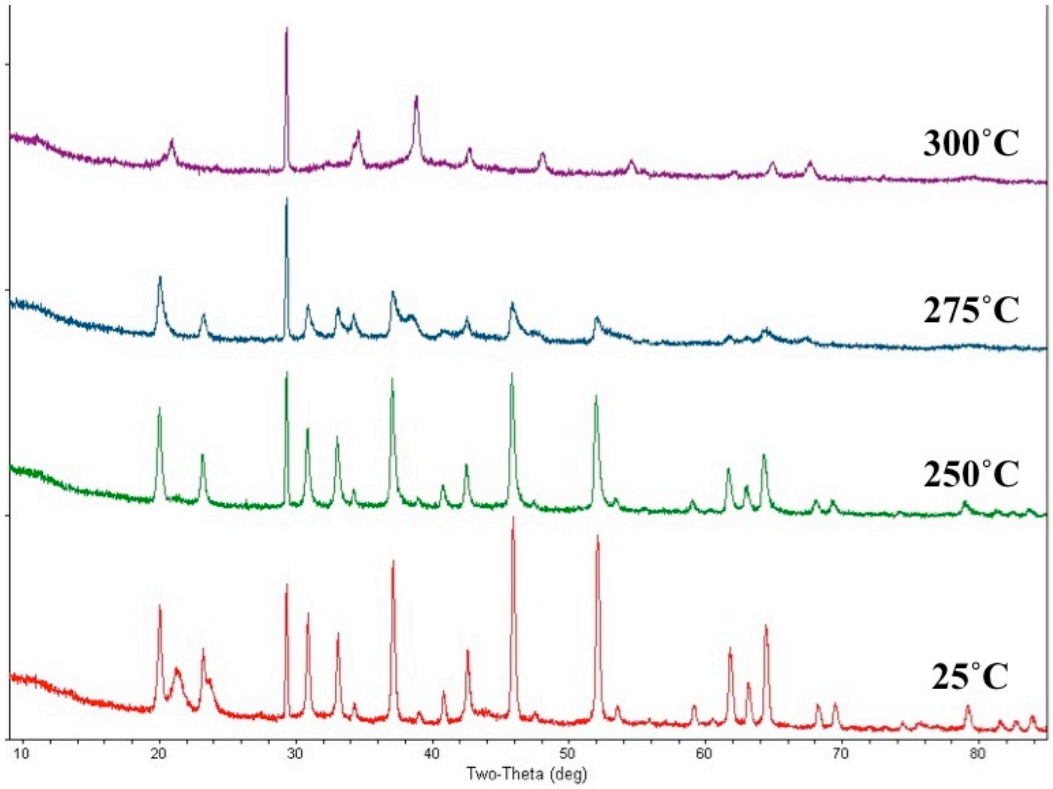

Figure 59. High temperature XRD of hydrates formed at 40˚C for 48 hours.

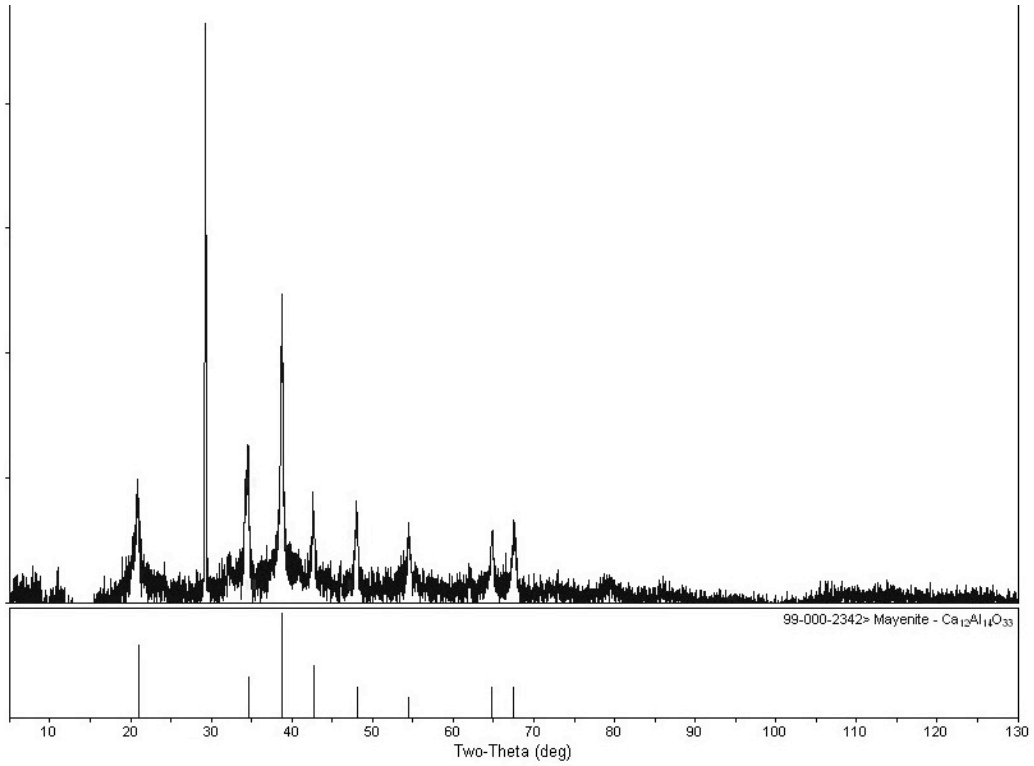

Figure 60. XRD pattern showing the phase formed on the CA microspheres during incubation in de-ionized water at 40˚C for 48 hours, using a SA/V ratio of 58, and then heat treated at 300˚C for 1 hour.

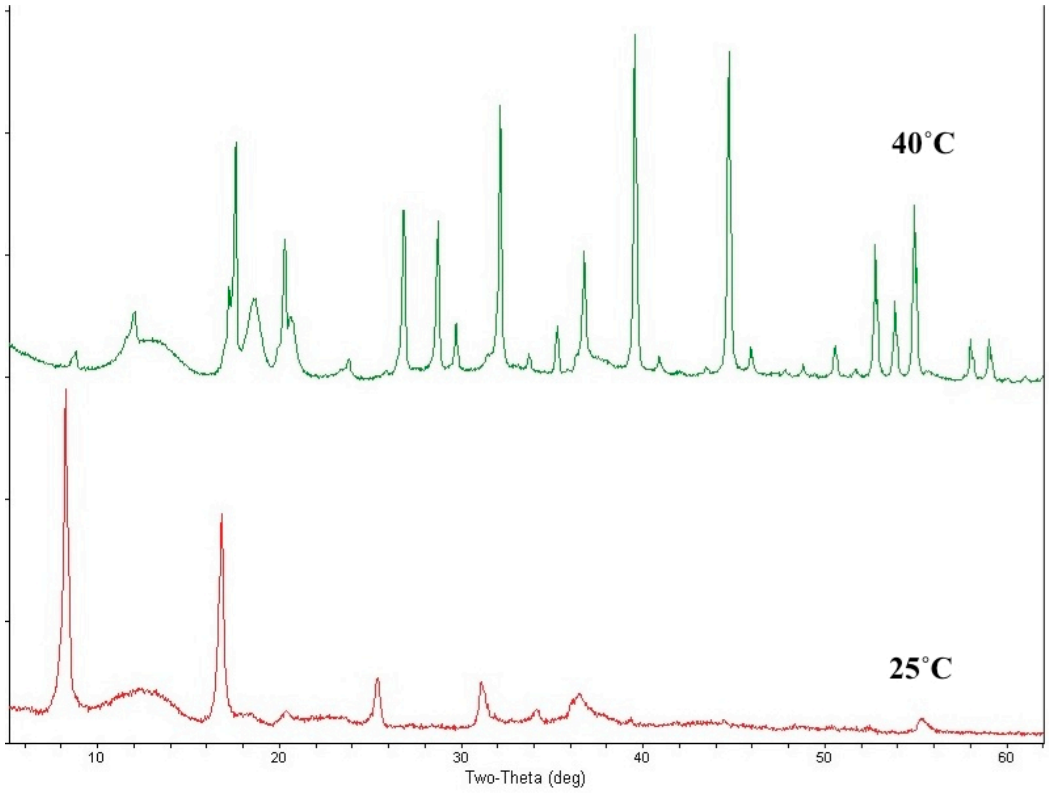

Figure 61. Overlay of the XRD patterns of the hydration products formed at 25 and 40˚C after incubation in de-ionized water for 48 hours.

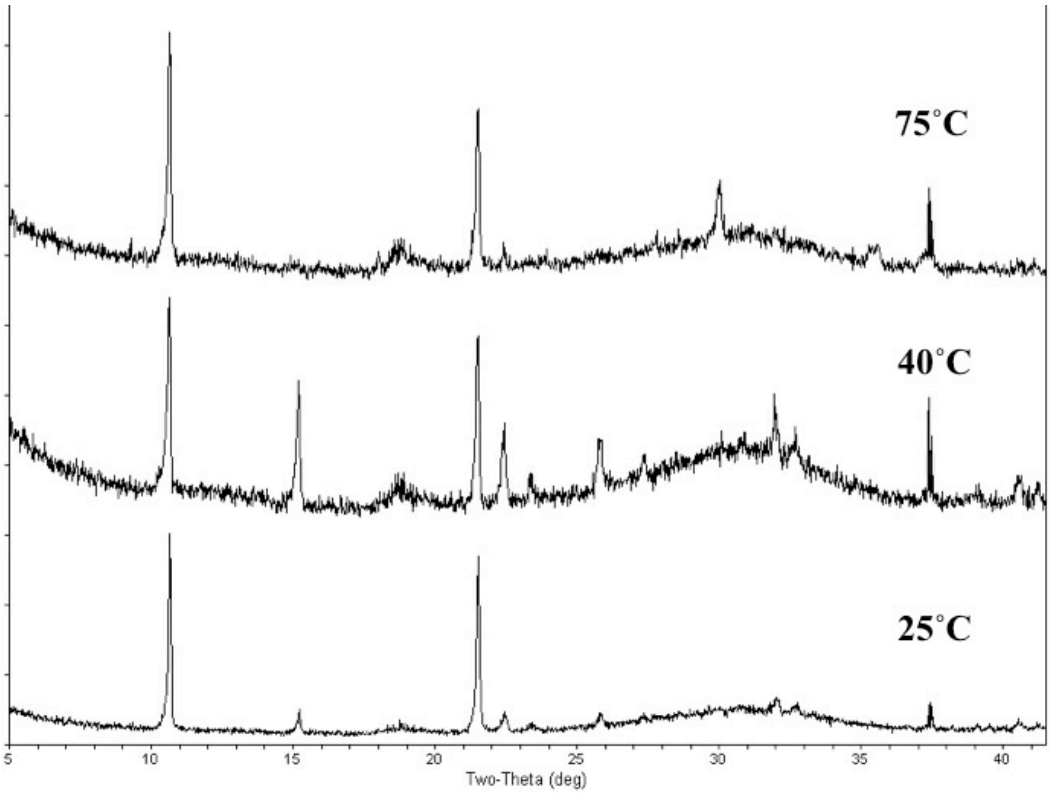

Figure 62. XRD pattern of the hydrated phases formed on the CA microspheres incubated in Tris solution at 25, 40 and 75˚C for 48 hours.

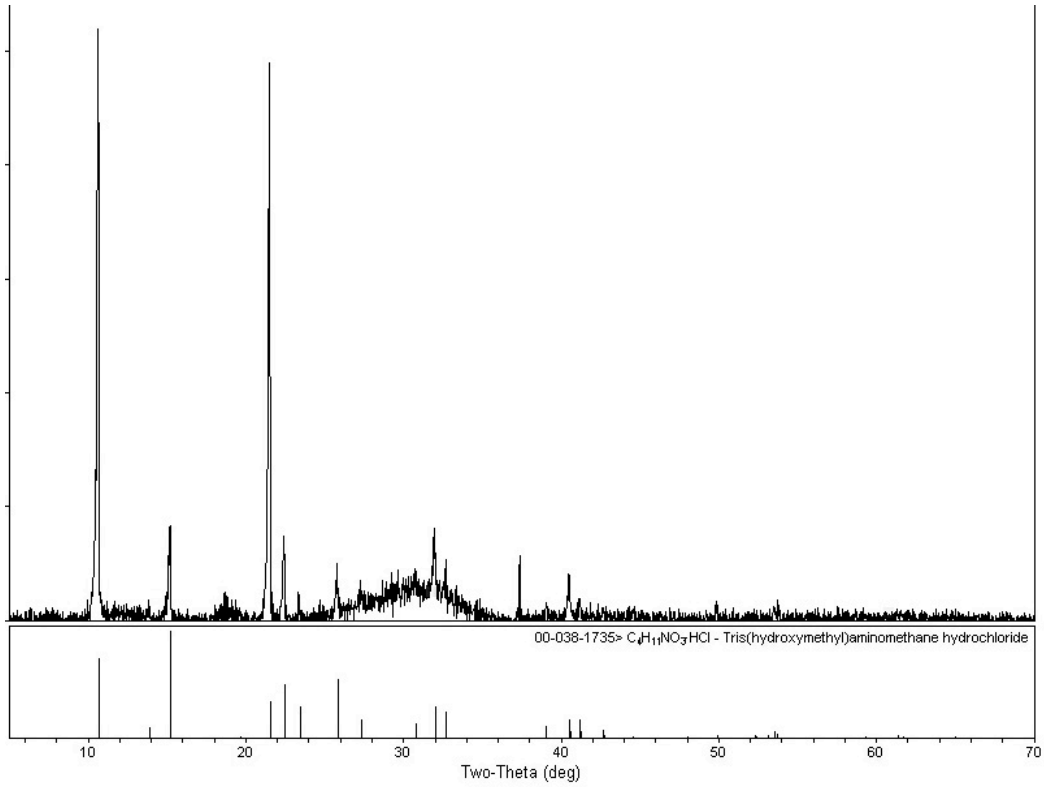

Figure 63. XRD pattern of the hydrated phases formed on the CA microspheres incubated in Tris solution at 40˚C for 48 hours.

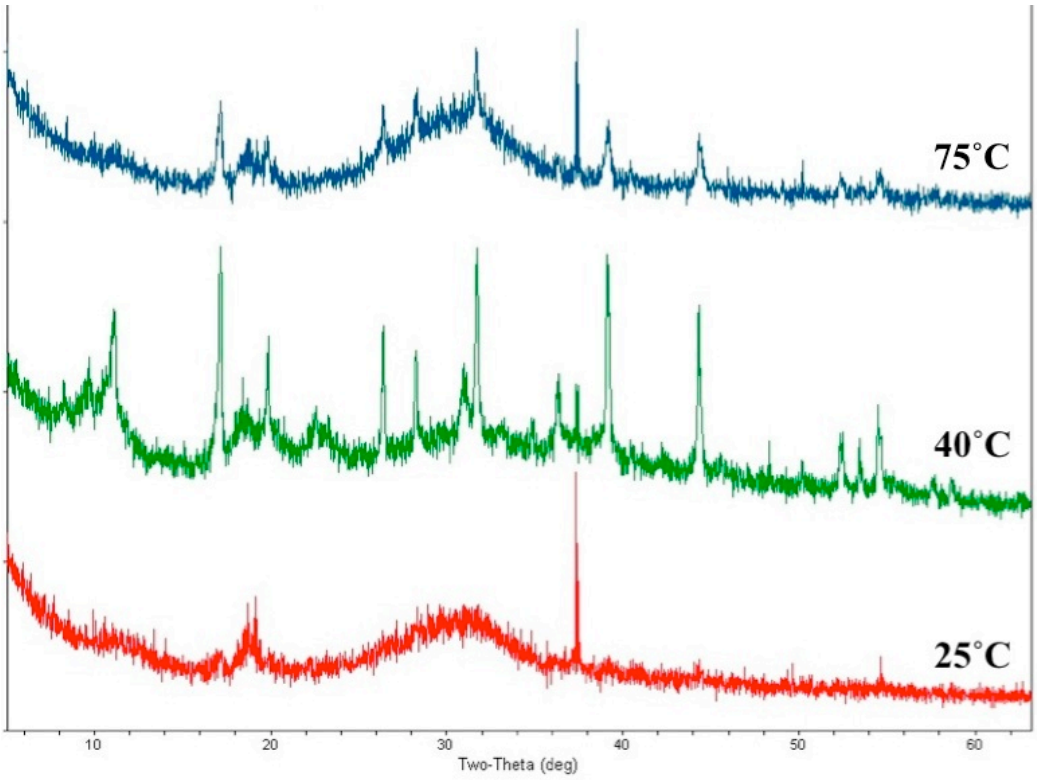

Figure 64. XRD pattern of the hydrated phases formed on the CA microspheres incubated in the 0.24 wt% Tris solution at 25, 40 and 75˚C for 48 hours.

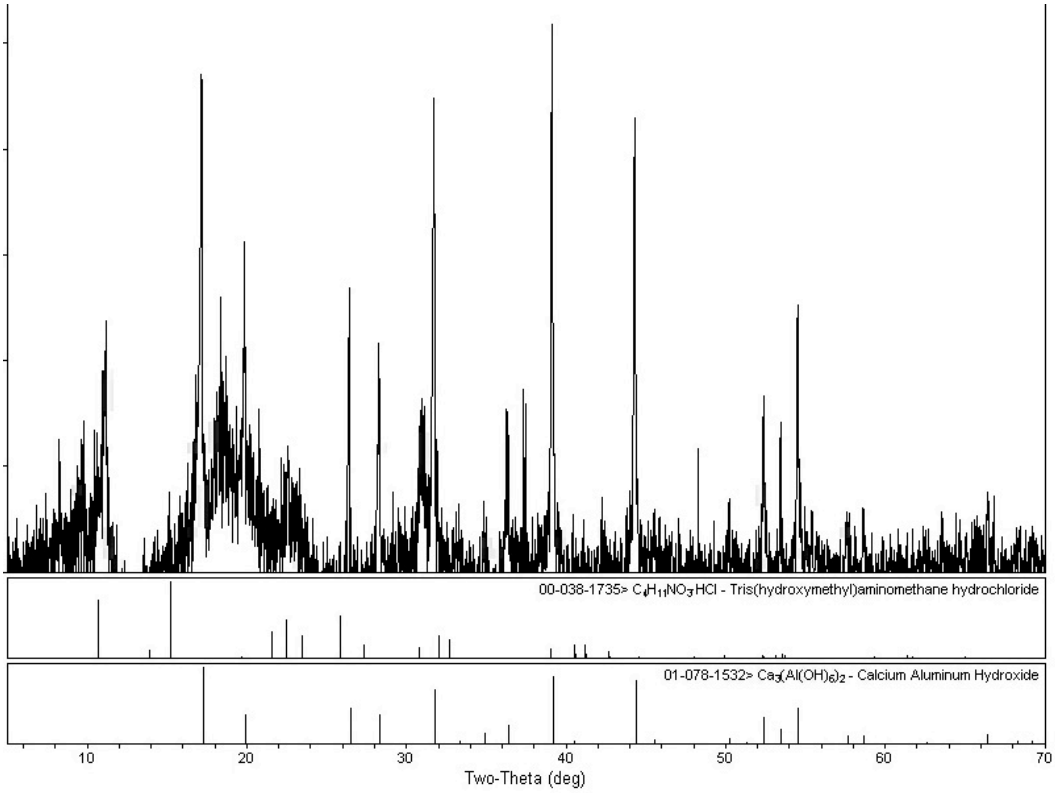

Figure 65. XRD pattern of the hydrated phase formed on the CA microspheres incubated in the 0.24 wt% Tris solution at 40 ˚C for 48 hours.

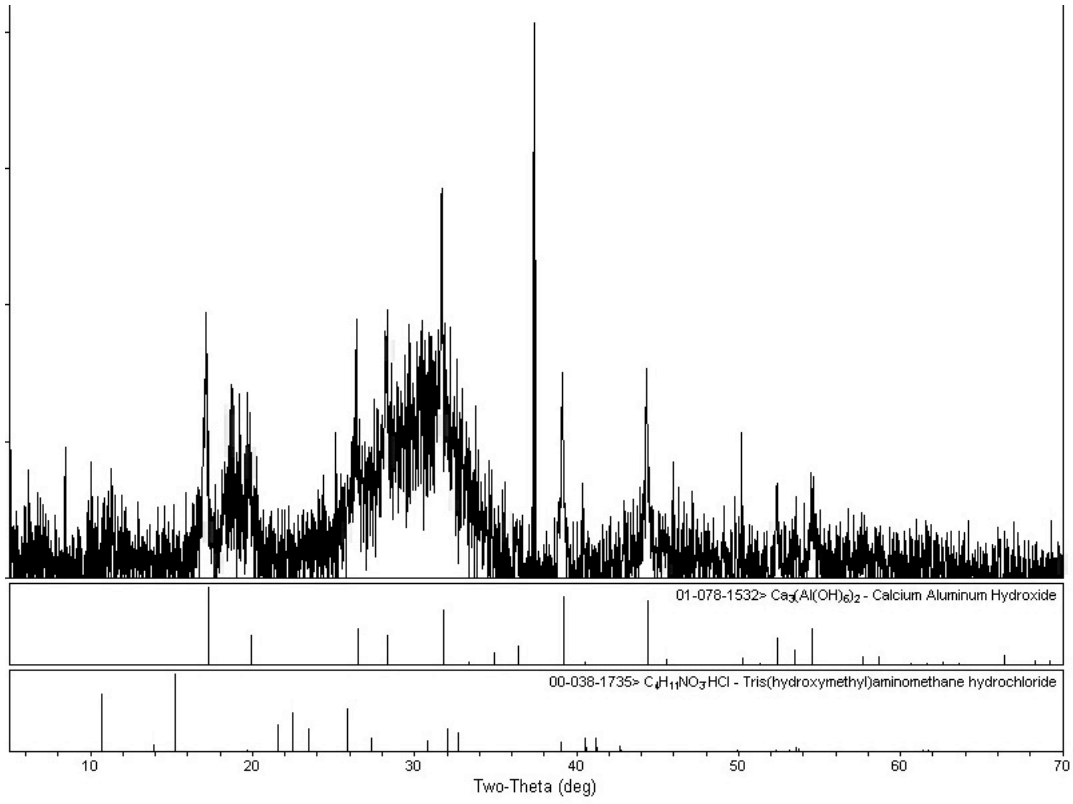

Figure 66. XRD pattern of the hydrated phases formed on the CA microspheres incubated in the 0.24 wt% Tris solution at 75˚C for 48 hours.

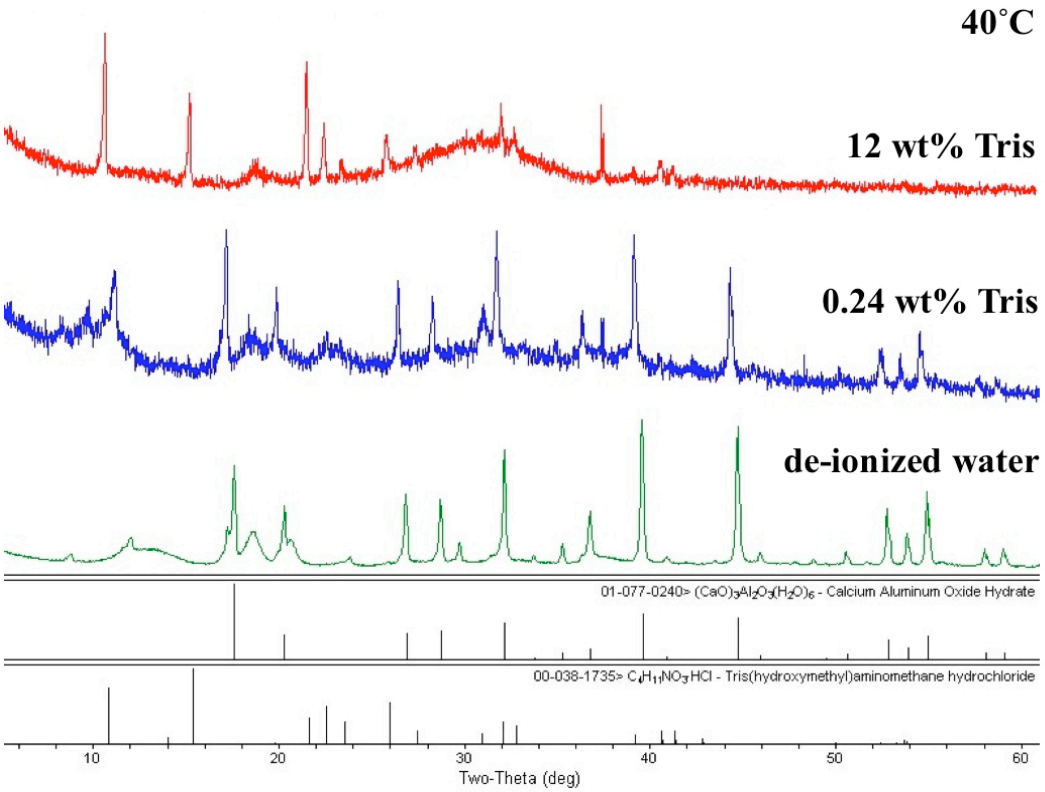

Figure 67. Overlay of XRD patterns of the CA microspheres incubated in de-ionized water, Tris and the 0.24 wt% Tris solution at 40˚C for 48 hours.

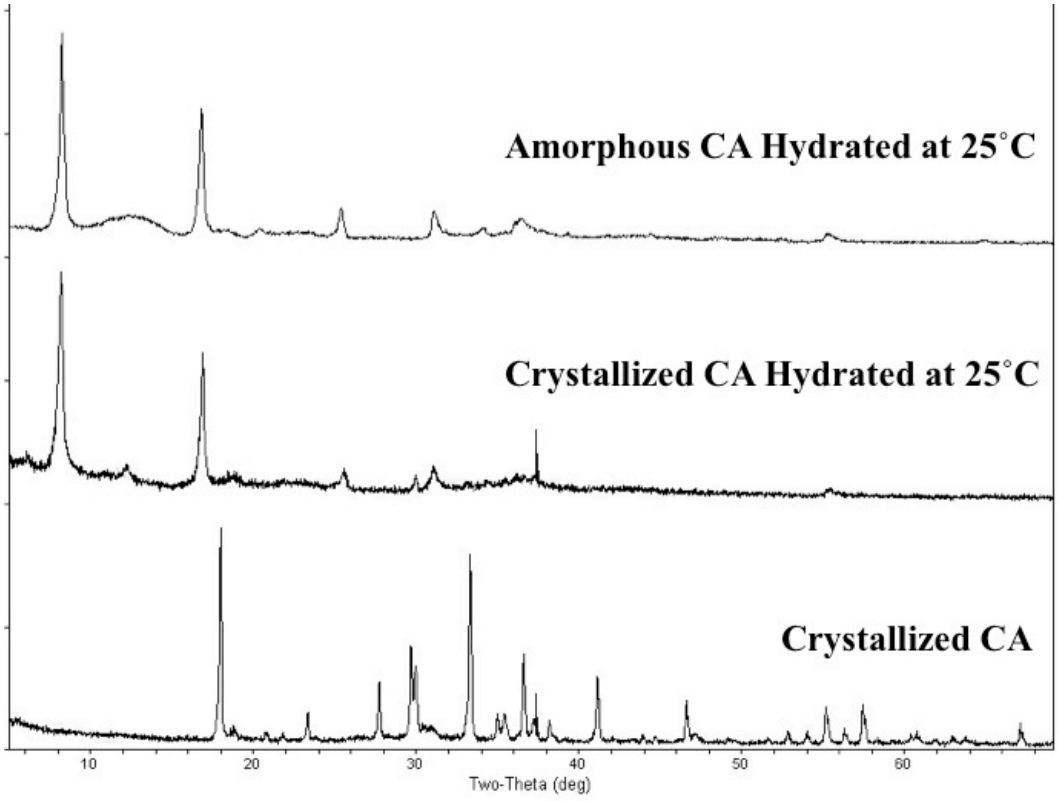

Figure 68. XRD pattern of the hydrated products formed on the crystalline CA and amorphous microspheres incubated at 25˚C for 48 hours.

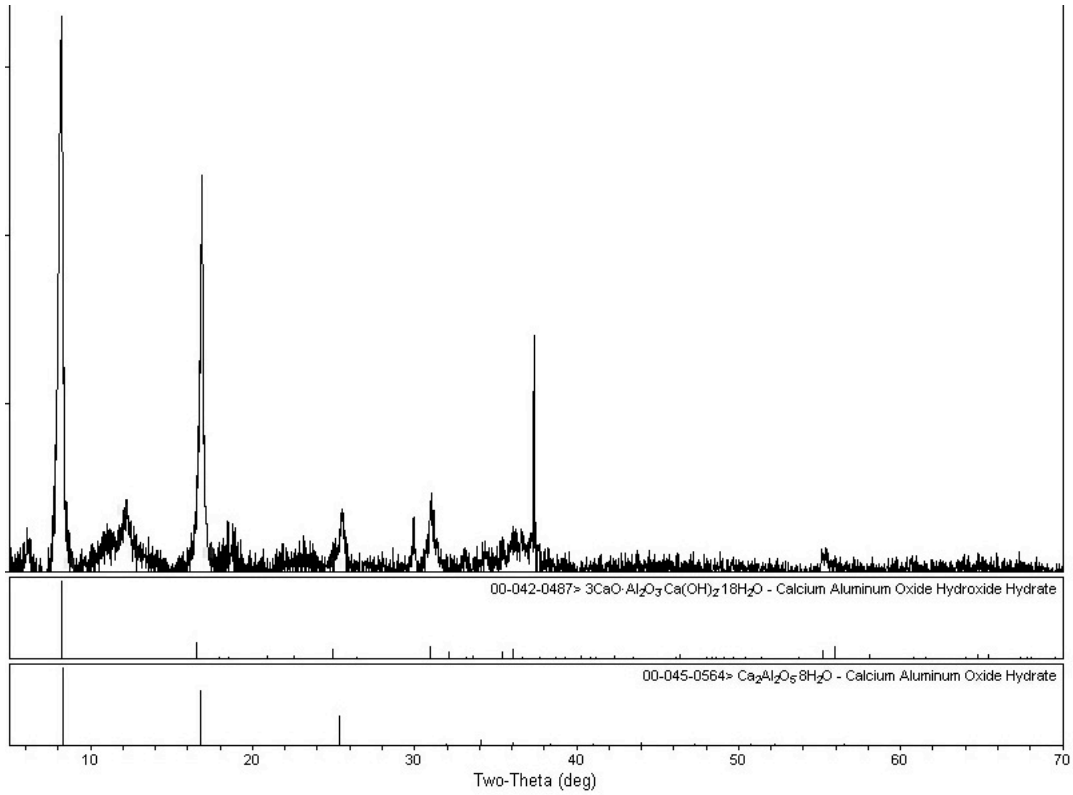

Figure 69. Hydration products formed on the crystalline CA microsphere incubated at 25˚C for 48 hour.

XXII DISCUSSION

A. Hydration of Calcium Aluminates

Several theories have been proposed for the hydration of crystalline calcium silicates and aluminates.[30] The two main theories suggest that hydration occurs as a result of calcium trying to obtain a sixfold coordination, however they disagree on whether it is coordination states above or below 6 that cause these instabilities. Both coordination theories are insufficient in accurately describing the cause of hydration since calcium is present in sixfold coordination in some of the most highly reactive cementing compounds. It has therefore been suggested that hydration occurs as a result of structural 'holes', which have not been found in stable structures that do not hydrate.

The structural 'hole' theory could be used to describe the hydration of amorphous calcium aluminates. The structure of these glasses is thought to be composed of AlO4 tetrahedra with a non-bridging oxygen (NBO) to bridging oxygen (BO) ratio of about 1:3. The calcium ions act as network modifiers, and are octahedrally coordinated by 3 BO and 3 NBO.[32,82] The similarities between the hydration of the amorphous and crystalline frits indicated that the materials formation process, not the presence of NBOs, produced the faster hydration rate of the CA microspheres. Water quenching of the calcium aluminate melts produced hydrated frit that became dehydrated after passing through the flame during microsphere formation. This dehydrated surface was more susceptible to aqueous attack and therefore hydrated at a faster rate until the formation of the protective hydrated crystalline layer. Microspheres will also exhibit a higher fictive temperature then the quenched frit due to faster cooling rates. A glass with a higher fictive temperature has a larger volume that would correspond to a structure with an increased number of structural 'holes'.

The addition of silica and iron oxide to the amorphous calcium aluminates improves their chemical durability by increasing the connectivity of the structure.[31,32] The absence of immediate agglomeration upon contact with water can be attributed to this increase in connectivity. However, the aluminum and calcium were not replaced in equivalent amounts and therefore cannot be directly compared. Equivalent replacements

could not be performed due to the limited glass forming regions of the different compositions.

B. Dehydration of Hydration Products

Difficulties in the structural characterization of the hexagonal hydrates is due to the large number of polymorphs and polytypes that result from the calcium aluminates acute sensitivity to aqueous environments.[30] Phase identification becomes even more ambiguous when hydrates are formed in the presence of atmospheric carbon dioxide, which is often easily incorporated into the hydrated structure. In fact, the α-C4AH13 phase shown in Table XIV is thought to be the carbonate phase $4CaO•Al_2O_3•0.5CO_2•12H_2O$. A carbonate phase could be present in hydrates formed at 25˚C since there was no atmospheric control of the de-ionized water during incubation. The presence of structural carbonate could be determined through extended incubation times in samples with low SA/V ratios. If no carbonate is present, the formation of C3AH6 should accompany the decomposition of the hexagonal hydrates.

While the C2AH8 phase has been commonly reported, the formation of C3ACH18 on hydrated amorphous CA could be supported by solution studies.[30] The formation of a hydrated alumina-rich gel-layer has been found to form in the initial stages of hydration. However, the ICP-OES data showed almost twice the amount of aluminum in solution which suggested that a lime-layer might have formed instead. While this difference in ion leaching could be a result of the CA structural differences discussed earlier, it could also be related to the SA/V ratio and lack of atmospheric control over the solution. The effects of structural differences on hydration could be examined by performing ICP-OES data during the hydration of crystalline CA, especially since the formed phase more closely resembled the C2AH8 XRD pattern better than the C3ACH18. The larger amount of ions present in solution at 40˚C than at 25˚C was the result of faster surface dissolution and precipitation of the hydration products.

The dehydration of the hexagonal hydrates at low temperatures confirms that they are as unstable in atmospheric conditions as they are in aqueous solutions. Dehydration to the C2AH6 was also observed at 25˚C when the XRD system was placed under vacuum. The formation of the C2AH6 phase is debatable however, since little is known

about the exact structure of the anionic layer and the shift in basal spacings is comparable to the dehydration of C2AH8 discussed in Ch3. XVIII. A. 1.

Decomposition of the C3AH6 into the C12A7 phase was consistent with previously reported data. However, the C3A phase was not observed due to the crystallization of the amorphous phase into mayenite at ~825˚C.

C. Effect of Organics on Hydration Products

The effects of Tris on the formation of C3AH6 was similar to those previously reported by Young.[76] Young found that solutions containing 1 wt% of various sugar molecules or large aliphatic molecules could inhibit the hexagonal hydrate conversion to C3AH6 for up to 1 day at 60˚C. However, C3AH6 conversions did occur when the solution temperature was increased to 75˚C or at 38˚C when the organic concentration was reduced to 0.2 wt%. When C3AH6 formed at 38˚C with 1 wt% additions of small, 3-carbon aliphatic molecules (ex. propanol, lactic acid), it was suggested that the compounds ability to inhibit hydration is based on the number and location of the oxy-functional groups. The number and location of these groups is important since conversion hindrance is similar to that of the carbonates, where hydrogen bonding prevents water movement in the anionic layer, but unlike the carbonates, the Tris molecules also interact with the inorganic layer. ESEM examination showed the formation of some hexagonal hydrates in the CA incubated at 25˚C in the 0.24 wt% Tris. However, the reaction products were severely distorted and were not detected by XRD. Therefore, it is thought that although the Tris molecule is small, containing only 3 hydroxyl groups, its amine group must also be participating in hydrogen bonding with the surrounding water molecules. The shift to higher basal spacings in the hydrates formed at 40˚C suggest that the Tris molecules are residing in the structure. The exact location of the Tris molecule in the structure and the reason for the decrease in crystallinity of the CA incubated at 80˚C is not known.

The formation of the hexagonal hydrates, or even surface damage, was completely inhibited by the thick Tris matrix formed around the microspheres incubated in the Tris solution. Unlike the stronger electrostatic interactions observed between alumina and sugar, the Tris was determined to be only weakly hydrogen bonded to the

surface since it could be easily removed by rinsing de-ionized water over the microspheres. Hydration is not expected to occur at longer incubation times, but is could possibly occur at elevated temperatures where the Tris molecule begins to degrade and is unable to hydrogen bond with the surrounding water molecules and/or the oxide surface.

XXIII CONCLUSION

Ambiguities in the structure of the anionic hydrated layer of the hexagonal crystals formed at 25˚C made phase identification difficult. The C3ACH18 phase found to best match the hexagonal hydrates could be due to the accelerated hydration rate of the microspheres. However, the basal spacings of the phase formed at 25˚C were very similar to that of β-C2AH8, with carbonation possibly affecting this since no atmosphere control was performed. Hydration with solutions kept free of CO_2 could help to clarify these results. Longer incubation times in de-ionized water at 25˚C used high SA/V ratios which dehydrated before conversion to the cubic phase was observed. The cubic hydrates formed at 40˚C were easily identified as the commonly reported C3AH6.

Surface hydration was inhibited by large concentrations of Tris which prevented surface hydration through hydrogen bonding to the surrounding water molecules and the oxide surface. Lower Tris concentrations provided better hydration retardation than previously reported aliphatic molecules and is possibly the result of the participation of the primary amine in the hydrogen bonding. Hydration in low Tris concentrations at 25˚C showed distorted hexagonal crystals that were undetectable with XRD. At 40˚C, shifted basal spacings of the cubic hydrates indicated that the Tris had intercalated into the hydrated structure, however its location in this structure is unknown.

SUMMARY AND FUTURE WORK

Oxides exhibiting a positive surface charge in the physiological range were found to have a greater capacity to adsorb DNA in the absence of chaotropic agents. The addition of chaotropic agents to a DNA containing solution effectively shielded or altered the inherent surface charge of the oxide, therefore increasing the amount of DNA that adsorbed to the surface. Isothermal titration calorimetry (ITC) could be used to examine the effects of chaotropic agent concentration on the ability of a negatively charged oxide surface to adsorb DNA. ITC could also be used to determine if the negatively charged phosphate backbone of the DNA has a greater affinity for a positively charged CAFe surface or a negatively charged silicate surface in the presence of chaotropic agents. Measuring the DNA binding energy to alumina coated silica particles could also help to clarify these questions. These particles have a high chemical durability and can be made to exhibit any surface charge ranging between that of silica and alumina. Changes in surface charge could be monitored using various electrokinetic techniques depending on the particle size; streaming potential for particles over 20 μm and sedimentation potential (solid phase movement, liquid phase stationary) for particles below this size. UV absorbance and gel electrophoresis could also be used to determine the optimal particle size for maximum DNA adsorption of various sized strands. These results should be very accurate since no leached ions from the particle surface would be present to interfere with the measurements. DNA orientation on the oxide surface could be examined through atomic force microscopy (AFM), however interactions with the AFM tip could cause problems if the DNA backbone is not fully attached to the surface.

Small concentrations (less than 2 mM) of calcium or aluminum leached from the oxide surface slightly altered the absorbance at ~260 nm but will most likely not interfere with downstream applications that are of concern to biologists (i.e. DNA replication via PCR). Comparisons between the amount of ions leached from the calcium aluminates and commercially used hydroxyapatite should be made to determine the ion concentration that is acceptable in DNA solutions used in commercial applications. Calcium aluminates could still be an acceptable isolation material as long as the buffers

used in attachment inhibit aqueous attack of the surface. Tris molecules inhibited the interactions between the dissociated water molecules and the oxide surface through hydrogen bonding. Hydrogen bonding between the Tris and the DNA also caused more than a monolayer of DNA to adsorb to the oxide surface.

The retardation and/or inhibition of calcium aluminate hydration is highly dependent upon the number of groups an organic has available for hydrogen bonding and also its concentration in solution. Tris was thought to provide better resistance to aqueous attack than other aliphatic molecules of a similar size due to the participation of its primary amine in hydrogen bonding. When cubic hydrates were formed at 40˚C, a shift to higher basal spacings indicated that the Tris had become intercalated into the structure. This was confirmed upon ESEM inspection where the crystals were clearly deformed.

APPENDIX A – QIAGEN® DNA ISOLATION PROTOCOL

DNeasy protocol for animal tissues

1. Cut up 25 mg tissue (or up to 10 mg spleen) into small pieces, place in a 1.5 ml micro-centrifuge tube, and add 180 µl Buffer ATL. It is advisable to cut the tissue into small pieces for efficient lysis.

2. Add 20 µl proteinase K, mix by vortexing, and incubate at 55°C until the tissue is completely lysed.

   Vortex occasionally during incubation to disperse the sample, or place in a shaking water bath on a rocking platform.

   Lysis time varies depending on the type of tissue being processed. Lysis is usually complete in 1–3 h, though samples can be lysed overnight.

   Optional: RNase treatment of the sample. Add 4 µl RNase A (100 mg/ml), mix by vortexing, and incubate for 2 min at room temperature.

   Transcriptionally active tissues such as liver and kidney contain high levels of RNA, which will copurify with genomic DNA. If RNA-free genomic DNA is required, carry out this step.

3. Vortex for 15 s. Add 200 µl Buffer AL to the sample, mix thoroughly by vortexing, and incubate at 70°C for 10 min.

4. Add 200 µl ethanol (98–100%) to the sample, and mix thoroughly by vortexing.

   A white precipitate may form on addition of ethanol. It is essential to apply all of the precipitate to the DNeasy spin column.

5. Pipet the mixture from step 4 into the DNeasy spin column placed in a 2 ml collection tube (provided). Centrifuge at ≥6000 x *g* (8000 rpm) for 1 min. Discard flow-through and collection tube.

6. Place the DNeasy spin column in a new 2 ml collection tube (provided), add 500 µl Buffer AW1, and centrifuge at ≥6000 x *g* (8000 rpm) for 1 min. Discard flow-through and collection tube.

7. Place the DNeasy spin column in a new 2 ml collection tube (provided), add 500 µl Buffer AW2, and centrifuge for 3 min at full speed to dry the DNeasy membrane. Discard flow-through and collection tube.

   This step ensures that no residual ethanol is carried over during the following elution. Remove the spin column carefully to ensure that the column does not touch the flow-through.

8. Place the DNeasy spin column in a clean 1.5 ml or 2 ml collection tube (not provided), and pipet 200 µl Buffer AE directly onto the DNeasy membrane. Incubate at room temperature for 1 min, and then centrifuge for 1 min at ≥6000 x *g* (8000 rpm) to elute.

9. Repeat elution once as described in step 8. Elution can be performed in the same or separate tubes. Do not use more than 200 µl Buffer AE as this will cause the eluate to come into contact with the DNeasy spin column.

APPENDIX B – CALCULATIONS

Ch 2. XIV. C. – DNA Adsorption to Microspheres

Perkin Elmer Spectrometer

- Add 0.04 ml of the 1 mg/ml DNA solution to the cuvette
    - 0.04 mg of DNA in the cuvette

$$\frac{Abs_{DNA}}{0.04mg} = \frac{Abs_{xmg}}{xmg}$$

where Abs_{DNA} is the measured maximum absorption value of the original DNA solution at ~260 nm, Abs_{xmg} is the absorbance of 0.04 ml of a DNA solution rinsed over the microspheres and *xmg* is the amount of DNA that did not attach to the microspheres.

- amount of DNA attached to the glass sample, *Ad*, in µg

$$0.04 - xmg = Ad \times 10^3 \mu g$$

- normalized surface area of 0.1 g of microspheres

$$0.1gmicrospheres \times SA\frac{cm^2}{g} = SAcm^2 \Rightarrow x\mu g / SAcm^2$$

NanoDrop Spectrometer

- DNA concentrations were calculated using the Beer-Lambert law

$$C = \frac{(A \cdot e)}{l}$$

where C is the concentration of nucleic acids in ng/ml, A is the absorbance in AU (-log[intensity of sample/intensity of blank]), e is a combination of the DNA and RNA extinction coefficients (45 ng-cm-μl^{-1}) and l is the path length in cm (1 cm).

Monolayer Adsorption of DNA onto Microsphere/Qiagen® filter Surface

Calf Thymus DNA properties:

- average number of base pairs (bp) per strand - 2000
- height of each bp – 0.0034 μm
- width of double stranded helix – 0.02 μm
- average molecular weight of bp – 660 g/mol

Surface area (SA) of single strand of DNA:

$$SA = 2000 bp/strand \cdot 0.0034 \mu m \cdot 0.02 \mu m = 0.136 \mu m^2$$

Mass of single DNA strand:

$$2000 bp/strand \cdot 660 g/mol \cdot \frac{1 mol}{6.02 \times 10^{23} bp} = 2.2 \times 10^{-12} \mu g/strand$$

Concentration for monolayer coverage of the microsphere/filter based on complete adsorption of the entire DNA backbone:

$$xstrands = \frac{1.1 \times 10^{8} \mu m^{2}}{0.136 \mu m^{2}} = 8.1 \times 10^{8} strands$$

$$Concentration = \frac{8.1 \times 10^{8} \cdot 2.2 \times 10^{-12}}{1.1 cm^{2}} = 1.6 \times 10^{-3} \mu g / cm^{2}$$

Ch 2. XIV. E. – Inductively Coupled Plasma – Optical Emission Spectroscopy

- prepared samples on a mass basis so values were given in ppm

$$xppm \rightarrow x \frac{\mu g}{g} \rightarrow x \frac{10^{-6} g}{ml} \cdot \frac{10^{-3} ml}{L} \cdot \frac{1}{M.W.} = xmoles/L \rightarrow x \times 10^{3} mM$$

REFERENCES

1. *Electrical Phenomena at Interfaces: Fundamentals, Measurements, and Applications*. Edited by A. Kitahara and A. Watanbe Marcel Dekker, New York, 1984.

2. D. Shaw, *Colloid and Surface Chemistry,* 4th ed. Butterworth-Heinemann, Oxford, 1992.

3. R. Hunter, *Zeta Potential in Colloid Science: Principles and Applications*; pp. 20-100, 119-50, 180-343. Academic Press, New York, 1981.

4. G. Parks, "The Isoelectric points of Solid Oxides, Solid Hydroxides, and Aqueous Hydroxo Complex Systems," *Chem. Rev.,* **65** [2] 177-98 (1965).

5. H. Stein, "Surface Charges on Calcium Silicates and Calcium Silicate Hydrates," *J. Colloid Interface Sci.,* **28** [2] 203-13 (1968).

6. E. Nagele and U. Schneider, "The Zeta Potential of Cement: Part IV: Effect of Simple Salts," *Cem. Concr. Res.,* **17** [6] 977-82 (1987).

7. M. Rahaman, *Ceramic Processing and Sintering,* 2nd ed; pp. 153-162. Marcel Dekker, New York, 2003.

8. J. Bockris and A. Reddy, *Modern Electrochemistry 1: Ionics,* 2nd ed; pp. 87-138, 225-349, 555-63. Plenum Press, New York, 1998.

9. C. Noguera, *Physics and Chemistry at Oxide Surfaces*. Cambridge University Press, New York, 1996.

10. E. Nagele, "The Zeta Potential of Cement," *Cem. Concr. Res.,* **15** [3] 453-62 (1985).

11. Anton Paar, Electro Kinetic Analyzer. The Company, Austria, 2003.

12. Z. Csogor, M. Nacken, M. Sameti, C. Lehr, and H. Schmidt, "Modified Silica Particles for Gene Delivery," *Mat. Sci. and Eng. C - Bio. S.,* **23** [1-2] 93-7 (2003).

13. R. Stokes and D. Evans, *Fundamentals of Interfacial Engineering*. Wiley-VCH, New York, 1997.

14. V. Balladur, A. Theretz, and B. Mandarnd, "Determination of the Main Forces Driving DNA Oligonucleotide Adsorption onto Aminated Silica Wafers," *J. Colloid Interface Sci.,* **194** [2] 408-18 (1997).

15. T. Tsai, D. Robinson, and R. Dieckmann, "Preparation of Olivines, (FexMg1-x)2DiO4, by a Sol-Gel Technique," *J. Mater. Synth. and Proces.,* **1** [6] 395-404 (1993).

16. J.J. Horn and G. Onoda, "Surface Charge of Vitreous Silica and Silicate Glasses in Aqueous Electrolyte Solutions," *J. Am. Ceram. Soc.,* **61** [11-12] 523-7 (1978).

17. M. Kosmulski, "The pH-Dependent Surface Charging and the Points of Zero Charge," *J. Colloid Interface Sci.,* **253** [1] 77-87 (2002).

18. M. Robinson, J. Pask, and W. Fuerstenau, "Surface Charge of Alumina and Magnesia in Aqueous Media," *J. Am. Ceram. Soc.,* **47** [10] 516-20 (1964).

19. M. Zembala, "Electrokinetics of Heterogeneous Interfaces," *Adv. Colloid Interface Sci.,* **112** [1-3] 59-92 (2004).

20. J. Jednacak, V. Pravdic, and W. Haller, "The Electrokinetic Potential of Glasses in Aqueous Electrolyte Solutions," *J. Colloid Interface Sci.,* **49** [1] 16-23 (1974).

21. N. Vdovic and J. Biscan, "Electrokinetics of Natural and Synthetic Calcite Suspensions," *Colloid Surface A.,* **137** [1-3] 7-14 (1998).

22. T. Kumar, S. Prabhakar, and G. Raju, "Adsorption of Oleic Acid at the Silimanite/Water Interface," *J. Colloid Interface Sci.,* **247** [2] 275-81 (2002).

23. Anton Paar, "Characterization of Glass Microspheres," The Company, Austria, 2003.

24. L. Pye, "Aluminate Glasses - A Review," *Infrared Optical Materials VI;* pp. 149-56. **929** (1988).

25. K. Nakagawa, I. Terashima, K. Asaga, and M. Daimon, "A Study of Hydration of Amorphous Calcium Aluminate by Selective Dissolution Analysis," *Cem. Concr. Res.,* **20** [4] 655-61 (1990).

26. A. Traetteberg and P. Grattan-Bellew, "Hydration of 3CaO•Al2O3 and 3CaO•Al2O3+Gypsum with and without CaCl2," *J. Am. Ceram. Soc.,* **58** [5-6] 221-6 (1975).

27. K. Murakami, H. Tanaka, and Y. Nakura, "The Early Stage of Hydration of 3CaO•Al2O3 and Na2O•8CaO•3Al2O3 as Clinker Minerals of Portland Cement," *Chem. Ind. - London,* 1769-70 (1968).

28. R. Edmonds and A. Majumdar, "The Hydration of 12CaO 7Al2O3 at Different Temperatures," *Cem. Concr. Res.,* **18** [3] 473-8 (1988).

29. E. Breval, "C3A Hydration," *Cem. Concr. Res.,* **6** [1] 129-38 (1975).

30. F. Lea, *The Chemistry of Cement and Concrete,* 3rd. ed; pp. 48-65, 177-527. Chemical Publishing Company, New York, 1971.

31. H. Hafnew, N. Kreidl, and R. Weidel, "Optical and Physical Properties of Some Calcium Aluminate Glasses," *J. Am. Ceram. Soc.,* **41** [8] (1958).

32. J. Shelby, "Formation and Properties of Calcium Aluminate Glasses," *J. Am. Ceram. Soc.,* **68** [3] 155-8 (1985).

33. E. Uhlmann, M. Weinberg, N. Kreidl, and A. Goktas, "Glass-Forming Ability in Calcium Aluminate-Based Systems," *J. Am. Ceram. Soc.,* **76** [2] 449-53 (1993).

34. A. Varshneya, *Fundamentals of Inorganic Glasses*; pp. 112-5, 397-408, 510-2. Academic Press, New York, 1993.

35. L. Holland, *The Properties of Glass Surfaces*; pp. 126-74. Chapman and Hall, New York, 1964.

36. K. Suzuki, T. Nichikawa, K. Kato, H. Hayashi, and S. Ito, "Approach by Zeta Potential Measurement on the Surface Change of Hydrating C3S," *Cem. Concr. Res.,* **11** [5-6] 759-64 (1981).

37. "U.S. Department of Energy Office of Science: Office of Biological and Environmental Research" (2007) Accessed on: April, 2008. Available at <http://genomics.energy.gov>

38. N. Campbell, L. Mitchell, and J. Reece, *Biology: Concepts and Connections,* 2nd ed; pp. 174-8. Benjamin/Cummings Publishing Company, New York, 1997.

39. A. Colman, M. Byers, S. Primrose, and A. Lyons, "Rapid Purification of Plasmid DNAs by Hydroxyapatite Chromatography," *Eur. J. Biochem.,* **91** 303-10 (1978).

40. B. Vogelstein and D. Gillespie, "Preparative And Analytical Purification of DNA from Agarose," *Biochemistry,* **76** [2] 615-9 (1978).

41. R. Boom, C. Sol, M. Salimans, C. Jansen, P.W.-v. Dillen, and J.v.d. Noordaa, "Rapid and Simple Method for Purification of Nucleic Acids," *J. Clin. Microbiol.,* **28** [3] 495-503 (1990).

42. D. Voet and J. Voet, *Biochemistry: Biomolecules, Mechanisms of Enzyme Action, and Metabolism,* 3rd ed; pp. 46-155. John Wiley & Sons, New York, 2004.

43. C. Cantor and P. Schimmel, *Biophysical Chemistry: Part I: The Conformation of Biological Macromolecules (Their Biophysical Chemistry; PT. 1),* Vol. 1*;* pp. 177-83, 311-97. W. H. Freeman, New York, 1980.

44. C. Cantor and P. Schimmel, *Biophysical Chemistry: Part II: Techniques for the Study of Biological Structure and Function (Their Biophysical Chemistry; PT. 2),* Vol. 2*;* pp. 462-553. W. H. Freeman, New York, 1980.

45. C. Cantor and P. Schimmel, *Biophysical Chemistry: Part III: The Behavior of Biological Macromolecules (Their Biophysical Chemistry; PT. 3),* Vol. 3*;* 1170-6, 1239-47. W. H. Freeman, New York, 1980.

46. T. Devlin, *Textbook of Biochemistry with Clinical Correlations,* 3rd ed; pp. 82-3, 609-23. Wiley-Liss, New York, 1992.

47. D. Nelson and M. Cox, *Principles of Biochemistry,* 4th ed; Chapter 8. W. H. Freeman, New York, 2005.

48. Wikepedia, "DNA" (2008) Accessed on: April, 2008. Available at <http://en.wikipedia.org/wiki/DNA>

49. J. Brady and J. Holum, *Chemistry: The Study of Matter and Its Changes,* 2nd ed; pp. 375-7, 698-9. John Wiley & Sons, New York, 1996.

50. J. Matthew and F. Richards, "Differential Electrostatic Stabilization of A-, B- and Z-Forms of DNA," *Biopolymers,* **23** [12] 2743-59 (1984).

51. J. Wu, F. Du, P. Zhang, I. Khan, J. Chen, and Y. Liang, "Thermodyanmics of the Interaction of Aluminum Ions with DNA: Implications for the Biological Function of Auminum," *J. Inorg. Biochem.,* **99** 1145-54 (2005).

52. R. Ahmad, H. Arakawa, and H. Tajmir-Riahi, "A Comparative Study of DNA Complexation with Mg(II) and Ca(II) in Aqueous Solution: Major and Minor Grooves Bindings," *Biophys. J.,* **84** 2460-6 (2003).

53. H. Drew and R. Dickerson, "Structure of a B-DNA Dodecamer; III. Geometry of Hydration," *J. Mol. Biol.,* **151** [3] 535-56 (1981).

54. E. Kejnovsky and J. Kypr, "Millimolar Concentrations of Zinc and Other Metal Cations Cause Sedimentation of DNA," *Nucleic Acids Res.,* **26** [23] 5295-9 (1998).

55. M. Kopka, A. Fratini, H. Drew, and R. Dickerson, "Ordered Water Structure Around a B-DNA Dodecamer: A Quantitative Study," *J. Mol. Biol.,* **163** [1] 129-46 (1983).

56. G. Manning, "Electrostatic Free Energy of the DNA Double Helix in Counterion Condensation Theory," *Biophys. Chem.,* **101-102** 461-73 (2002).

57. J. Anastassopoulou, "Metal-DNA Interactions," *J. Mol. Struct.,* **651-653** 19-26 (2003).

58. T. Chiu and R. Dickerson, "1A Crystal Structures of B-DNA Reveal Sequence-specific Binding and Groove-specific Bending of DNA by Magnesium and Calcium," *J. Mol. Biol.,* **301** [1] 915-45 (2000).

59. E. Hackl, S. Kornilova, L. Kapinos, V. Andrushchenko, V. Galkin, D. Grigoriev, and Y. Blagoi, "Study of Ca2+, Mn2+ and Cu2+ Binding to DNA in Solution by Means of IR Spectroscopy," *J. Mol. Struct.,* **408/409** [1] 229-32 (1997).

60. K. Rao and S. Divakar, "Spectroscopic Studies on the Effects of Aluminum Ion on Calf-Thymus DNA," *B. Environ. Contam. Tox.,* **50** [1] 92-9 (1993).

61. *Biomaterials Science: An Introduction to Materials in Medicine,* 2nd ed; pp. 211-5, 813-5. Edited by B. Ratner, A. Hoffman, F. Schoen, and J. Lemons. Elsevier Academic Press, New York, 2004.

62. F. Stephenson, *Calculations for Molecular Biology and Biotechnology: A Guide to Mathematics in the Laboratory*, pp. 151-60. Academic Press, New York, 2003.

63. N. Good and S. Izawa, "Hydrogen Ion Buffers," in Vol. 24, *Methods in Enzymology.* Edited by A. SanPietro. Academic Press, New York, 1972.

64. N. Good, G. Winget, W. Winter, T. Connolly, S. Izawa, and R. Singh, "Hydrogen Ion Buffers for Biological Research," *Biochemistry,* **5** [2] 467-77 (1966).

65. R. Durst and B. Staples, "Tris/Tris•HCl: A Standard Buffer for Use in the Physiologic pH Range," *Clin. Chem.,* **18** [3] 206-8 (1972).

66. T. Thiel, L. Liczkowski, and S. Bissen, "New Zwitterionic Butanesulfonic Acids that Extend the Alkaline Range of Four Families of Good Buffers: Evaluation for use in Biological Systems," *J. Biochem. Biophys. Methods,* **37** [3] 117-29 (1998).

67. J. Grady, N. Chasteen, and D. Harris, "Radicals from "Good's" Buffers," *Anal. Biochem.,* **173** [1] 111-5 (1988).

68. R. Sheardy, "Monitoring Conformational Transitions in Synthetic DNA Oligomers using Circular Dichroism," *Spectroscopy,* (1991).

69. P. Cai, Q. Huang, and X. Zhang, "Microcalorimetric Studies of the Effects of MgCl2 Concentrations and pH on the Adsorption of DNA on Montmorillonite, Kaolinite and Goethite," *Appl. Clay Sci.,* **32** 147-52 (2006).

70. W. Baase and W. Johnson, "Circular Dichroism and DNA Secondary Structure," *Nucleic Acids Res.,* **6** [2] 797-814 (1979).

71. P. Sauer, M. Muller, J. Kang, "Quantitation of DNA," Technical Report, Qiagen, Germany, 1998.

72. Qiagen, DNeasy Tissue Handbook. The Company, USA, 2004.

73. W. Chen, M. Lin, P. Lin, P. Tasi, Y. Chang, and S. Yamamoto, "Studies of the Interaction Mechanism Between Single Strand and Double-Strand DNA with Hydroxyapatite by Microcalorimetry and Isotherm Measurements," *Colloid Surfaces A.,* **295** [1-3] 274-83 (2007).

74. D. Skoog and J. Leary, *Principles of Instrumental Analysis,* 4th ed; Chapter 8. Saunders College Publishing, Fort Worth, TX, 1992.

75. S. Rodger, S. Brooks, W. Sinclair, G. Groves, and D. Double, "High Strength Cement Pastes," *J. Mat. Sci.,* **20** [8] 2853-60 (1985).

76. J. Young, "Effect of Organic Compounds on the Interconversions of Calcium Aluminate Hydrates: Hydration of Tricalcium Aluminate," *J. Am. Ceram. Soc.,* **53** [2] 65-9 (1970).

77. P. Mondal and J. Jeffery, "The Crystal Structure of Tricalcium Aluminate, C3Al2O6," *Acta Crystallogr.,* **B31** 689-96 (1975).

78. G. Bye, *Portland Cement: Composition, Production and Properties*; pp. 99-138. Pergamon Press, New York, 1983.

79. N. Ukrainczyk, T. Matusinovic, S. Kurajica, B. Zimmermann, and J. Sipusic, "Dehydration of a layered double hydroxide - C2AH8," *Thermochim. Acta,* **464** [1-2] 7-15 (2007).

80. S. Martin, M. O'Keeffe, and R. VonDreele, "The Crystal Structure of the Hydrogarnet Ba3In2(OD)12," *J. Solid State Chem.,* **87** 173-7 (1990).

81. H. Stein, "Mechanism of the Hydration of 3CaO,Al2O3," *J. Appl. Chem.,* **13** 228-32 (1963).

82. A. Hannon and J. Parker, "The Structure of Aluminate Glasses by Neutron Diffraction," *J. Non-Cryst. Solids,* **274** [1-3] 102-9 (2000).

83. J. Gebauer and R. Coughlin, "Preparation, Properties and Corrosion Resistance of Composites of Cement Mortar and Organic Polymers," *Cem. Concr. Res.,* **1** [2] 187-210 (1971).

84. K. Singh and S. Mohan, "Kinetic Studies of the Sucrose Adsorption onto an Alumina Interface," *Appl. Surf. Sci.,* **221** [1] 308-18 (2004).

85. O. Popoola, W. Kriven, and J. Young, "Microstructural and Microchemical Characterization of Calcium Aluminate-Polymer Composite (MDF Cement)," *J. Am. Ceram. Soc.,* **74** [8] 1928-33 (1991).